University of Mohamed Boudiaf-M'sila

FACULTY OF TECHNOLOGY

DEPARTMENT OF ELECTRONIC

Serial number:……..
Registration number: DE/03/15

Thesis

Presented for the graduation of

DOCTORAT OF SCIENCES

Field: Electronic
Option: Electronic

THEME

Theoretical and experimental study of defects for $Cu(In,Ga)Se_2$ absorbers

Presented by:

Rafik ZOUACHE

Defended the: 18/10/2023

Jury members:

Prof. Djamel KHADROUCHE	University of M'sila	Chairman
Prof. Idris BOUCHAMA	University of M'sila	Supervisor
Prof. Achour SAADOUN	University of Biskra	Examiner
Prof. Khaled BEKHOUCHE	University of Biskra	Examiner
Prof. Hamza BENNACER	University of M'sila	Guest

2022 /2023

Dedication

With deep respect and gratitude, I offer this work as a dedication: To my beloved mother and cherished father, whose affection and love have been invaluable.

May God protect them.

To my wife and my daughter, Djoumana. And to my entire family.

Acknowledgements

I would like to extend my deepest appreciation to ***Prof. Idris BOUCHAMA***, my supervisor, for the unwavering support and invaluable guidance he provided throughout my doctoral studies. I am truly grateful for his patience, boundless motivation, and invaluable advice, which have greatly contributed to the advancement of my research career. His constant encouragement and generous support during my time as a PhD student have been immeasurable.

I would like to express my heartfelt appreciation to each and every ***member of the jury*** for their strong interest in my work and for graciously agreeing to evaluate my research as members of the jury of my thesis.

Rafik Zouache

LIST OF FIGURES

CHAPTER I: Solar cell presentation

CHAPTER II: Physical properties of Cu(In,Ga)Se_2 materials

CHAPTER III: Simulation of CIGS solar cell using SILVACO/Atlas software

CHAPTER IV: Impacts of crystalline defects in CIGS material on CIGS solar cell performances

CHAPTER V: Experimental study of $Cu(In,Ga)Se_2$ thin film

LIST OF TABLES

CHAPTER II: Physical properties of Cu(In,Ga)Se_2 materials

CHAPTER III: Simulation of CIGS solar cell using SILVACO/Atlas software

CHAPTER IV: Impacts of crystalline defects in CIGS material on CIGS solar cell performances

CHAPTER V: Experimental study of Cu(In,Ga)Se_2 thin film

TABLE OF CONTENTS

CHAPTER II: Physical properties of Cu(In,Ga)Se_2 materials

Chapter III: Simulation of CIGS solar cell using SILVACO/Atlas software

Chapter IV: Impact of crystalline defects in CIGS material on CIGS solar cell performances

Chapter V: Experimental study of $Cu(In,Ga)Se_2$ thin film

GENERAL INTRODUCTION

GENERAL INTRODUCTION

The industrial development and growth of the world's population have led to a rapid increase in energy consumption over the past few decades. Unfortunately, a large part of this consumption is based on fossil fuels, such as oil, natural gas, and coal, which are considered to be exhaustible resources. In addition to their exhaustible nature, these fossil resources also have several drawbacks, including global warming with greenhouse gas emissions, radioactive pollution and the release of carbon dioxide CO_2.

Recent progress in the world has encouraged research and development programs on renewable energies, such as solar, thermal, and wind energy, which are environmentally friendly. Solar energy is an attractive alternative source of energy that is inexhaustible and pollution-free. The Earth receives an annual energy from the sun of 1018 kWh, which is approximately 20000 times more than the current annual energy consumption of the world.

Government budgets and private investments in the production of electricity from solar cells are increasing regularly with the aim of limiting future energy demand. Several photovoltaic power plants are multiplying around the world to generate large amounts of electricity compared to the past. Silicon wafers are highly demanded for the production of integrated circuits and in the solar cell industry, and their cost has therefore increased as evidenced by the market. Solar cells based on $Cu(In,Ga)Se_2$ (CIGS) thin film can be an alternative to silicon.

CIGS is a semiconductor with an appropriate energy gap and a high optical absorption coefficient in the visible range of solar spectrum. The absorption coefficient of CIGS films is 100 times greater than that of Si in the visible range. Additionally, CIGS solar cells exhibit excellent stability, high radiation resistance [1,2] and achieve the highest efficiency compared to other chalcopyrites, CdTe and a-Si:H thin film solar cells. Single junction CIGS solar cell with active surface area of 0.5 cm^2 has shown the highest efficiency of 20.3% at the Center for Solar Energy and Hydrogen Research Baden Württemberg (ZSW) [3] and 19.9% at the National Renewable Energy Laboratory (NREL) [4]. Single junction thin film solar cells have advantages due to their low cost [5] and high efficiency [6] compared to other solar cells, but their conversion efficiency is limited by the Shockley Queisser limit [7]. Improving their efficiency requires the use of multi-junction configurations [8]. Multi-junction crystalline solar cells achieve the world record efficiency [9], but they are expensive to produce due to the costly epitaxial growth [10]. Therefore, it would be desirable to use low cost polycrystalline thin film solar cells for multi-junction applications, such as CdTe and CIGS solar cells.

The electronic behavior of CIGS thin film solar cells is mainly influenced by the presence of crystalline defects in CIGS absorber layer [11-13]. Depending on the manufacturing process, the density of grains and dislocations, it can vary considerably.

The objective of our work is to analyze the impact of deep defects that can be detected in CIGS absorber layer and the formation of Ordered Defect Compound layer on the performance of CIGS solar cell using SILVACO/Atlas software. Single junction solar cells based on CIGS absorber layer with and without back surface filed BSF layer, Tandem and Triple junction solar cells were also investigated. The SILVACO/Atlas tool enables the design and prediction of the performance of CIGS solar cells.

This thesis consists of five chapters:

The first chapter is focused on examining the principles and characteristics of photovoltaic solar cells.

The second chapter will cover the fundamental properties of the CIGS material used as an absorber layer in our work. Additionally, we will discuss the different defects that can be found within the CIGS bulk and the associated manufacturing processes.

Chapter three begins with a brief introduction to the SILVACO/Atlas-2D simulator tool. It focuses on the optimizing of J-V characteristics to study the performance of three types of CIGS solar cells using SILVACO/Atlas tool. Specifically, we investigate the effects of structural, electrical and external parameters on the substrate CIGS solar cell performance, with and without back surface field layer, as well as CGS/CIGS tandem and triple-junction solar cell structure performances.

The fourth chapter begins by examining the effect of the formation of Ordered Defect Compound layer on the performance of $ZnO/In_2Se_3/ODC/CIGS/Mo$ solar cell structure. Subsequently, we will present the effect of activation energies (E_A) for acceptor trap states and (E_D) for donor trap states.

The last chapter presents the experimental details to manufacture high-quality $Cu(In,Ga)Se_2$ thin film using RF magnetron sputtering technique. Structural, morphological and optical properties of obtained CIGS thin film were also investigated.

REFERENCE

[1] Yamaguchi, M. (1995). Radiation resistance of compound semiconductor solar cells. Journal of Applied Physics, 78(3), 1476-1480. doi:10.1063/1.360236.

[2] Ullal, H. S., Zwelbel, K., Von Roedern, (1997). Current status of polycrystalline thin-film PV technologies. Conference Record of the Twenty Sixth IEEE Photovoltaic Specialists Conference -. doi:10.1109/pvsc.1997.654089.

[3] Jackson, P., Hariskos, D., Lotter, E., Paetel, S., Wuerz, R., Menner, R., Powalla, M. (2011). New world record efficiency for Cu(In,Ga)Se_2 thin-film solar cells beyond 20%. Progress in Photovoltaics: Research and Applications, 19(7), 894-897. doi:10.1002/pip.1078.

[4] Repins, I., Contreras, M., Romero, M., Yan, Y., Metzger, W., Li, J., Noufi, R. (2008). Characterization of 19.9%-efficient CIGS absorbers. 2008 33rd IEEE Photovolatic Specialists Conference. doi:10.1109/pvsc.2008.4922628.

[5] Edoff, M. (2012). Thin Film Solar Cells: Research in an Industrial Perspective. AMBIO, 41(S2), 112-118. doi:10.1007/s13280-012-0265-6.

[6] Repins, I., Contreras, M. A., Egaas, B., DeHart, C., Scharf, J., Perkins, C. L., Noufi, R. (2008). 19·9%-efficient ZnO/CdS/$CuInGaSe_2$ solar cell with 81·2% fill factor. Progress in Photovoltaics: Research and Applications, 16(3), 235–239. doi:10.1002/pip.822.

[7] Shockley, W., Queisser, H. J. (1961). Detailed Balance Limit of Efficiency of p-n Junction Solar Cells. Journal of Applied Physics, 32(3), 510-519. doi:10.1063/1.1736034.

[8] Green, M. A. (2001). Third generation photovoltaics: Ultra-high conversion efficiency at low cost. Progress in Photovoltaics: Research and Applications, 9(2), 123-135. doi:10.1002/pip.360.

[9] Green, M. A., Emery, K., Hishikawa, Y., Warta, W., Dunlop, E. D. (2013). Solar cell efficiency tables (version 42). Progress in Photovoltaics: Research and Applications, 21(5), 827-837. doi:10.1002/pip.2404.

[10] Cotal, H., Fetzer, C., Boisvert, J., Kinsey, G., King, R., Hebert, P., Karam, N. (2009). III-V multijunction solar cells for concentrating photovoltaics. Energy Environ. Sci., 2(2), 174-192. doi:10.1039/b809257e.

[11] Jackson, P., Wuerz, R., Hariskos, D., Lotter, E., Witte, W., Powalla, M. (2016). Effects of heavy alkali elements in Cu(In,Ga)Se_2 solar cells with efficiencies up to 22.6%. Physica Status Solidi (RRL) - Rapid Research Letters, 10(8), 583-586. doi:10.1002/pssr.201600199.

[12] Bouchama, I., Zouache, R., Djessas, K., Bouloufa, A., and Ghribi, F. (2015). Size and grain-boundary effects on the performance of polycrystalline CIGS-based solar cells. IREC2015 The Sixth International Renewable Energy Congress. doi:10.1109/irec.2015.7110920.

[13] Zouache, R., Bouchama, I., Saidani, O., Djedoui, L., and Zaidi, L. (2022). Numerical study of high-efficiency CIGS solar cells by inserting a BSF µc-Si:H layer. J Comput Electron 21, 1386-1395. https://doi.org/10.1007/s10825-022-01942-5.

Chapter I: Solar cell presentation

Chapter I

Solar cell presentation

I.1. Introduction

In this chapter, we will present several useful concepts related to the photovoltaic conversion. Firstly, we define a photovoltaic solar cell and provide an overview of solar radiation, which serves as the primary source of energy conversion in solar cells. We delve into the operational principles of solar cell, including its equivalent circuit diagram and primary characteristics and examining the physical and technological losses that limit its efficiency. Furthermore, we explore the different generations and different structures of solar cells. We conclude this chapter by highlighting both the benefits and disadvantages of photovoltaic energy.

I.2. Definition of photovoltaic solar cell

A photovoltaic solar cell is a device that directly converts electromagnetic energy (solar radiation) into direct usable continuous electrical energy (see Fig. I.1).

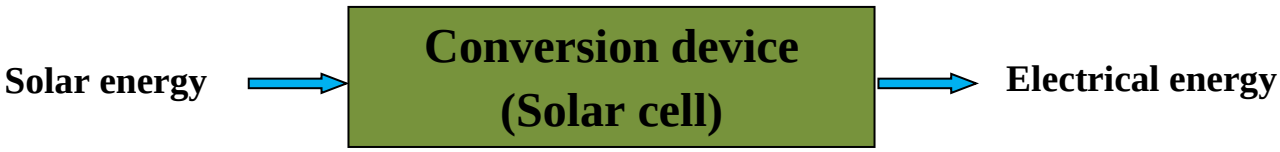

Fig. I.1: Solar cell device for transforming solar energy into electricity.

I.3. Solar spectrum

The sun releases radiation in the form of electromagnetic waves, which travel through space and reach the upper part of the earth's atmosphere. These waves span a range of wavelengths, including visible light (between 0.4 and 0.75 µm) and near-infrared (above 0.75 and up to approximately 4 µm), due to the sun's high surface temperature of around 5800 K [1]. A graphical representation of the spectral distribution of this solar radiation, known as the AM1.5G spectrum, can be found in Fig. I.2 and shows how this radiation reaches the surface of the earth.

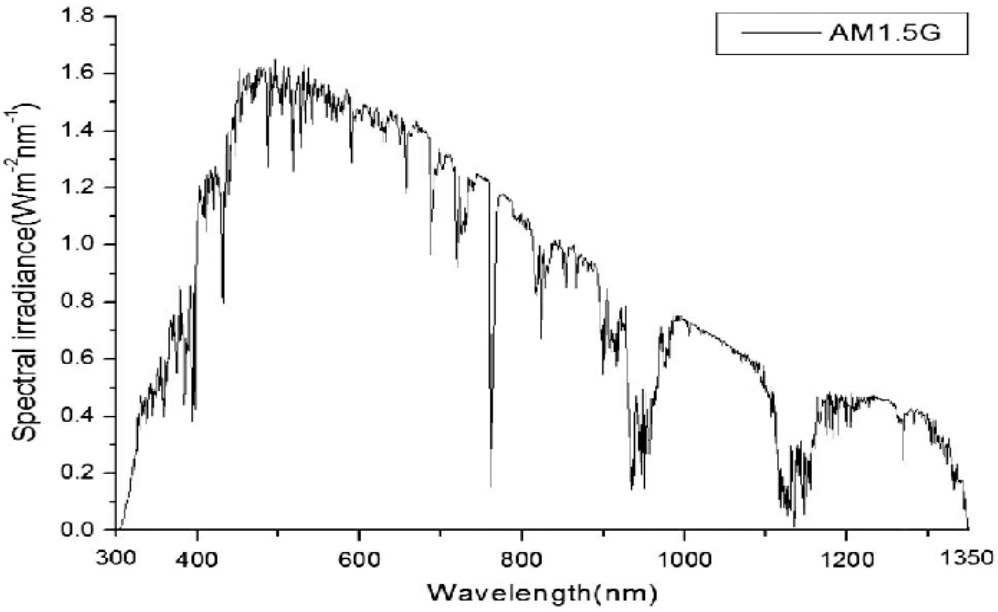

Fig. I.2: Spectral distribution of the solar spectrum AM1.5G.

We use a coefficient known as the number of air mass AMx to factor in the distance that light rays travel. This expression is introduced to account for the distance traveled by the light as follows:

$$X = 1/Sin\theta \tag{I.1}$$

Referring to Fig. I.3 [2], the angle θ represents the deviation of the sun's direction from the zenith. AM0 conditions are defined as the solar radiation outside the atmosphere. At the angle of 48.19° from the zenith, the sunlight is termed as AM1.5, which corresponds to 83.3 mW/cm² power carried by the solar radiation when the surface is inclined at an angle of 37°. AM1.5 is considered as standard to evaluate the efficiency of new photovoltaic devices.

The International Electrotechnical Commission (IEC) has established standard characterization conditions and it is outlined in the IEC-60904 standards. These conditions are based on a global AM1.5 spectral distributions, with a total intensity of 100 mW/cm², and assume a cell temperature of 25°C [2]. Solar radiation on the Earth's surface is composed of a direct component and a diffuse component, which is created by the scattering or reflection of incident radiation by obstacles such as the clouds. The sum of these two components is referred to as global radiation. The global solar emission spectrum under AM1.5 is standardized to 100 mW/cm² [3], and its intensity can vary depending on factors such as pressure, altitude and the angle at which the light rays strike the surface.

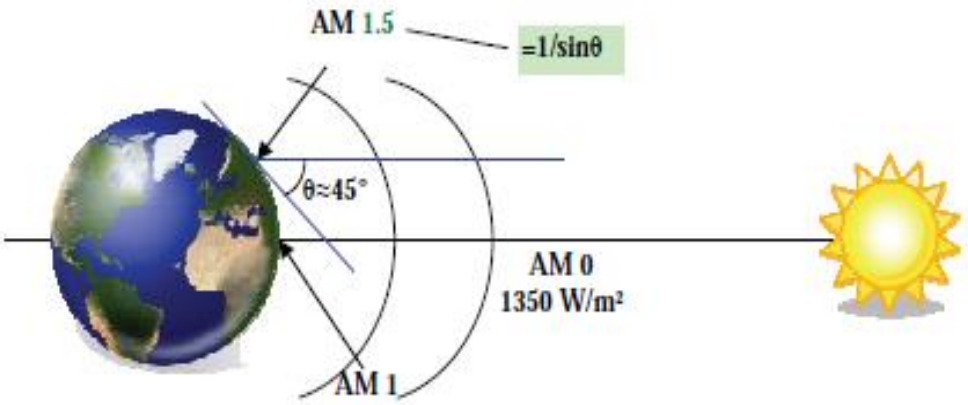

Fig. I.3: Standards for measuring the spectrum of light energy emitted by the sun, concept of the AM standard.

To simplify, we use the following concepts [4]:

- AM0: Out of the atmosphere (spatial application) P = 1.35 kW.m^{-2}.
- AM1: The sun at the zenith of the place of observation (at the equator).
- AM1.5: Standard spectrum, P = 1 kW.m^{-2} for the angle of the sun at 45°.

I.4. Solar radiation conversion

This conversion is carried out via electronic components based on semiconductor materials, known as solar cells or photovoltaic cells. So, the solar photovoltaic panel is comprised of a collection of solar cells.

The photon in the solar spectrum is associated with an energy *E:*

$$E = h\nu \tag{I.2}$$

with:

- ν : Frequency of the photon.
- h: Planck's constant.

The solar cell comprises two semiconductors with varying conductivities, namely, p-type (where the holes are the dominant carriers) and n-type (where the electrons are the dominant carriers). When these semiconductors are exposed to light, an electric current can be generated and directed to an external load. In generally the solar cells are described as p-n junctions obtained by varying the type of doping in a semiconductor, look in Fig. I.4. the conversion of energy is the result of the absorption of photons giving rise to the creation of electron holes.

N-type doping (negative), which consists of introducing foreign atoms into the semiconductor crystal structure that have the property of each giving an excess electron, free to move within the crystal (e.g. phosphorus in the case of silicon).

P-type doping (positive), which uses atoms whose insertion into the crystal lattice will create an excess hole (e.g. boron in the case of silicon).

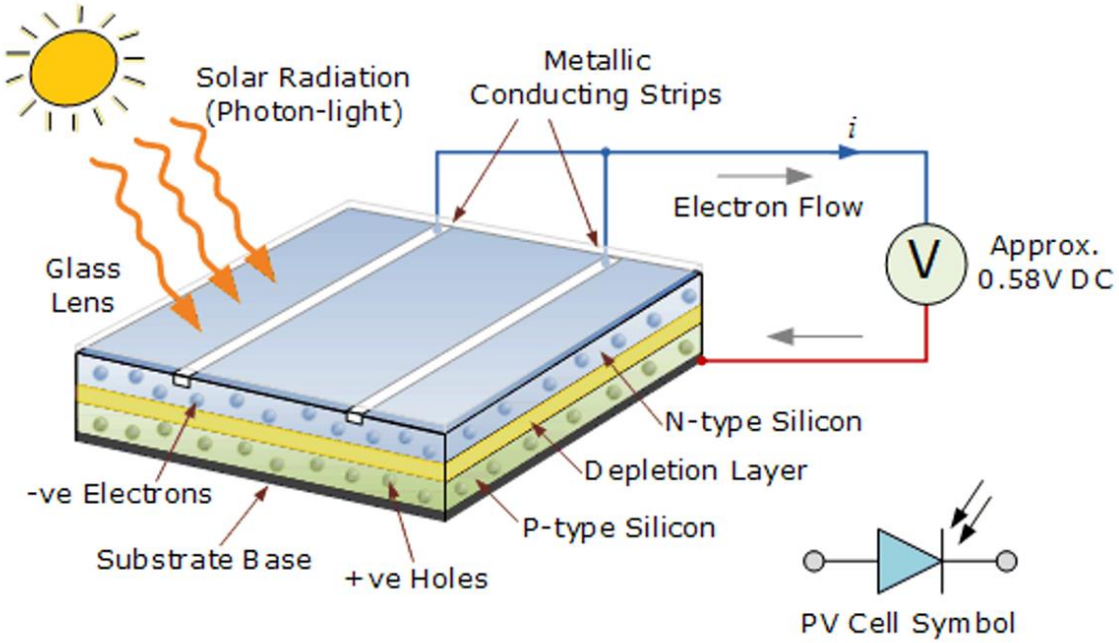

Fig. I.4: Construction of a solar cell.

When the first one comes into contact with the second, excess electrons in material n diffuse into material p. The initially doped n zone becomes positively charged, and the initially doped p zone becomes negatively charged. Thus, an electric field is created between them, which tends to push electrons into the n zone and holes into the p zone then the p-n junction is formed. By adding metal contacts on the n and p zones, a diode is obtained. When the junction is illuminated, photons with energy equal to or greater than the band-gap energy transfer their energy to the atoms. Each atom moves an electron from the valence band to the conduction band, leaving behind a hole that can move and thus generating an electron-hole pair. When a load is attached to the cell, an external connection allows for the flow of electrons from the n zone to the p zone, resulting in the creation of a potential difference [5].

I.5. Modeling of solar cell

I.5.1. Ideal case

The ideal solar cell can be described by the following equation [6]:

$$I = I_{ph} - I_D = I_{ph} - I_0 \times \left(\exp\left(qV/KT\right) - 1\right) \quad \text{(I.3)}$$

The equivalent electrical circuits corresponding to a solar cell are shown in Fig. I.5.

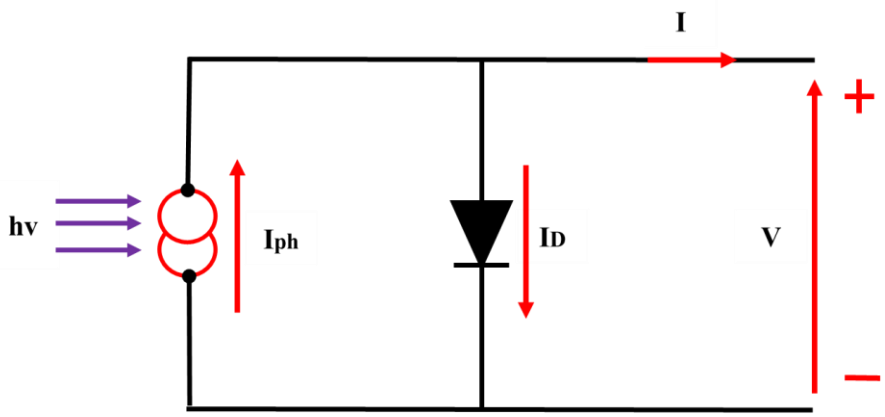

Fig. I.5: Electrical circuits that correspond to an ideal solar cell.

and:

- J-V: Current and voltage provided by the cell.
- I_D: Diode current given by equation [**7**]:

$$I_D = I_0 \cdot \left(\exp\left(qV/AkT\right) - 1\right) \quad \text{(I.4)}$$

with:

- q: Elementary charge is $1.6.10^{-19}$C.
- V: Voltage across the p-n junction.
- k: Constant of Boltzmann = $1.38.10^{-23}$ J.K^{-1}.
- T: absolute temperature (K).
- I_0: Reverse saturation current of the p-n junction.
- A: p-n junction ideality factor.

I.5.2. Real case

The performance of a solar cell is limited by the influence of two physical phenomena similar to two resistances (R_S and R_{sh}). The R_S is the serial resistance, mainly due to losses by Joule effects through the collection grids and the specific resistance of semiconductors, as bad contacts (semiconductor, electrodes), it is expressed by the following relation [8].

$$R_S = R_m + \left(\rho L / S_g\right) \quad \text{(I.5)}$$

with:

- ρ: Resistivity of the grid.
- L: Length of the grid.

- S_g: Section of the collector grid.
- R_m: The material's inherent resistance has a low value (< 2Ω for silicon cells).

Shunt resistance R_{sh} is the parallel resistance that created from recombination losses mainly due to thickness, surface effects and the non-ideal of p-n junction. The booths resistances R_S and R_{sh} are modified the short circuit current of the cell in photo-current I_{ph}, the equivalent circuit of a solar cell presented in Fig. I.6.

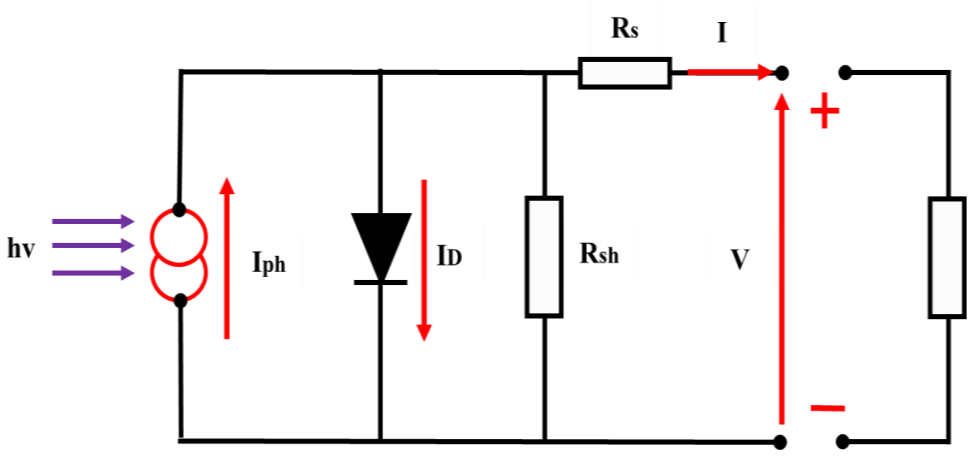

Fig. I.6: Equivalent schema of a real solar cell.

By apply Kirchhoff's law to nodes A and B:

$$I = I_{ph} - I_D - I_{sh} \tag{I.6}$$

with:

- I_{ph}: Photogenerated current it is proportional to the incident flow (generation rate) g and the electron and hole diffusion lengths (L_n, L_p) [7].

$$I_{ph} = qg(L_n + L_p) \tag{I.7}$$

- I_{sh}: Shunt current, if R_{sh} is very large, this current become very low.

$$I_{sh} = V_D / R_{sh} = (V + I.R_s)/R_{sh} \tag{I.8}$$

whereas:

$$V_D = R_{sh}.I_{sh} = V + I.R_s \tag{I.9}$$

- I_D: Diode current, the same order of magnitude as I_{sh} for low voltages and it becomes very large in the vicinity of V_{OC}, it is written in the form [7]:

$$I_D = I_0.\left(\exp\left(V_D.q/AKT\right) - 1\right) \tag{I.10}$$

Based on the preceding equations, we can infer the conclusive representation of the output current:

$$I = I_{ph} - I_0\left(\exp\left(\left(V + I.R_S\right).q/A.K.T\right) - 1\right) - \left(V + I.R_S\right)/R_{sh} \qquad \text{(I.11)}$$

I.6. Characteristic of a solar cell

When a solar cell operates under different conditions, such as varying levels of temperature or illumination, it produces a relationship between the current and voltage generated, which is called the J-V (current-voltage) characteristics (see Fig. I.7). This relationship is depicted graphically and is a representation of the cell's performance, providing valuable information about its efficiency, power output, and other electrical properties, if the cell operates under a fixed illumination and at the constant temperature. The operation of the module is essentially characterized by three areas.

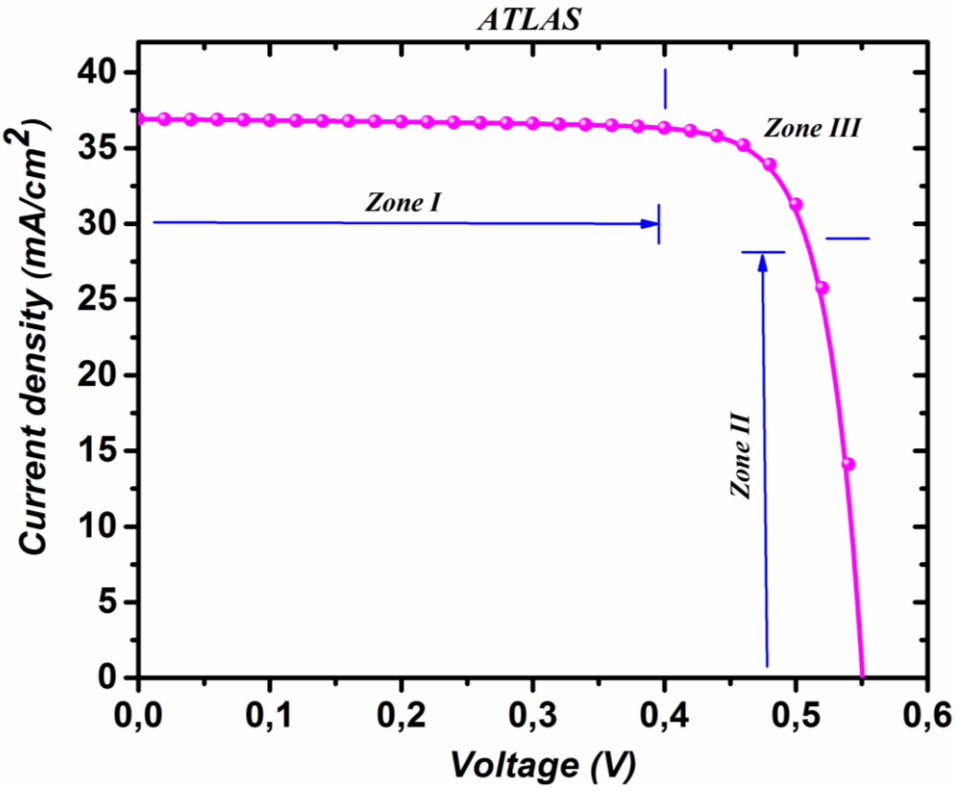

Fig. I.7: J-V characteristic of illuminated solar cell.

- **Zone I:** In this zone, the cell acts like a current generator with a constant output value, which produces low power, high current and low voltage.
- **Zone II:** Solar cell behaves as a voltage generator in open circuit V_{OC}, the operation of the cell in this zone gives low powers, small currents and high voltages.
- **Zone III:** Operation of the cell in this zone gives high powers, acceptable currents and voltages.

I.6.1. Short-circuit current I_{sc}

The short-circuit current is delivered when the potential applied to the cell is zero. This is the largest current the cell can supply. This is a function of the temperature and the wavelength of the radiation, the active surface of the cell, the mobility of the carriers is linearly dependent on the light intensity received on the cell area, explained in equation (I.12):

$$I_{sc} = I_{ph} - I_0.\left(\exp\left(qR_s I_{sc}/AkT\right)-1\right) - I_{sc}R_s/R_{sh} \quad \text{(I.12)}$$

when (R_S=0 and $R_{Sh}\rightarrow\infty$)

$$I_{sc} = I_{ph} \quad \text{(I.13)}$$

I.6.2. Open-circuit voltage V_{oc}

At zero current, the highest voltage that a solar cell can produce is referred to as the open-circuit voltage (V_{OC}). The open-circuit voltage is an outcome of the solar cell junction's forward bias as a result of the light-generated current. It is obtained by following equation (I.14):

$$0 = I_{ph} - I_0.\left(\exp\left(qV_{OC}/AkT\right)-1\right) - V_{OC}/R_{sh} \quad \text{(I.14)}$$

when (R_S=0 and $R_{Sh}\rightarrow\infty$)

$$V_{OC} = \frac{nkT}{q}\ln\left(\frac{I_{SC}}{I_0}+1\right) \quad \text{(I.15)}$$

I.6.3. Fill Factor *FF*

The Fill Factor is the ratio that accounts for the quality of the shape of the current-voltage characteristic J-V; on the other hand, it is the ratio between the maximum power that a cell can supply and the power that it is theoretically possible to deliver, to obtain the power optimal. The equation used to define this ratio is as follows:

$$FF = P_m/I_{SC}V_{OC} = I_m V_m/I_{SC}V_{OC} \quad \text{(I.16)}$$

While I_m and V_m represent the current-voltage couple for which the power delivered by the cell is maximum P_m. The theoretical studies indicate that the fill factor is between 0.25 and 1. The fill factor can also give information on the quality of the material-electrode interfaces, when its value drops below 25%, the presence of a non-ohmic contact or an oxidized/insulating layer at the interface between the material and electrode is typically indicated by this phenomenon.

I.6.4. Conversion Efficiency η

When it comes to assessing the performance of a solar cell, the efficiency (η) is the primary metric used. The efficiency of the cell is determined by its ability to convert light energy into electrical power, and it can be represented as the ratio between the maximum power output of the cell and the incident power P_{in}. This relation can be expressed mathematically using the following equation:

$$\eta = P_m / P_{in} = I_{SC} V_{OC} FF / P_{in} \tag{I.17}$$

The incident power of the light equal to the solar power (P solar = 100 mW/cm^2). Conversion efficiency can be improved by increasing the Fill Factor, short-circuit current and open-circuit voltage [9].

I.6.5. Quantum Efficiency QE

The Quantum efficiency (QE) of a solar cell is described as the ratio of collected carriers to incident photons at each wavelength. In an ideal scenario, every photon that reaches the device produces an electron-hole pair, contributing one carrier to the photocurrent. Consequently, the quantum efficiency is expected to be 100% for photon energies above the band gap, while it will be zero for energies below it. However, real solar cells do not always achieve this ideal scenario, and there is always some degree of reflection loss, even after efforts have been made to minimize it, due to the reflection of light from the front surface of the cell, we can express the external quantum efficiency QE by the following equation.

$$QE = \frac{\text{Number of collected photons}(\lambda)}{\text{Number of incident photons}(\lambda)} \tag{I.18}$$

I.7. Capacitance-voltage

The C-V characteristic is a valuable tool for assessing the performance and optimizing the design of solar cells. This measurement quantifies the device's ability to store electrical charge in response to an applied voltage by measuring the resulting capacitance from a small AC voltage. The obtained C-V characteristic provides crucial information on the device's doping density, depletion width, and interface trap density [10].

I.8. Different photovoltaic solar cell technologies

The commercial photovoltaic solar (PV) cells can be divided into two broad categories: crystalline silicon (c-Si) wafer-based solar cells and thin-film solar cells. Currently, a

representation of the annual world market is 85-90% for the first generation and 10-15% for the second [11]. Additionally, there is a range of currently emerging technologies, including advanced thin-film designs, PV concentrators, organic and photo-electrochemical solar cells. In the long term, new, innovative concepts are being considered. These are hoped to achieve a significant performance increase and cost reduction by implementing nano-geometries, plasmonic effects and up or down conversion, according to reference [11]. Fig. I.8 presents a comparison of the status and potential of various technologies in terms of their efficiency in converting solar energy to electricity, to give a guide to the chronological and topical development for the PV, new concepts were grouped according to the technological developments in three generations [12].

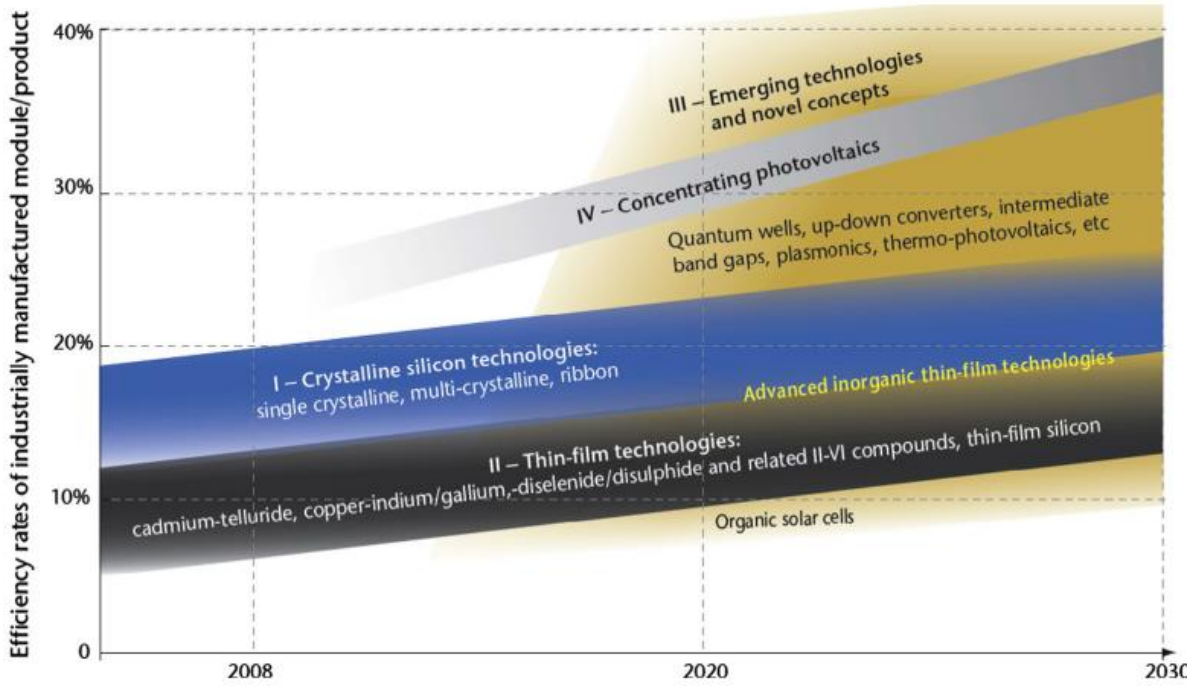

Fig. I.8: Insights into the past, current and potential status of photovoltaic technology.

I.8.1. First generation of photovoltaic solar cells

The utilization of silicon for the fabrication of photovoltaic modules is based on its physical and chemical properties, particularly its use in microelectronics and its non-toxicity [13]. In addition, its crystalline form is highly suitable for making the single p-n junction in the first-generation cells.

The silicon wafer-based production process is costly due to its high energy consumption and the need for high-purity silicon, and it distinguishes between monocrystalline and polycrystalline cells, the former of which have higher efficiency but higher manufacturing costs than the latter.

I.8.2. Second generation of photovoltaic solar cells

Thin-film solar cells, being a second-generation solar technology, hold great promise in terms of cost reduction. These cells use only the necessary amount of photosensitive material to efficiently absorb solar radiation, resulting in a thickness of just a few micrometers. Moreover, the use of low-cost substrates such as glass or flexible ones, as well as the ability to directly serialize the cells onto the substrate, makes the manufacturing process less expensive. This is expected to lead to a greater reduction in production costs per unit area compared to those based on c-Si, and to benefit from economies of scale provided by the large area industrial tools developed by flat panel display technologies [11,14].

The most famous absorber materials of this generation are: hydrogenated amorphous silicon (a-Si:H), hydrogenated microcrystalline silicon (µc-Si:H), Cadmium Telluride (CdTe) and Copper Diselenide, Indium and Gallium (CIGS).

The problem in the second-generation cells is the low efficiency compared to the first generation and the toxicity of some elements (such as Cadmium Cd for the CdTe and the CdS) and the scarcity of others (such as Indium In for the CIGS). However, this second generation has many advantages for the markets such as applications in flexible modules, with weak illuminations or with high temperatures.

I.8.3. Third generation of solar cells

New design and manufacturing techniques may have to be incorporated into second generation solar technologies to compete with c-Si technology in terms of cost. These innovative concepts are often referred to as third-generation technologies.

It is anticipated that the third generation of solar cells will have improved efficiency and make use of low-cost substrates or deposition methods to overcome the limitations of single-junction devices, potentially leading to the development of ultra-high efficiency devices with production costs comparable to first and second-generation solar cells.

The third or next generations of photovoltaic cells often feature technologies such as optical concentration-based cells, the deposition of fixed material systems on new substrates, or alternative manufacturing techniques. Devices that have commercially realized, such as photo-electrochemical dye solar cells (also called Grätzel or DSSC) [15] and organic photovoltaic solar cells based on polymers (OPV), including organic-inorganic hybrids and perovskite solar cells, face several challenges [11]. In this study, we have selected to investigate second-generation cells in greater detail, specifically CIGS-based solar cells.

I.9. Photovoltaic solar cell structure

In most cases, a thin-film solar cell is composed of three primary layers which are the p-type absorber layer, the n-type buffer layer, and the transparent conducting oxide (TCO) layer. This can be observed in Fig. I.9.

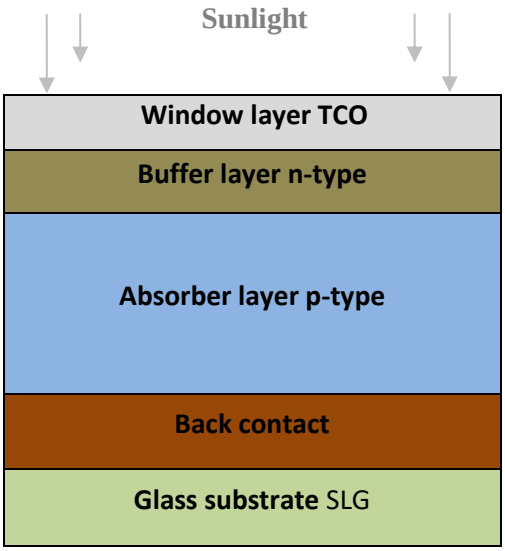

Fig. I.9: Schematic representation of a typical solar cell structure.

I.9.1. Absorber layer

The heart of thin film solar cells is often referred to as the absorber layer, which is a semiconducting material. This layer's primary function is to absorb the highest number of photons and excite electrons in the conduction band to create a photocurrent. To achieve this, the material must have a high absorption coefficient in the visible spectrum and should ideally be a p-type material due to its long electron scattering length. The thickness of the Absorber layer is typically between 1 μm to 3 μm [11]. There are a number of materials with a band gap around 1.5 eV. However, other factors such as technology and stability are also important. Deposition methods are varied depending on the type of absorber material. Some of the most noteworthy solar cells based on absorber materials are Si, a-Si, GaAs, CdTe, InP, Zn_3P_2, CZTSSe, and CIGS, which have garnered considerable attention.

I.9.2. Buffer layer

The buffer layer is positioned between the absorber layer and the transparent conducting oxide (TCO) layer. Any layer that transmits light from the cell is classified as part of the window layer [16]. The electronic characteristics of the buffer layer must allow for a band shift that is compatible with both the absorber-buffer layer and buffer layer-optical window layer interfaces. This enables the photo-generated electrons to move freely while limiting the

recombination current [17,18], which contributes to the optimization of the solar cell's performance. Moreover, the buffer layer must exhibit n-type conductivity and possess the following properties:

- The conductivity of the buffer layer should be lower than that of the absorber layer, typically around 10^{-3} $(\Omega.cm)^{-1}$, in order to prevent current leakage effects.
- To facilitate a seamless transition between the absorber and the optical window, the intermediate band gap should have a broad value of 2.4 eV to minimize light absorption.
- CdS is the most commonly used material with a thickness ranging from 30 to 50 nm, allowing for high efficiency [19]. However, due to its toxicity, efforts are being made to replace CdS with materials that are Cd-free and have a higher band gap (such as In_2Se_3, ZnS, Zn(S,O), Zn(S,O,OH), (Zn,Mg)O) in order to reduce optical losses [20-21].

I.9.3. Window layer

The window layer in a solar cell is composed of transparent layers that allow light to pass through to the buffer layer and absorber layer. This layer possesses specific characteristics, as outlined in reference [16].

- The ZnO layer in a solar cell typically has a large band gap (3.3 eV), which results in high transparency. To minimize reflection losses, an antireflective coating is usually applied to the top of the cell. Additionally, the layer exhibits high conductivity, with a value of 5×10^2 $(\Omega.cm)^{-1}$ as reported in reference [22].
- High resistance in order to limit the formation of short-circuits in the zones presenting an imperfect covering of the absorber by the buffer layer [23].

I.10. Structures of photovoltaic solar cells based on CIGS material

I.10.1. Classic structure

The conventional solar cell that utilizes a $Cu(In,Ga)Se_2$ absorber is commonly referred to as the "standard structure" or "substrate structure". The substrate structure is composed of the following layers as indicated in Fig. I.10:

- A rear metal electrode in Molybdenum (Mo) deposited on a glass substrate.
- A p-type absorber layer whose thickness can vary from 1 µm to 3 µm.
- A buffer layer with a thickness of 10 nm to 100 nm each, respectively ensuring the junction and the absence of short circuit.

- An optical window layer which must combine two essential properties, namely electrical conductivity and optical transparency.
- An aluminum-nickel front metal grille required for current collection.

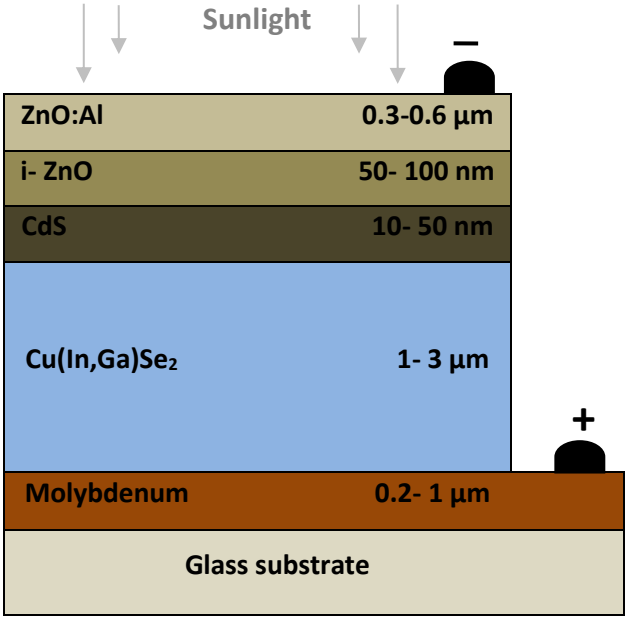

Fig. I.10: Schematic diagram of classical Cu(In,Ga)Se_2 thin film solar cell.

For Cu(In,Ga)Se_2 solar cell, in addition to the metallic electrodes (lower ohmic contact (Molybdenum) and upper ohmic contact (Ni/Al)), the substrate CIGS cell structure consists mainly of three elements: an absorbing layer (p-Cu(In,Ga)Se_2), a buffer (n-CdS, i-ZnO) and an aluminum doped ZnO optical window (ZnO:Al). The deposition of the buffer layer between the absorber and the optical window serves to avoid a possible short circuit due to the interconnection between the layers. It must be very thin (< 0.2 µm) so as not to impede the passage of charge carriers. It is also used to adapt the energy bands of the absorber and of the optical window to avoid discontinuities due to differences in component gaps and to facilitate the passage of carriers [24].

I.10.2. Superstrate structure

The superstrate structure configuration is the made up of the following different semiconductor layers: Glass substrate (SLG)/Transparent conducting oxide layer (TCO)/buffer layer (i-ZnO)/CIGS absorber/back contact. Fig. I.11 presented this structure. This configuration has advantages over the classic substrate configuration [25]:

- Makes it possible to eliminate the buffer layer of the CdS, it is first of all the transparent and conductive window playing the role of n/n+ type emitter (most often constituted by an

oxide) which will be deposited on the glass substrate, followed by the deposition of the p-type absorber while a metal contact (Ag) will be deposited on the back.

- Offers an easier encapsulation of the cell. The glass substrate acts not only as a support for the cell but also as part of the encapsulation, leading to a reduction in module cost compared to those of substrate type cells.
- Has merit in making a more advanced tandem structure, namely, multi-junction solar cells, in which it acts as a superior cell for the short wavelength part of the solar radiation.

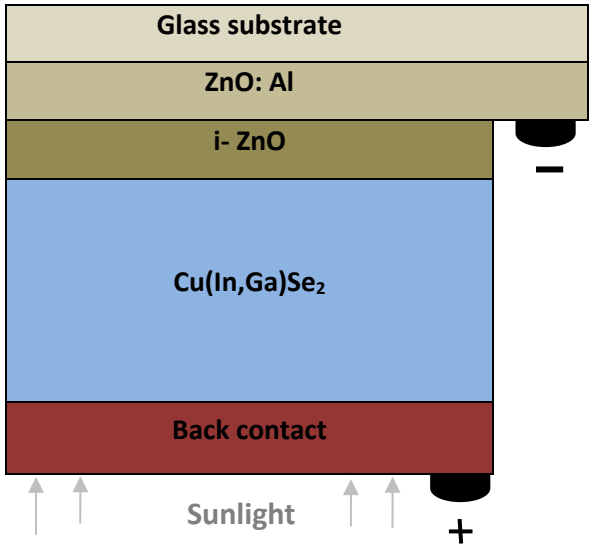

Fig. I.11: Superstrate solar cell structure.

I.10.3. Bifacial structure

The bifacial solar cell shown in Fig. I.12 can be illuminated from both sides. However, its performance is better when illuminated from the front face compared to when illuminated from the rear face. This phenomenon has been well-documented in the literature, and it is explained by the difficulty that photo-generated carriers face in reaching the junction when illuminated from the rear face.

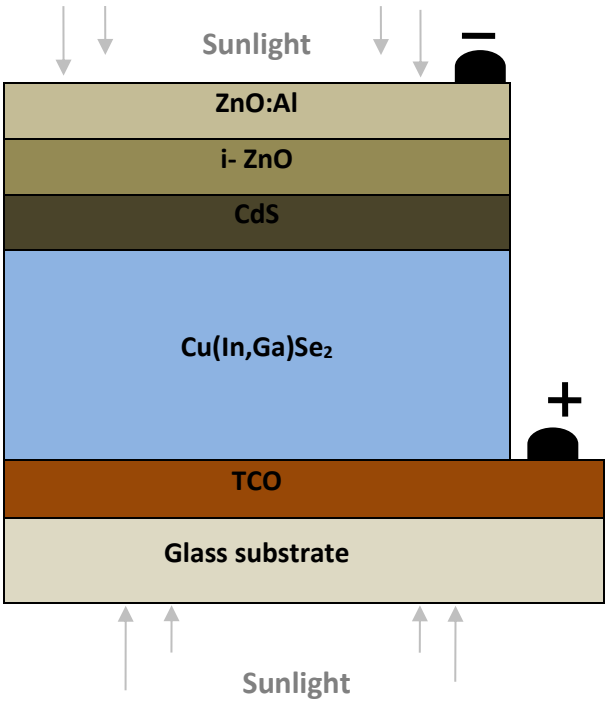

Fig. I.12: Bifacial solar cell structure.

I.10.4. Tandem cell

The CIGS tandem structure is made up of a series of semiconducting materials with decreasing band gaps. This allows for the efficient collection of incident radiation by combining the small band gap E_g = 1.16 eV solar cell based on CIGS with the large band gap E_g = 1.69 eV cell based on CGS, as illustrated in Fig. I.13. It is theoretically possible to achieve an efficiency of up to 25.11% [26].

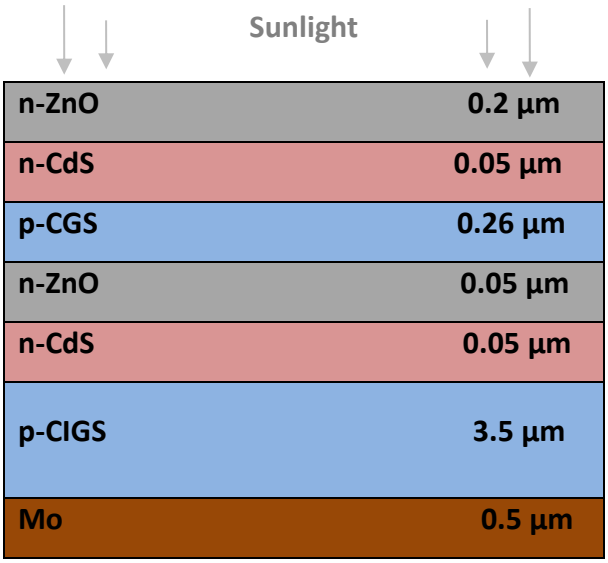

Fig. I.13: Tandem solar cell structure.

I.11. Benefits and disadvantages of photovoltaic energy

I.11.1. Benefits

- Most manufacturers provide a 25-year guarantee on their modules, which speaks to their high reliability
- The fact that photovoltaic energy is well-suited for remote areas is why it has been utilized on spaceships.
- The photovoltaic panels are designed in a modular manner which facilitates easy assembly and enables customization to fulfill diverse energy requirements.
- Due to minimal maintenance requirements and the absence of fuel, transportation, and highly skilled labor, the operating expenses of these systems are exceptionally low. Typically, a professional visit once or twice a year is sufficient for maintenance purposes.

I.11.2. Disadvantages

- Producing a photovoltaic module involves advanced technology and necessitates significant financial investment.
- Large space is required for the installation.
- Photovoltaic generators can only compete with diesel generators in remote areas with low energy demands.

I.12. Conclusion

The first chapter is structured into two sections. In the first one, an overview of solar cell devices is presented, the section covers the basic principle of photovoltaic cell operation. Furthermore, the section delves into how the current-voltage characteristic of the cell is used to determine physical parameters, and examines the different photovoltaic sectors in thin layers.

Second section centered on the different structural designs of thin-film solar cells developed. Our bibliographic research led us to identify CIGS as the most promising semiconductor for manufacturing such cells. To conclude, we examined the advantages and disadvantages of photovoltaic energy.

References

[1] Dessus, B., Pharabod, F. (1996). L'énergie solaire, Presses Universitaires de France, Paris, France.

[2] Villalva, M. G., Gazoli, J. R., Filho, E. R. (2009). Comprehensive Approach to Modeling and Simulation of Photovoltaic Arrays. IEEE Transactions on Power Electronics, 24(5), 1198-1208. doi:10.1109/tpel.2009.2013862

[3] Heriche, H., Rouabah, Z., Bouarissa, N. (2016). High-efficiency CIGS solar cells with optimization of layers thickness and doping. Optik Int. J. Light Electron Opt 127(24), 11751-11757. https:// doi. org/ 10. 1016/j. ijleo. 2016. 09. 071.

[4] Nann, S., Riordan, C. (1991). Solar Spectral Irradiance under Clear and Cloudy Skies: Measurements and a Semiempirical Model. Journal of Applied Meteorology, 30(4), 447-462. doi:10.1175/1520-0450(1991)030<0447:ssiuca>2.0.co;2.

[5] Observ'er. (2004). Baromètre du solaire photovoltaïque, Système Solaires, No. 160, pp. 68-83.

[6] http://www.abcelectronique.com. Consulted on March 13, 2022.

[7] http://www.gelgif.ulaval.ca. Consulted on March 26, 2022.

[8] Lazizi, A. (2019). Modélisation, contrôle et gestion énergétique d'une installation de pompage solaire. Thèse de Doctorat, Universite M'hamed Bougara-Boumerdes, Algerie.

[9] Mathieu, H. (2009). Physique des semiconducteurs et des composants électroniques, Dunod, sciences sup.

[10] Martin, A. G. (1982). Solar Cells: The Prentice Hall.

[11] Abermann, S. (2013). Non-vacuum processed next generation thin film photovoltaics: Towards marketable efficiency and production of CZTS based solar cells. Solar Energy, 94, 37-70. doi:10.1016/j.solener.2013.04.017.

[12] Green, M. A. (2006). Third-Generation Photovoltaics: Advanced Solar Energy Conversion. Springer, Berlin.

[13] Veschetti, Y. (2005). Modélisation, caractérisation et réalisation de nouvelles structures photovoltaïques sur substrat de silicium mince, Thèse de doctorat, L'Université Louis Pasteur, Strasbourg I, France.

[14] Ricaud, A. (2005). Modules photovoltaïques-Filières technologiques, Dossier Techniques de l'Ingénieur, 10/05.

[15] Green, M. A. (2001). Third generation photovoltaics: Ultra-high conversion efficiency at low cost. Progress in Photovoltaics: Research and Applications, 9(2), 123-135. doi:10.1002/pip.360.

[16] Scheer, R., Schock, H.W. (2011). Chalcogenide Photovoltaics: Physics, Technologies, and Thin Film Devices, Wiley-Vch Verlag and Co. KGaA, Boschstr. 12, 69469 Weinheim, Germany.

[17] Rau, U., Schock, H.W. (1999). Electronic properties of Cu(In,Ga)Se_2 heterojunction solar cells-recent achievements, current understanding, and future challenges, Appl.Phys. A, vol. 69, no. 2, pp.131-147.

[18] Rau, U., Schmidt, M. (2001). Electronic properties of ZnO/CdS/Cu(In,Ga) Se_2 solar cells-aspects of heterojunction formation, Thin Solid Films, vol. 387, no. 1-2, pp.141–146.

[19] Naghavi, N., Abou-Ras, D., Allsop, N., Barreau, N., Bücheler, S., Ennaoui, A., Törndahl, T. (2010). Buffer layers and transparent conducting oxides for chalcopyrite Cu(In,Ga)$(S,Se)_2$ based thin film photovoltaics: present status and current developments. Progress in Photovoltaics: Research and Applications, 18(6), 411-433. doi:10.1002/pip.955.

[20] Friedlmeier, T. M., Jackson, P., Bauer, A., Hariskos, D., Kiowski, O., Wuerz, R., Powalla, M. (2015). Improved Photocurrent in Cu(In,Ga)Se_2 Solar Cells: From 20.8% to 21.7% Efficiency with CdS Buffer and 21.0% Cd-Free. IEEE Journal of Photovoltaics, 5(5), 1487-1491. doi:10.1109/jphotov.2015.2458039.

[21] Schmid, D., Ruckh, M., Schock, H. (1996). A comprehensive characterization of the interfaces in Mo/CIS/CdS/ZnO solar cell structures. Solar Energy Materials and Solar Cells, 41-42, 281–294. doi:10.1016/0927-0248(95)00107-7.

[22] Fonash, S. (2010). Solar Cell Device Physics, Second ed, Chapter. 5, Elsevier, USA.

[23] Rau, U., Grabitz, P. O., Werner, J. H. (2004). Resistive limitations to spatially inhomogeneous electronic losses in solar cells. Applied Physics Letters, 85(24), 6010-6012. doi:10.1063/1.1835536.

[24] Nakada, T., Hirabayashi, Y., Tokado, T., Ohmori, D., Mise, T. (2004). Novel device structure for Cu(In,Ga)Se_2 thin film solar cells using transparent conducting oxide back and front contacts. Solar Energy, 77(6), 739-747. doi: 10.1016/j.solener.2004.08.010.

[25] Ikeda, S., Kamai, R., Min Lee, S., Yagi, T., Harada, T., Matsumura, M. (2011). A superstrate solar cell based on $In_2(Se,S)_3$ and $CuIn(Se,S)_2$ thin films fabricated by electrodeposition combined with annealing. Solar Energy Materials and Solar Cells, 95(6), 1446-1451. doi:10.1016/j.solmat.2010.11.006.

[26] Elbar, M., Tobbeche, S. (2015): Numerical simulation of CGS/CIGS single and tandem thin-film solar cells using the silvaco-atlas software. Energy Proc. 74, 1220-1227. https:// doi. org/10. 1016/j. egypro. 2015. 07. 766.

Chapter II: Physical properties of $Cu(In,Ga)Se_2$ materials

Chapter II

Physical properties of Cu(In,Ga)Se_2 materials

II.1. Introduction

The primary objective of this chapter is to provide readers with the necessary knowledge to understand the topic at hand. We will begin by discussing critical concepts pertaining to Cu(In,Ga)Se_2 (CIGS) materials. This will involve describing the crucial properties of the material and providing an overview of the deposition processes used for CIGS thin films.

In general, there are two types of solid state, the state in which the arrangement of atoms is random and the state in which the atoms are arranged regularly at the nodes of a lattice. The first state is called amorphous. The materials that solidify in an amorphous state are generally called glasses. This state differs from the liquid state only by the degree of viscosity. Any liquid with a shear viscosity greater than 10^{13} poise is called glass.

The second state, which interests us more particularly here, is the crystallized state, characterized by the fact that the atoms are arranged at the nodes of a periodic lattice. So, the result is an ordered set of nuclei and electrons bound together by essentially Coulomb forces. Among these materials, interest is focused on chalcopyrite I-III-VI_2 compounds in general and on the CIGS material in particular. The latter is one of the most promising compounds for photovoltaic conversion. It has good photovoltaic characteristics, in particular, a direct band-gap and a high absorption coefficient, it has enabled solar cells to achieve photovoltaic conversion efficiencies of around 22.9% [1], so the CIGS layer is the key material in CIGS-based solar cells as an absorber layer, therefore the structural and optoelectronic properties must be studied.

II.2. Fundamental elements of CIGS material

In 1876, the first semiconductor based photovoltaic component was realized by mechanically introducing a layer of selenium between two electrodes. But the introduction of copper and indium was make until the next century, in 1973, by Wagner and these collaborations which obtained efficiency of 12% from a single crystal of $CuInSe_2$ [2]. The first $CuInSe_2$-based thin film solar cells were made by Boeing [3].

In the following section, we present some values of the physical and chemical parameters of the elements Cu, In, Ga and Se, used in the synthesis of $CuInSe_2$ and $CuGaSe_2$ materials and the basic elements which compose the CIGS material in the following section.

A. Copper

According to scientific classification, copper (Cu) is an element with an atomic number of 29, and it has a melting point of 1,085°C. It is believed that copper was likely the earliest metal used by humans, and it has a distinctive reddish hue when polished. Additionally, copper is known for its exceptional thermal and electrical conductivity [4].

B. Indium

Indium (In) is an element with an atomic number of 49. It is a lustrous gray metal that has a low melting point and is resistant to atmospheric corrosion. Although it is malleable and shares chemical similarities with aluminum and gallium. Indium is considered rare and is only found in trace amounts within zinc mines [5]. The recent surge in demand for indium, particularly in the manufacturing of LCD screens, has led to a steep price point of approximately 1000$/kg in 2005 [5].

C. Gallium

Gallium (Ga) is an element with an atomic number of 49, and it has a low melting point of 29.76°C, which allows it to melt in the hand [6]. When pure, gallium has a pleasing silvery appearance and shatters similarly to glass when in a solid state. Often, gallium is alloyed with arsenic to create III-V composite materials, specifically "AsGa" or gallium arsenide.

D. Selenium

Selenium (Se), a member of the chalcogen family, is an element with an atomic number of 34 and a melting point of 220.8°C. Although it is considered a trace element, selenium can be highly toxic in very low doses. In Fig. II.1, the real images for the four materials are presented.

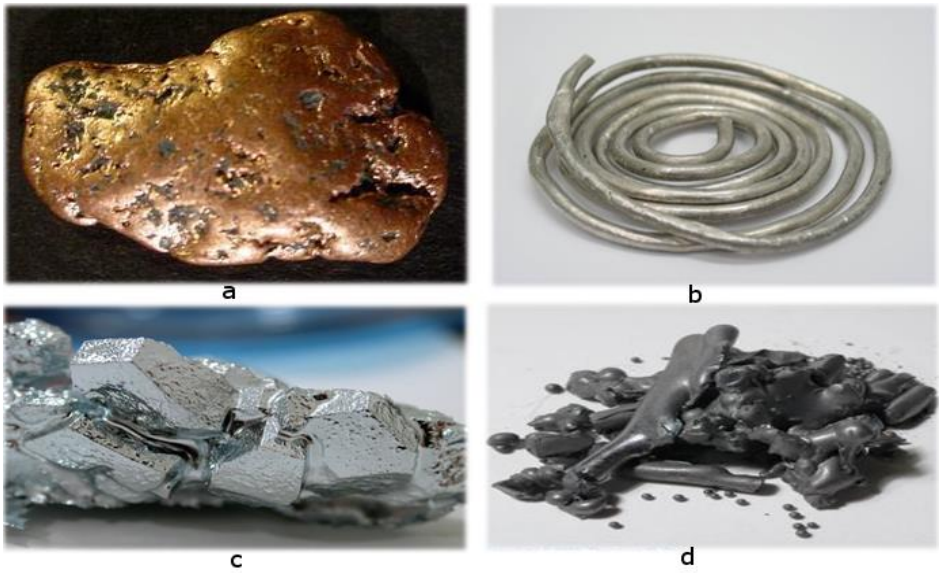

Fig. II.1: (a): Copper sample, (b): Indium wire, (c): Gallium crystals and a sample of Selenium (d).

In the following table (Table II.1), we present some values of the physical and chemical parameters of the elements Cu, In, Ga and Se used in the synthesis of Cu(In,Ga)Se_2 materials.

Table II.1: Physical and chemical properties of Cu, In, Ga and Se.

Parameters	**Cu**	**In**	**Ga**	**Se**
Atomic mass (g/mol)	63.546	114.818	69.72	78.96
Density at 300 K (g/cm^3)	8.96	7.31	5.907	4.79
Melting temperature (°C)	1083.4	156.61	29.78	217
Melting temperature (°C)	2595	2080	2403	685
Electronic conductivity (10^6/cm Ω)	0.596	0.116	0.0678	10^{-12}
Thermal conductivity (W/cm.K)	4.01	0.816	0.406	0.020
Ionization potential (1^{st}) (eV)	7.726	7.786	5.999	9.752
Electronegativity	1.9	1.78	1.81	2.4
Atomic radius (pm)	127.8	162.6	122.1	116

II.3. Fundamental properties of CIGS material

The CIGS material belongs to the family of chalcopyrites I-III-VI_2. These compounds are used in the composition of solar cells in thin layers as an absorber layer. This specificity makes them promising for photovoltaic applications for the following reasons:

- Their optical absorption coefficient is very high in the most intense part of the light spectrum, ($\alpha = 10^4$-10^5 cm^{-1}) [7,8]. This translates into a fairly substantial material saving compared to Si where a thickness of about 30 cm is required to achieve this absorption rate [9,10].
- The direct band gap of the material ranges from 1.01 to 1.68 eV [11].
- Make them in tow possibilities with n-type or p-type conductivity [12].
- Deposition can be done on inexpensive substrates such as soda-lime glass as well as on metallic or flexible substrates [13,14].
- Excellent stability to extremely high cosmic radiation [15-17].

Nevertheless, some characteristics of the CIGS run counter to its above-mentioned advantages, namely:

- A low band gap limits the open-circuit voltage. Consequently, it reduces the efficiency of solar cells.
- Some processes used for their deposition in thin layers and allowing good conversion efficiency are expensive and complex compared to those used in the other materials.
- Chalcopyrite-based materials contain indium and gallium, which are considered rare elements. The scarcity of these elements makes their acquisition expensive.

The chalcopyrite I-III-VI_2 materials have been widely studied in the literature and mainly those of the Cu-In-Se ternary system which is known as the basis of the Cu-In-Ga-Se quaternary system. This state of knowledge will therefore mainly focus on the well-established and practically indisputable results of the $CuInSe_2$ material and consequently of the $CuIn_{1-x}Ga_xSe_2$ compounds. It should be noted that Ga and In are chemically very similar, because the substitution of Ga instead of In does not dramatically change the parameters of the material [18].

The Chalcopyrite CIGS materials have two main families and the semiconductors we use in our work belong to the first family which is composed of a first column element, a third column element and an element of the sixth column of periodic table of the elements I-III-VI_2 as seen in Fig. II.2 [19].

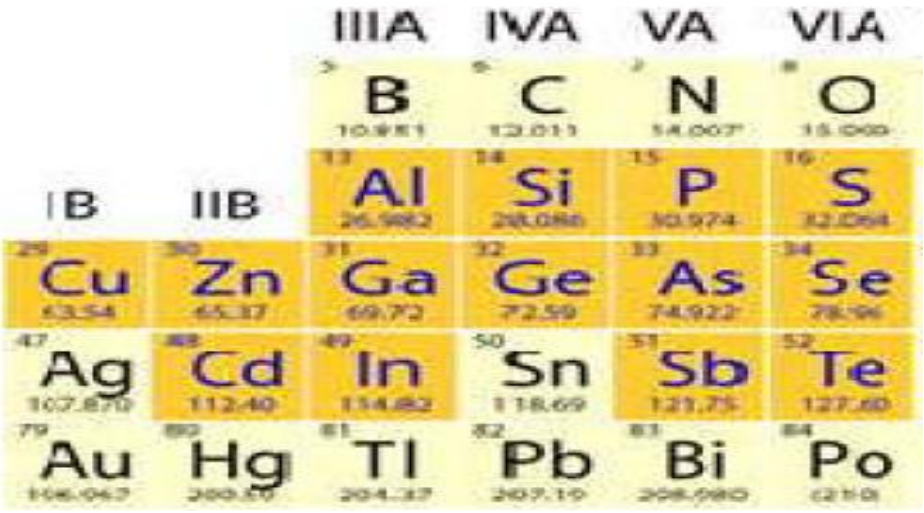

Fig. II.2: Chalcopyrite elements as indicated in the Periodic table.

II.4. Crystal structure of CIGS material

The $CuInSe_2$ and $CuGaSe_2$ are materials form the alloy of $Cu(In,Ga)Se_2$, belong to the I-III-VI_2 family which has a tetragonal structure of chalcopyrite. $CuInSe_2$ based chalcopyrites have a cubic zinc blende structure, also called sphalerite like ZnSe. Each Se atom is tetrahedrally bonded to two Cu and In atoms, while Cu or In atoms is surrounded by four Se atoms. The Cu-Se bond length is 2.43 Å and the In-Se bond length is 2.57 Å, giving a tetragonal distortion of unity of 0.3% [20].

For CIGS material, the group III atom sites are filled by either In or Ga atoms, in varying proportions based on the alloys composition. Both of these forms are depicted in Fig. II.3.

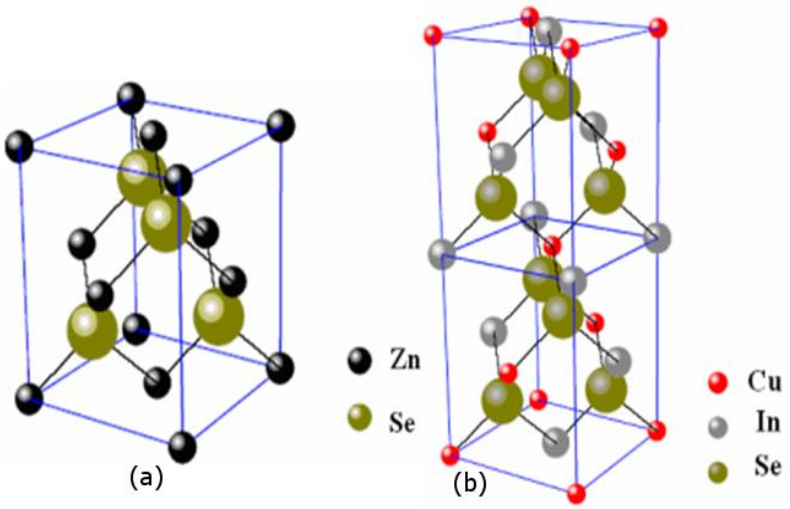

Fig. II.3: Sphalerite structures (a), chalcopyrite structures (b).

The incorporation of Ga into the $CuInSe_2$ ternary system can alter the electronic band structure, carrier concentration, chemical reactions and growth mechanisms. In the CIGS, the group III atom sites are occupied by In or Ga atoms, in proportions depending on the atomic composition x = [Ga]/([Ga]+[In]) of the alloy.

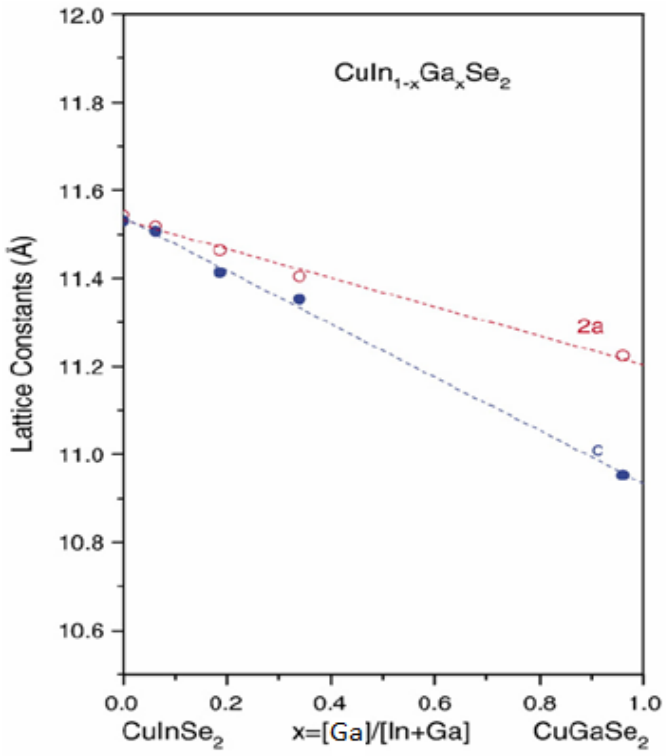

Fig. II.4: Variation of lattice parameters 2a and c of thin film CIGS as a function of Ga composition x.

Fig. II.4 shows the variations of the lattice parameters a and c of the $CuIn_{1-x}Ga_xSe_2$ thin layers decreasing almost linearly with the composition x of Ga, following the substitution of the smaller atoms of Ga instead of the atoms of In [21]. When this quasi-linearity is respected, we say that Vegard law is verified [22], therefore, these compounds can be assimilated to solid solutions.

II.5. Optical properties

Maximum light absorption across the entire solar spectrum is one of the most important properties of an absorbent layer. The CIS, CGS chalcopyrites and their alloys in thin layers are distinguished from other photovoltaic materials (CdTe, GaAs, CdS…etc.) by a very high optical absorption coefficient (10^4 to 10^5 cm^{-1}) making it possible to obtain high efficiency with minimal material thickness (1 to 2 µm). So, in order to manufacture cells at a lower cost, the CIGS alloy is very interesting because it requires a reduced amount of material. For various

x = [Ga]/([Ga]+[In]) ratios, Fig. II.5 shows the variation of the coefficient of absorption of CIGS thin films as a function of incident photon energy hν [23]. Therefore, the absorption coefficient α is calculated from the following equation [24]:

$$\alpha = \left(\frac{1}{d}\right)\ln\left[\frac{\left(1-R^2\right)}{2T} + \left[\frac{\left(1-R^2\right)^4}{4T^2} + R^2\right]^{\frac{1}{2}}\right] \quad \text{(II.1)}$$

where:

- *d*: The layer thickness.
- *T*: The transmission.
- *R*: The reflectivity.

According to citation [25], a relation exists between the absorption coefficient and both the energy gap and the energy levels of the photons that are being absorbed.

$$\alpha = \frac{A}{h\nu}\left(h\nu - E_g\right)^{\beta} \quad \text{(II.2)}$$

where:

- E_g: The band gap.
- *A*: The constant.
- *h* is Planck's constant.
- *B* = 1/2: The case of ternary and quaternary compounds (CIS and CIGS).

The gap value may be obtained by extrapolating the linear part of the expression:

$$\left(\alpha h\nu\right)^2 = A\left(h\nu - E_g\right) \quad \text{(II.3)}$$

The mole fraction *x* = [Ga]/([Ga]+[In]) represents the rate of gallium atoms which replace the atoms of indium in the structure. So, the CIGS have a direct gap and the addition of gallium in the crystalline structure makes it possible to vary the gap between 1.01 eV and 1.68 eV according to the value of the molar fraction *x*.

The band gap of CIGS is varying between the gap of CIS (*x* = 0) and the band gap of CGS (*x* = 1), according to the following equation [26]:

$$E_g\left[eV\right] = 1.010 + 0.626\,x - 0.167\,x\left(1-x\right) \quad \text{(II.4)}$$

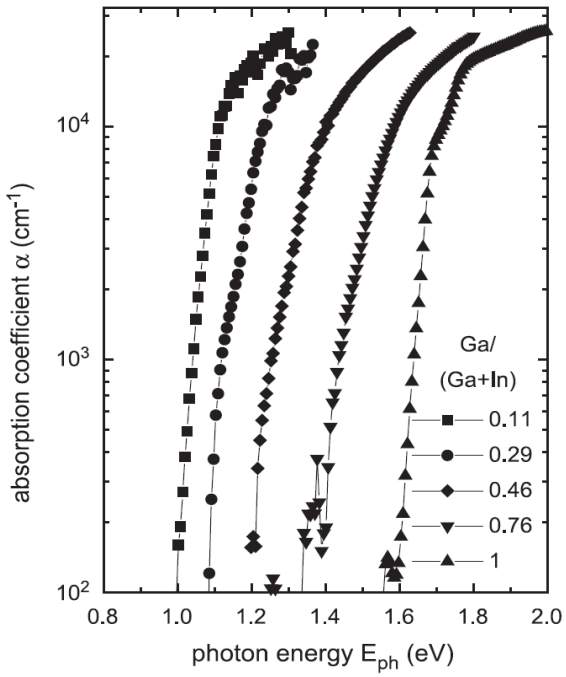

Fig. II.5: CIGS optical absorption coefficient as a function of photon energy *hv* and $x = [Ga]/([Ga]+[In])$ ratio.

The band gap is related to photon wavelength by:

$$E_g[eV] = \frac{1.24}{\lambda(\mu m)} \qquad \text{(II.5)}$$

The optical properties of CIS absorber layers have been extensively studied by several research groups [27]. So, the absorption coefficient of CIGS, CIS is very high and greater than 10^{-5} in the visible and near infrared range (Fig. II.6).

II.6. Different defects in CIGS

The characteristics of semiconductor materials are strongly influenced by defects. Often these impurities or imperfections in the lattice act as a bad factor, therefore a high concentration of defects decreases the possibility of carrier transport, thus reducing the conversion efficiency [28].

The nature of the defects for certain solids is quite well known. Many important properties of solids are determined from the impurities. The conductivity of some semiconductors may be entirely due to chemical impurities present in the crystal. Defects and impurities are created inside the band gap, generally a defect state is shallow if the energy level is close to the minimum of the conduction band or the maximum of the valence band. Otherwise, it is called deep level.

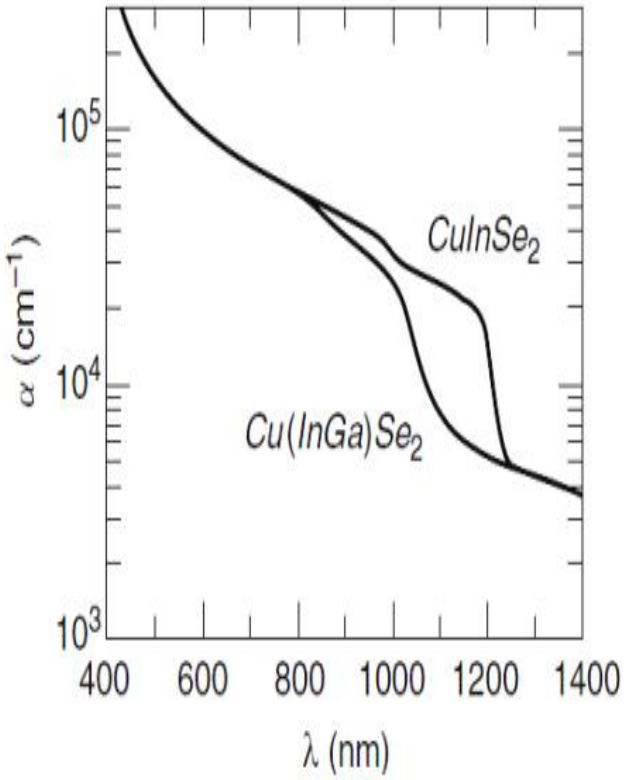

Fig. II.6: Absorption coefficient of $CuInSe_2$ and $CuIn_{0.7}Ga_{0.3}Se_2$ as a function of wavelength.

The reference [29] suggests that the deep levels act as traps for free carriers and capture the carriers introduced by doping. In order to introduce shallow levels into the material or eliminate deep levels, it is crucial to understand and regulate the defects and impurities that create these energy levels. Crystal defects can be classified into four categories.

- ✓ Point defect (0D).
- ✓ Line defect (1D).
- ✓ Surface defect (2D).
- ✓ Volume defect (3D).

II.6.1. Point defects

When one or more crystalline atoms move from their initial lattice site or when foreign atoms enter the crystal's interstitial position, a point defect is created. Therefore, there are three ways that a point defect can occur, as listed below:

- Least one original crystal atom is absent from its corresponding lattice position;
- Same crystal, one or more original atoms are moved from their original lattice site to the interstitial position;

- Crystalline solid's interstitial region contained one or more alien atoms;
- Crystal's initial atom was replaced by one or more foreign atoms, which then took up residence in the interstitial space.

The three main classifications for point defects are vacancy, interstitial, and substitutional defects. However, self-interstitial defects can sometimes be categorized differently. In the case of ionic crystals, Schottky and Frenkel defects can occur. These defects are nothing but the combination of two different types of the four basic types of point defects discussed above. The next section covers the specific details of these point defects.

a) Vacancy

A vacancy defect is created when an atom is missing from its original lattice location, resulting in an empty lattice site. Vacancy is a zero-dimensional point defect, just like other types of point defects. The presence of a vacancy defect can cause tension between nearby atoms. The density of a crystalline solid can be reduced due to vacancy defects because there are fewer atoms present. In the ternary structure ABC_2, V_A, V_B and V_C can exhibit this type of defect.

b) Interstitial

An atom occupying an interstitial location in a lattice structure creates an interstitial point defect. This interstitial atom can come from either the same crystal or another one entirely, resulting in two different forms of interstitial defects:

- Self-interstitial defect occurs when an atom from the crystal lattice moves to occupy an interstitial space within the same solid.
- Foreign atom taking up residence in the interstitial location is known as an interstitial defect. This type of defect is presented by A_i, B_i, Ci.

c) Substitutional

A substitutional defect happens when a different kind of atom fills the empty space left by the original atom in a crystalline solid's lattice site. Contrary to interstitial defects, foreign atoms should not occupy the interstitial position but rather the lattice site, as seen below. The foreign atom could have a similar size or a different size. The surrounding atoms can still be in tension or compression depending on the size of the substituted foreign atom. These defects are illustrated by A_B A_C, B_A B_C, C_A C_B. A crystal lattice made up of the atom types A and B is illustrated in the Fig. II.7. A various kinds of point defects can be present.

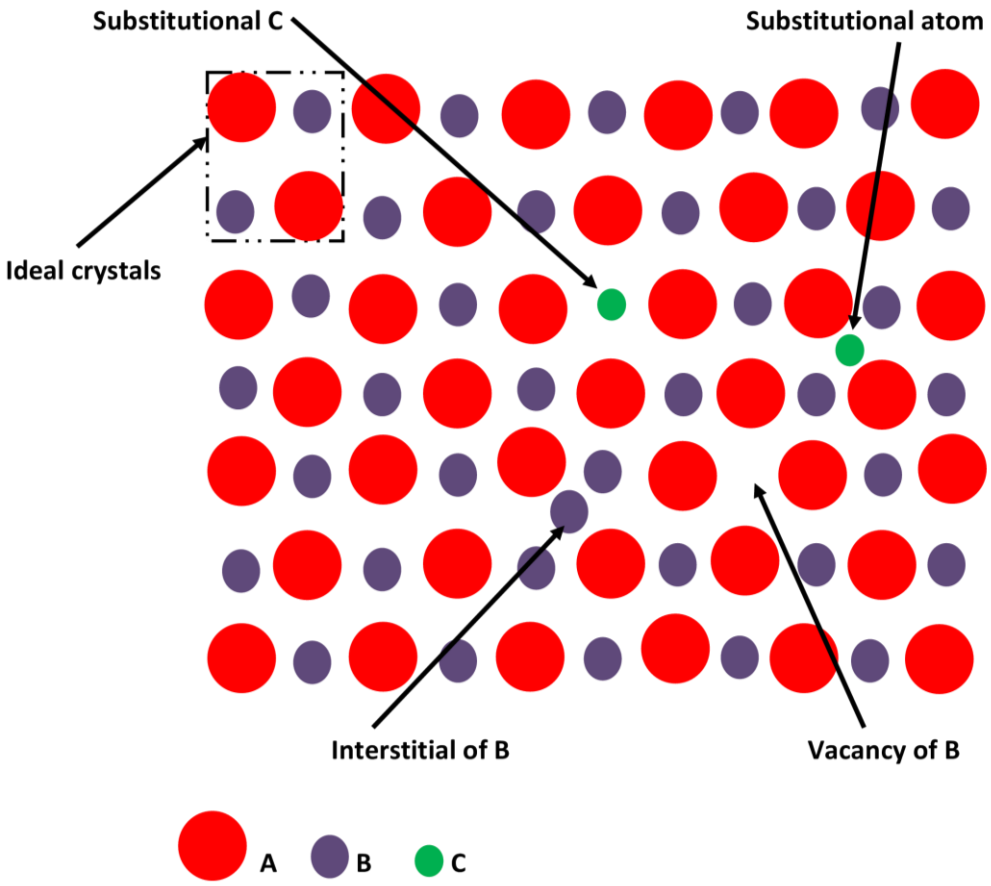

Fig. II.7: Point defects in the crystal lattice.

II.6.2. Line defect

In the 1930, Orowan, Polanyi and Taylor [30] proposed that shearing of a crystal could occur through the propagation of elementary linear defects called dislocations. The dislocation is a linear defect corresponding to a discontinuity in the organization of the crystalline structure [31], there are two types screw and edge dislocations, for example, taking a CIGS wafer and applying a force on each side, the crystal deformation will be due to the dislocation. This defect is depicted in Fig. II.8.

II.6.3. Surface defect

The 2D defects are produced from manufacturing methods, it is a so-called extrinsic defect, for example twin and grain boundary GB, the twin boundary is a group of two or more identical crystals (same crystallographic orientations), whose orientation relative to each other comes from a symmetry operation. The Fig. II.9 shows this defect.

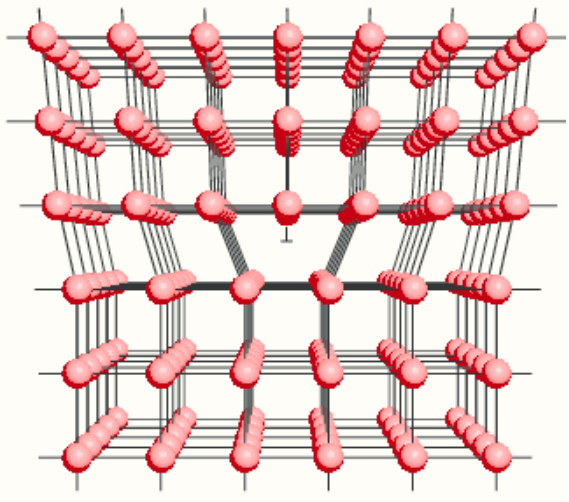

Fig. II.8: Crystal deformation due to the dislocation.

A grain boundary refers to the interface between two crystals of the same chemical composition and crystallographic structure, but with different orientations. These boundaries can be visualized through graphical representations, such as the one shown in Fig. II.10, which depicts grains and grain boundaries in a polycrystalline material. Grain boundaries are generally categorized into two types, Horizontal and Vertical. Horizontal boundaries may decrease the short circuit current by reducing electron lifetime and increasing recombination site density. On the other hand, Vertical grain boundaries can decrease both the short circuit current and the open circuit voltage. If these boundaries intersect, they can lead to an increase in the reverse saturation current [32].

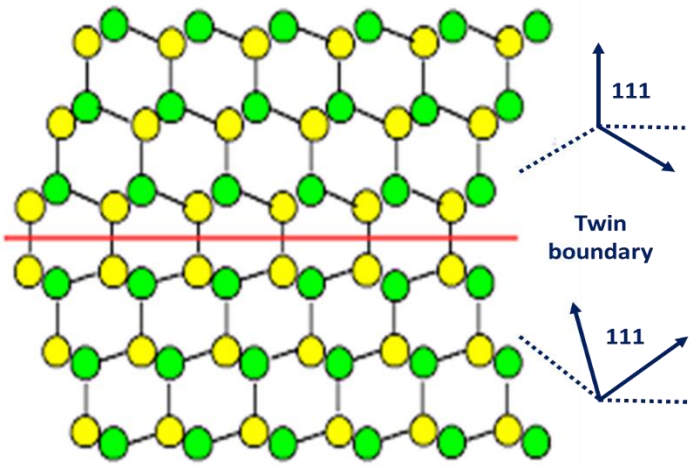

Fig. II.9: Schematic of a twin boundary.

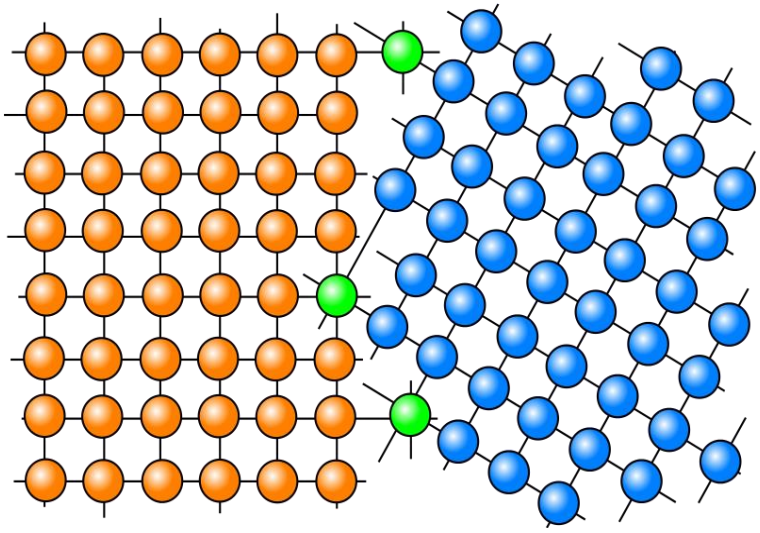

Fig. II.10: Grain boundary between two crystals.

II.6.4. Volume defect

Replacing a part of the crystal with a different compound creates a three-dimensional defect. This foreign compound may differ from the crystal in terms of its crystallographic nature. There are various types of volume defects, including cracks, voids, inclusions, and precipitates. Dislocations can lead to a decrease in the lifetime of minority carriers. There are two types of precipitates, as shown in Fig. II.11.

- **Coherent precipitates:** Show crystallographic continuity and bonding with the matrix and precipitates (matrix and precipitate lattices are similar but their lattice parameters may be different resulting in elastic distortion).
- **Incoherent precipitates:** There is no compatibility or no bonding between the matrix and the precipitates.

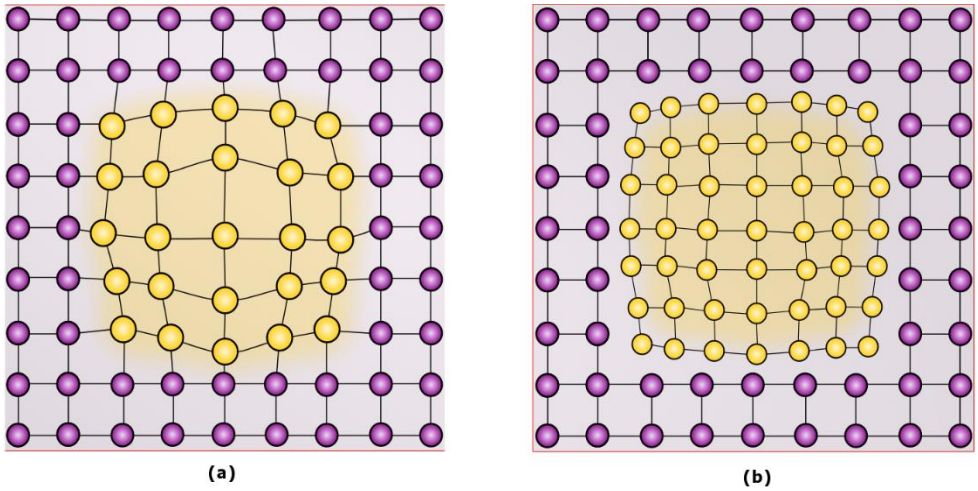

Fig. II.11: (a) Coherent precipitates, (b) Incoherent precipitates.

II.6.5. Defect energy levels

The stoichiometry has a direct impact on the formation energy of the various defects. So this various defects are accounting for the individual elements' chemical potentials. The following is the order in which these defects are produced in $CuInSe_2$, according to Zhang et *al*. [33]:

- V_{Cu} <Cu_{In}<V_{In}<Cu_i<In_{Cu} (Cu rich; In rich; n type).
- V_{Cu} <Cu_{In} <In_{Cu}<Cu_i<V_{In} (Cu rich; In rich; p type).
- V_{Cu} <V_{In}<In_{Cu}<Cu_{In}<Cu_i (Cu poor; In rich; n type).
- V_{Cu}<In_{Cu}<V_{In}<Cu_{In}<Cu_i (Cu poor; In rich; p type).
- Cu_{In}<V_{In}<V_{Cu}<Cu_i<In_{Cu} (Cu rich; In poor; n type).
- Cu_{In}<V_{Cu}<V_{In}<Cu_i<In_{Cu} (Cu rich; In poor; p type).

Based on previous studies [34,35], energy levels ranging from 10-30 meV have been measured electronically [24] using optical measurements [36-38] in the case of n-type and indium-rich copper indium gallium selenide (CIGS). These energy levels have been attributed to the substitution of a copper atom by an indium atom, forming In_{Cu}. Additionally, in luminescence studies of both n-type and p-type CIGS, a level of 60-80 meV was observed, which was identified as a selenium vacancy V_{Se} [39]. The copper vacancy introduces a surface acceptor level, with a value of 20-40 meV in n-type CIGS. Furthermore, this gap can also introduce an energy level of 160 meV [39].

Defects are highly likely to occur in CIGS materials due to their broad tolerance for stoichiometry. So, the complex defects can occur in addition the vacancy and substitution. When V_{Cu} and In_{Cu} are present simultaneously in CIGS material, they can form an ordered defect compound (ODC) [39]. This compound has unique electrical properties and crystal structure that differentiate it from the standard CIGS structure. ODC have captured the attention of researchers who are studying the performance and stability of photovoltaic devices. Several studies have explored the properties and formation of ODC, highlighting their potential impact on device performance and the effect of processing conditions on their sensitivity.

The energy gap of CIS, CGS, and CIGS (x = 0.3) is presented in Fig. II.12 [33,40], along with the calculated theoretical energy levels of the defects found in those materials. Regarding the CIGS acceptor, the letter "M" refers to both gallium and indium atoms.

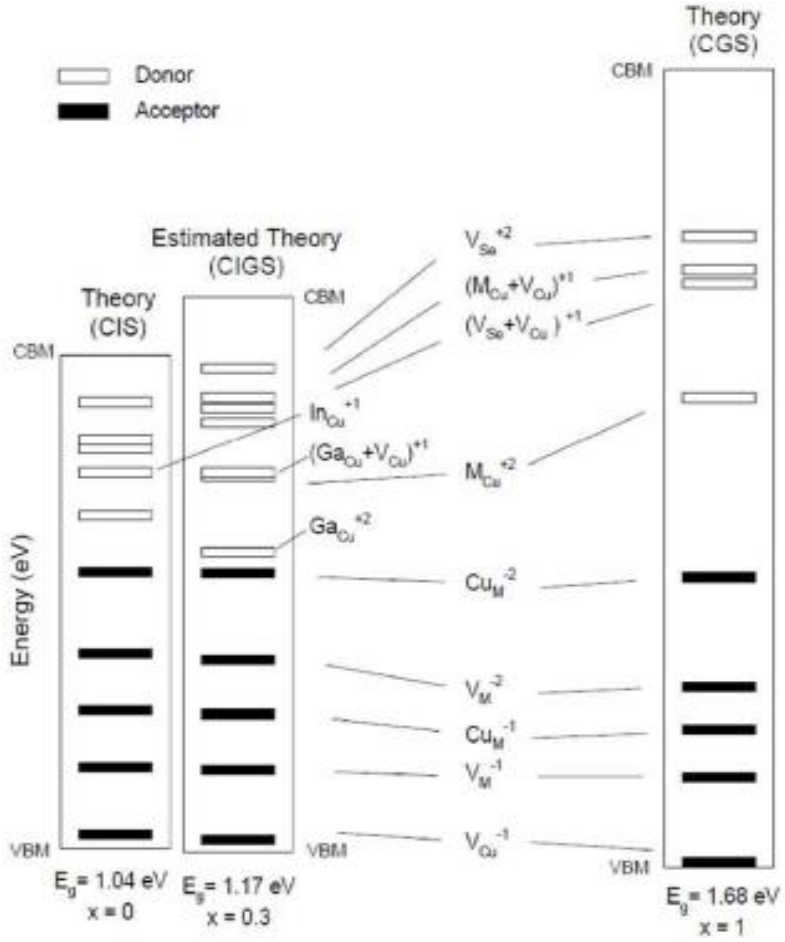

Fig. II.12: Different defects in band gap energy of CIS, CGS, and CIGS.

II.6.6. Electrical properties of $CuInSe_2$

Several researchers have studied the electrical properties of $CuInSe_2$, including the identification and characterization of defects in this material. As we mentioned before, homojunctions and heterojunctions can be made with this semiconductor, in other words, this material can be n or p type conductivity and this by excess or lack of selenium. On the other hand, $CuInSe_2$ exhibits excellent electrical stability in a wide stoichiometry band. Research has shown that by acting on the ratios (Cu/In) and Se/(Cu+In) one can change the type of conduction in the $CuInSe_2$ semiconductor, other work has shown that generally selenium atoms in $CuInSe_2$ behave as donors and thus lead to n-type conduction, $CuInSe_2$ layer that have excess indium and contain copper vacancies (V_{Cu}) are usually p-type. Table II.2 gathers the evolutions of the conduction types of the $CuInSe_2$ according to the ratios (Cu/In) and Se/(Cu+In) after deposition [41].

Table II.2 Type of conduction in $CuInSe_2$ according to ratios (Cu/In) and (Se/Cu+In).

$(Se/Cu+In)>1$		$(Se/Cu+In)<1$	
$(Cu/In)>1$	$(Cu/In)<1$	$(Cu/In)>1$	$(Cu/In)<1$
p type with low resistivity	***p*** type with medium resistivity or ***n*** type with high resistivity	***p*** type with low resistivity	***p*** type with high resistivity or ***n*** type with low resistivity

II.7. CIGS thin film deposition processes

Thin layer deposition refers to all the techniques that make it possible to deposit a thin layer or a thin film of material on a substrate or on other layers, some techniques make it possible to achieve high optical conversion efficiencies in the laboratory, but the high cost of the process and its complex implementation limit their large scale development.

On the other hand, other techniques lead to lower conversion efficiency by low cost processes that are easily transposable to an industrial scale. On the other hand, the structural, optical and electrical properties depend on the composition of the thin layer. These properties are strongly related to growth conditions. So, the choice of the deposition process is therefore essential to obtain compounds that make it possible to achieve very high efficiency. Several deposition techniques are used today for the development of CIGS layer, these techniques fall into two broad categories, physical or chemical process.

II.7.1. Physical deposition

Physical deposition consists of using the vapors of the material to be grown to produce a thin film on any substrate. So, these processes mainly include: evaporation, laser ablation and sputtering in all its forms.

II.7.1.1. Evaporation technique

Evaporation is a gradual passage from the liquid state to the gassy state. In the field of micro-manufacturing, evaporation consists of evaporating or sublimating the material to be deposited by heating it to high temperature.

As soon as the melting temperature is exceeded, it turns out that the vapor pressure of the material is significantly higher than the residual pressure in the enclosure (Around 10^{-8} to 10^{-6}

mbar). Then atoms of the material escape and propagate in a straight line to the substrate.

There will be a stay of the atom on the surface with energy exchange and if the surface is noticeably colder than the atom there is definitive condensation. Therefore, the heating in evaporation is done by different methods, we quote:

- Heating by resistance: evaporation by Joule effect, thermal evaporation;
- Heating by electron beam: electron shelling, cathode sputtering;
- Heating by laser beam: evaporation by laser ablation.

A. Thermal evaporation technique

The vapor of the material to be deposited in a thin layer is produced thermally, by heating. This can be achieved in various ways, in particular by resistance, taking advantage of the Joule effect, a crucible in which the material to be evaporated is placed, brought to incandescence by a high electric current and causes it to melt (Fig. II.13), in the photovoltaic field, this method has been used for the deposition of thin layers of CIS, FeS_2, SnS, CdS and (Ag,Cu)(In,Ga)Se_2 [42].

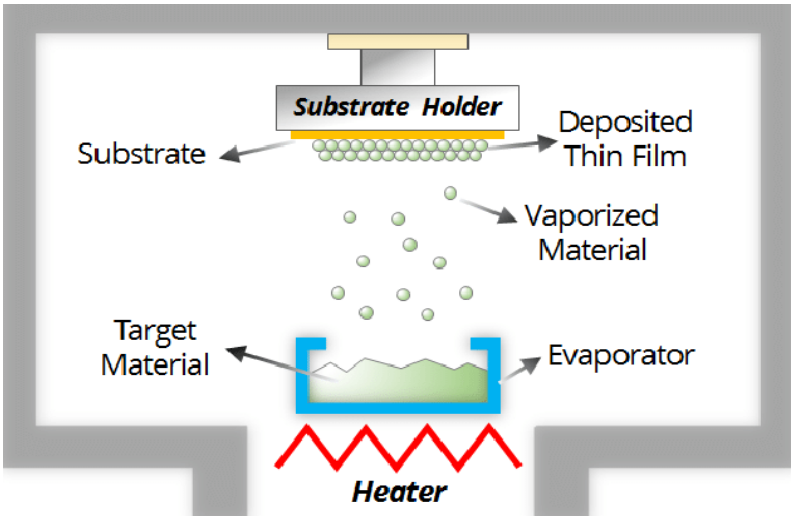

Fig. II.13: Thermal evaporation deposition.

B. Co-Evaporation technique

This technique has the advantages of easy control of the evaporation rate of the elements and the possibility of making very thin layers. It is very simple and simply consists in heating the Cu-(In-Ga)-Se materials which will be deposited on the substrate. On a rear contact deposited on ordinary glass, maintained at a temperature between 450 and 550°C, Se is simultaneously deposited, the crucible of which is heated between 300 and 320°C, the copper is heated to 1360°C and the indium is heated to 900°C. In the first phase of the deposition, the

temperature of the substrate must be raised to 550°C so that the layer of $CuInSe_2$ is rich in Cu, in the second phase, the temperature of the substrate must rise to 450°C, so that the $CuInSe_2$ layer is poor in Cu. The maximum deposition temperature is restricted by the glass's softening point. Moreover, research has indicated that as the temperature increases, the efficiency distribution widens [29]. A schematic of the Co-Evaporation system is illustrated in Fig. II.14.

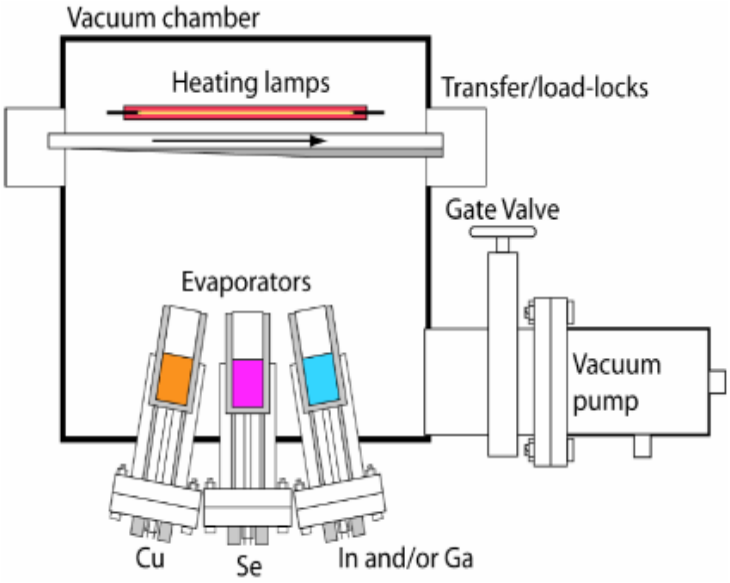

Fig. II. 14: Schematic of co-Evaporation system.

II.7.1.2. Spraying

The principle of spraying involves bombarding the surface of a solid with a beam of neutral or charged particles. This leads to the ejection of constituents of the target in the form of atoms, ions, and neutral or charged aggregates, which are then deposited onto the substrate and form a thin layer [43].

A. Magnetron sputtering technique

This technique is desirable for depositing $CuInSe_2$ layers on large surfaces. In this technique, the $CuInSe_2$ to be deposited, called the target material, is introduced into a vacuum chamber, in the form of a pellet a few millimeters thick (powder) or else in the form of an ingot [44]. Its principle consists in tearing of $CuInSe_2$ atoms via plasma. This plasma is obtained by means of an electrical discharge in a gas at low pressure, this gas is generally Argon (Ar), and the ions of the gas constituting the plasma are accelerated towards the target via the applied potential, thus bombarding the target and eject atoms of copper, indium and selenium. These

atoms are ejected in all directions in space and part of them will be deposited on a substrate placed above the target to form a $CuInSe_2$ layer (see the Fig. II.13).

The layer obtained is subsequently subjected to appropriate heat treatments which make it possible to obtain the $CuInSe_2$ phase. $CuInSe_2$ layers deposited by this technique have a high grain size and a low defect density, and the photovoltaic cells made from these latter layers reach efficiencies of around 11.3% [45]. This technique has been used to deposit thin layers of compound materials such as $Cu(In,Ga)Se_2$ [46]. In the chapter 5, we will provide more explanation about this technique.

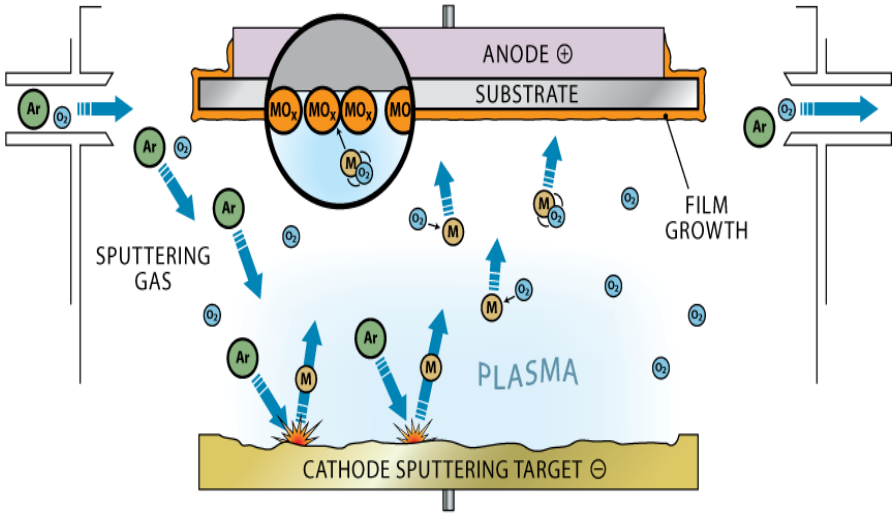

Fig. II.15: Schematic of the sputtering reactor.

B. Spray

The spray deposition was introduced by Chamberlin and Skarman [47] in 1966 for the deposition of thin films of CdS, since then the process has been used for the deposition of various materials such as: SnO_x, ITO, ZnO and others. The CIS, CGS and CIGS have also been developed by this technique [48]. They are prepared from aqueous acid solutions or aqueous ethanoic $CuCl_2$, $InCl_3$ and $GaCl_3$ solutions. So, these solutions are then sprayed onto a preheated substrate at a constant temperature of 350°C to 400°C (Fig. II.16). The films obtained then undergo annealing at temperatures ranging from 450°C to 500°C in various environments such as H_2, H_2Se. Although this technique is simple, inexpensive, does not require a vacuum and that substrates with complex geometries can be coated, the efficiency obtained are mediocre compared to those achieved by other techniques.

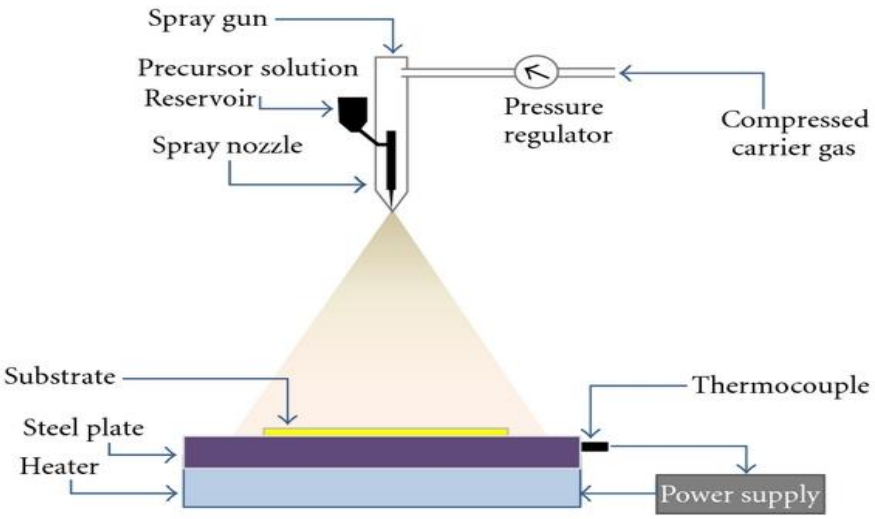

Fig. II.16: Schematic diagram of spray technique.

II.7.2. Chemical deposition

In the physical process, a thin layer is created through the condensation of the material's vapor phase, whereas in the chemical process, the thin layer is formed by a chemical reaction between the gaseous products in the vapor phase and the substrate, triggered by an activation energy such as thermal energy. Among the chemical techniques we can cite:

II.7.2.1. Chemical vapor deposition (CVD)

Chemical vapor deposition (CVD) is a vacuum deposition method for thin films from gaseous precursors. In a typical CVD process, the substrate is exposed to one or more volatile precursors which react and decompose on the surface of the substrate to produce the desired layer. During this process volatile by products are also generated, which are removed by a gas flow through the reaction chamber (Fig. II.17). The CVD deposition is a process used to produce high purity, high performance solid materials. However, it has the following disadvantages: the films are not very dense and are often contaminated by highly reactive gases resulting from the chemical reaction (hydrogen, fluorine, chlorine, etc.). However, not all materials can be deposited by CVD and the deposition system is a relatively hard.

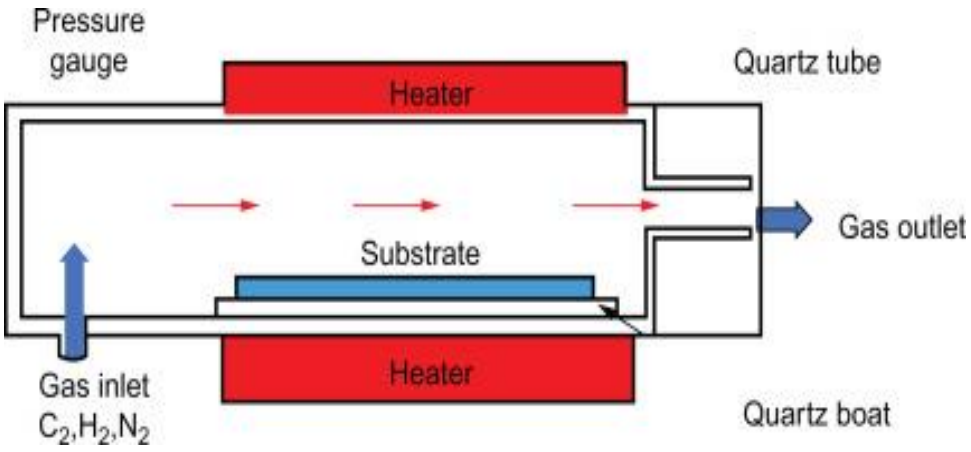

Fig. II. 17: Schematic of CVD technique.

II.7.2.2. Metal organic chemical vapor deposition

The metal organic chemical vapor deposition (MOCVD) is a crystal growth technique in which the elements to be deposited in the form of organometallics or hydrides are brought towards the wafers substrate by a carrier gas (Fig. II.18). However, this growth technique is particularly used in the III-V semiconductor industry because of the good reproducibility and the high growth speeds accessible. This method has been applied successfully for deposit CGS on GaAs layer [49].

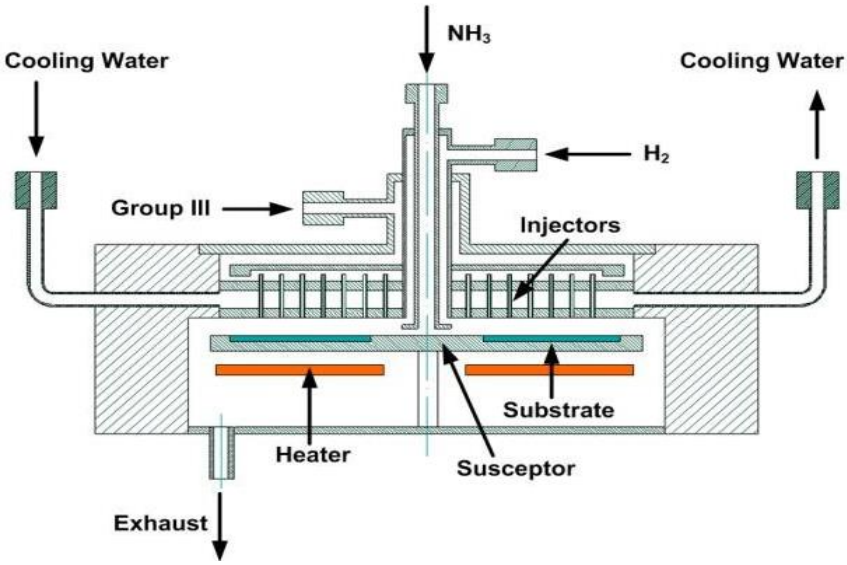

Fig. II.18: Schematic of MOCVD reactor.

II.7.2.3. Electro-deposition

Electro-deposition is a redox reaction (reduction–oxidation) that is triggered by a current source. So, the electrolysis bath contains the appropriate metal salt, the substrate (working

electrode) on which the deposition must take place and the electrolyte in which it is immersed (Fig. II.19).

The substrate is connected to the negative pole of the current source, while the other pole is connected to an electrode formed by the metal to be deposited. Under the action of the current, the metal ions are deposited on the substrate and form a metallic film.

Calixto et *al.* [50] used the technique to deposit CIS and CIGS films whose stoichiometry was improved after salinization at 550°C. In order to reduce the manufacturing cost of photovoltaic panels based on CIS and CIGS. Lincot et *al*. [51] have successfully developed thin layers of CIGS by added Ga into the CIS and the efficiency up to 11%.

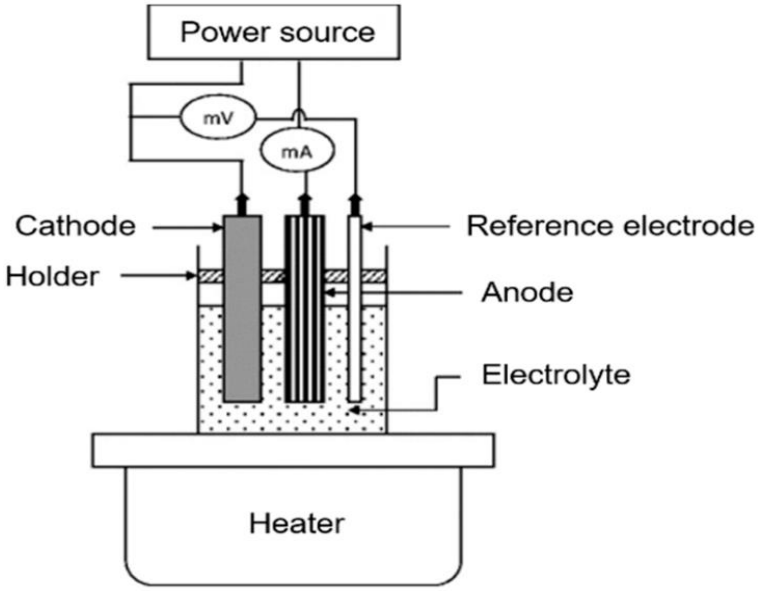

Fig. II.19: Schematic of electro-deposition system.

II.8. Conclusion

In this chapter, we provided a thorough bibliographic analysis of essential characteristics of the Cu(In,Ga)Se_2 material, including its crystalline structure, electronic and the optical properties. Then, we provided concise explanations of the various crystal defects (dislocations, grain boundaries), as well as point defects (vacancies, interstitial atoms, substitutional defects). In the last section we have discussed two most popular deposition processes used to deposit CIGS thin films, namely the chemical deposition and the physical deposition.

These qualities have made the CIGS material a preferred semiconductor for photovoltaic applications, allowing for the employment of this semiconductor as a basic material in the production of electronic components to satisfy particular industrial needs.

References

[1] Wu, J. L., Hirai, Y., Kato, T., Sugimoto, H., Bermudez, V. (2018). New world record efficiency up to 22.9% for Cu(In,Ga)$(Se,S)_2$ thin-film solar cells. in 7th World Conference on Photovoltaic Energy Conversion (WCPEC-7), pp.10-15.

[2] Bouloufa, A. (2007). Etude et Caractérisation des Semiconducteurs Ternaires et Quaternaires CuIn1-xGaxSe_2 par Spectroscopie Photoacoustique. These de Doctorat, Universite Ferhat Abbas-Setif Ufas, Algerie.

[3] Mickelsen, R., Chen W. (1981). Development of a 9.4% efficient thin-film $CuInSe_2$/CdS solar cell. 15th photovoltaic specialist's conference, pp. 800-804.

[4] https:// fr.wikipedia.org/wiki/Cellule CIGS. Accessed May 15 2021.

[5] https://www.usgs.gov/centers/nmic/indium-statistics-and-information, Accessed April 09 2021.

[6] Gallium. Encyclopædia Britannica, Encyclopædia Britannica, Inc., 16 Nov. 2021, https://www.britannica.com/science/gallium.

[7] Schön, J., Alberts, V., Bucher, E. (1997). Structural and optical characterization of polycrystalline $CuInSe_2$. Thin Solid Films, 301(1-2), 115–121. doi:10.1016/s0040-6090(97)00060-6

[8] Boustani, M., Bekkay, T. (1997). Characterization of $CuInTe_2$ thin films prepared by flash evaporation. Semicond. Sci. Technol. 12 (1997) 1658–1661. UK.

[9] Xu, J., Yao, X., Feng, J. (2002). The influence of the vacuum annealing process on electrodeposited $CuInSe_2$ films. Solar Energy Materials and Solar Cells, 73(2), 203–208. doi:10.1016/s0927-0248(01)00125-8.

[10] Shen, F. Y., Que, W., Cheng, L., Huang, Y. W. (2010). Preparation and Characterization of $CuInSe_2$Thin Films Derived by Electrodeposition Process for Solar Cells. Ferroelectrics, 402(1), 102–109. doi:10.1080/00150191003708802

[11] Schön, J.H, Bucher, E. (1999). Comparison of point defects in $CuInSe_2$ and $CuGaSe_2$ single crystals. Sol. Energy Mater. Sol. Cells., vol. 57, no.3, pp.229-237.

[12] Bouloufa, A., Djessas, K., Todorovic, D. (2009). Structural and optical properties of Cu(In,Ga)Se_2 grown by close-spaced vapor transport technique. Materials Science in Semiconductor Processing, 12(1-2), 82–87. doi:10.1016/j.mssp.2009.07.010.

[13] Deepa, K. G., Jayakrishnan, R., Vijayakumar, K. P., Sudha Kartha, C., Ganesan, V. (2009). Sub-micrometer thick $CuInSe_2$ films for solar cells using sequential elemental evaporation. Solar Energy, 83(7), 964-968. doi:10.1016/j.solener.2009.01.016.

[14] Murali, K. R., Vinothini, C., Srinivasan, K. (2012). Characteristics of pulse plated copper indium telluride films. Materials Science in Semiconductor Processing, 15(2), 194-198. doi:10.1016/j.mssp.2012.02.006.

[15] Yamaguchi, M. (1995). Radiation resistance of compound semiconductor solar cells. Journal of Applied Physics, 78(3), 1476–1480. doi:10.1063/1.360236.

[16] Dıaz, R., Martín, T., Rueda, F. (2000). Composition effects on structural and optical infrared properties of $CuIn_{0.5}Ga_{0.5}Se_2$. J. Appl. Phys, vol. 88, no. 4,pp.1776-1783.

[17] A. N. Tiwari, M. Krejci, F. J. Haug, and H. Zogg, "12.8% efficiency Cu (In,Ga) Se_2 solar cell on a flexible polymer sheet," Prog. Photovolt. Res. Appl, vol. 7, no. 5, pp.393-397, 1999.

[18] D. Rudmann, (2004). Thèse de PhD, Suisse Federal Institute of Technology Zurich, Suisse.

[19] Elbar, M. (2018). Etude par simulation numérique d'une cellule solaire en CIGS à multi-jonction par le logiciel Tcad Silvaco, Thèse de doctrat, Université Mohamed Khider-Biskra.

[20] Shay, J., Wernick, J. (1975). Ternary Chalcopyrite Semiconductors, growth, electronic Properties and Applications. Pergamon Press, pp. 15.

[21] Jaffe, J. E., & Zunger, A. (1983). Electronic structure of the ternary chalcopyrite semiconductors $CuAlS_2$, $CuGaS_2$, $CuInS_2$, $CuAlSe_2$, $CuGaSe_2$, and $CuInSe_2$. Physical Review B, 28(10), 5822-5847. doi:10.1103/physrevb.28.5822.

[22] Vegard, L. (1921). Recent results of north light investigations and the nature of the cosmic electric rays. Lond.Edinb. Dublin Philos. Mag. J. Sci., vol. 42, no. 247, pp.47-87.

[23] Bauera, G.H., Braggemann, (2005). Thin Solid Films, pp. 480-481.

[24] H. Neumann, W. Horig, E. Reccius, Solid State Comm. vol. 27, pp. 449, 1978.

[25] Pankove, J. I., Tomasetta, L., Williams, B. F. (1971). Identification of Auger Electrons in GaAs. Physical Review Letters, 27(1), 29-32. doi:10.1103/physrevlett.27.29.

[26] Bouabdelli, M.W., Rogti, F., Maache, M., Rabehi A. (2020). Performance enhancement of CIGS thin-film solar cell, Optik. 216 164948.https://doi:10.1016/j.ijleo.2020.164948.

[27] Gray, J. L. (2011). Chapter 3: The Physics of the Solar Cell, Handbook of Photovoltaic Science and Engineering, John Wiley and Sons Inc., pp. 82-128.

[28] Benosman, M., Bouchaour, M., Dujardin, F., Benyoucef, B. 2003. Le Rôle Du Mécanisme de Recombinaison sur Les Performances Photovoltaïques des cellules solaires de type CIGS. Rev. Energ. Ren. ICPWE, pp. 103-106.

[29] Abdo, F. (2007). Croissance de couches minces de silicium par épitaxie en phase liquide à basse température pour applications photovoltaïques. Thèse de doctorat, Lyon, France.

[30] Hirth, J. P., Lothe, J. (1982). Theory of dislocations (Vol. 1). John Wiley & Sons.

[31] http:// fr.wikipedia.org/wiki/Cellule CIGS, Accessed April 08 2013.

[32] Sozzi, G., Troni, F., Menozzi, R. (2010). Numerical analysis of the effect of grain size and defects on the performance of CIGS solar cells, CS Mantech Confe, Portland, Oregon, USA pp. 353-356.

[33] Zhang, S. B., Wei, S.-H., Zunger, A., Katayama-Yoshida, H. (1998). Defect physics of theCuInSe2chalcopyrite semiconductor. Physical Review B, 57(16), 9642-9656. doi:10.1103/physrevb.57.9642.

[34] Rincón, C., Bellabarba, C. (1986). Optical properties of copper indium diselenide near the fundamental absorption edge. Physical Review B, 33(10), 7160-7163. doi:10.1103/physrevb.33.7160.

[35] Hollings, R. E. (1985). The Conference Record of the Eighteenth IEEE Photovoltaic Specialists Conference IEEE, New York, 1409.

[36] Wasim, S. M., Noguera, A. (1984). Transport properties of n-type $CuInSe_2$. Physica Status Solidi (a), 82(2), 553–559. doi:10.1002/pssa.2210820228.

[37] Rincón, C., González, J., Sánchez Pérez, G. (1983). Luminescence and impurity states in CuInSe2. Journal of Applied Physics, 54(11), 6634–6636. doi:10.1063/1.331900.

[38] Rincón, C., Pérez, G. S. (1986). Degeneracy effect on the optical properties of CuInSe2. Solar Cells, 16, 363-368. doi:10.1016/0379-6787(86)90096-7.

[39] Bouchama, I. (2012). Contribution à l'amélioration des performances des cellules solaires $CuIn_{1-x}$ Gax Se_2. Thèse de doctorat, Universite Ferhat Abbas Setif ufas, Algerie.

[40] Wei, S.-H., Zhang, S. B., Zunger, A. (1998). Effects of Ga addition to $CuInSe_2$ on its electronic, structural, and defect properties. Applied Physics Letters, 72(24), 3199-3201. doi:10.1063/1.121548.

[41] Bouraiou, A. (2009). Élaboration et caractérisation des couches minces $CuInSe_2$ parélectrodéposition. Thèse de doctorat, Universite Mentouri Constantine, Algerie.

[42] Simchi, H., McCandless, B. E., Kim, K., Boyle, J. H., Shafarman, W. N. (2013). Effect of Rapid Thermal Processing on the structural and device properties of (Ag,Cu)(In,Ga)Se_2 thin film solar cells. Thin Solid Films, 535, 102-106. doi:10.1016/j.tsf.2012.11.061.

[43] Clyne, T.W. (2001) 3.7.12. Metal Matrix Composites: Matrices and Processing. In: Mortensen, A., Ed., Encyclopedia of Materials: Science and Technology, Composites: MMC, CMC, PMC, Elsevier, New York, 1-14.

[44] A.N.Y. Samaan, S. Al-Saffar, S.M. Wasim, A.E. Hill, D.G. Armour, R.D. Tomlinson Nuovo Cimento, Italia, pp. 1784, 1983.

[45] Nakada, T., Migita, K., Niki, S., AkioKunioka. (1995). Microstructural Characterization for Sputter-Deposited of $CuInSe_2$ Films and Photovoltaic Devices. Japanese Journal of Applied Physics, 34(Part 1, No. 9A), 4715–4721. doi:10.1143/jjap.34.4715.

[46] Liu, J., Zhuang, D., Luan, H., Cao, M., Xie, M., Li, X. (2013). Preparation of Cu(In,Ga)Se_2 thin film by sputtering from Cu(In,Ga)Se_2 quaternary target. Progress in Natural Science: Materials International, 23(2), 133-138. doi:10.1016/j.pnsc.2013.02.006.

[47] Chamberlin, R. R., Skarman, J. S. (1966). Chemical Spray Deposition Process for Inorganic Films. Journal of The Electrochemical Society, 113(1), 86. doi:10.1149/1.2423871.

[48] Guo, Q., Ford, G. M., Hillhouse, H. W., Agrawal, R. (2009). Sulfide Nanocrystal Inks for Dense $Cu(In_{1-x}Ga_x)(S_{1-y}Se_y)_2$ Absorber Films and Their Photovoltaic Performance. Nano Letters, 9(8), 3060-3065. doi:10.1021/nl901538w.

[49] Orsal, G., Romain, N., Artaud, M.-C., Duchemin, S. (1999). Characterization of CuGaSe/sub 2/ thin films grown by MOCVD. IEEE Transactions on Electron Devices, 46(10), 2098–2102. doi:10.1109/16.792003.

[50] Calixto, M., Sebastian, P., Bhattacharya, R., Noufi, R. (1999). Compositional and optoelectronic properties of CIS and CIGS thin films formed by electrodeposition. Solar Energy Materials and Solar Cells, 59(1-2), 75-84. doi:10.1016/s0927-0248(99)00033-1

[51] Lincot, D., Guillemoles, J. F., Taunier, S., Guimard, D., Sicx-Kurdi, J., Chaumont, A., Kerrec, O. (2004). Chalcopyrite thin film solar cells by electrodeposition. Solar Energy, 77(6), 725–737. doi:10.1016/j.solener.2004.05.024.

Chapter III: Simulation of CIGS solar cell using SILVACO/Atlas software

Chapter III

Simulation of CIGS solar cell using SILVACO/Atlas software

III.1. Introduction

The primary aim of solar cells simulation is to achieve precise predictions of their performance and gain a deeper understanding of the fundamental physical mechanisms that underlie their operation. This enables researchers and engineers to optimize their design, enhance their efficiency and create innovative materials and technologies. Simulation results provide valuable insights into the intricate interactions between materials, light, and electrical fields in a solar cell, aiding in the identification of potential efficiency losses. Furthermore, these simulations can assess the influence of environmental factors such as temperature and irradiance on solar cell performance and evaluate the long-term durability and reliability of solar cell materials and structures [1].

In the first section of this chapter will begin by introducing the SILVACO/Atlas simulation software, which was utilized for simulating solar cells. We will provide an overview of its operational mode, as well as the different commands and instructions required for programming in SLVACO/Atlas. Additionally, we will discuss the various models that were employed during the simulation process. In the second section, we will present the results of numerical simulations carried out using SLVACO/Atlas software for single-junction CIGS solar cells, as well as for tandem structure combining CGS/CIGS absorber layers and triple-junction CGS/CIGS structure. We will present the findings of the numerical simulation of different structures and compare them with the experimental results. Additionally, we will offer our own interpretation of the results that have been obtained.

III.2. SILVACO/Atlas simulation tool

SILVACO/Atlas software is a simulation tool that is capable of predicting the electrical behavior of various semiconductor components under different operating conditions, including continuous, transient, and frequency regimes. In addition to simulating external electrical behavior, it can also provide details about the distribution of internal variables such as current

lines, electric field and potential. This is achieved by using numerical methods to solve the Poisson equation and the Continuity equations for electrons and holes in two dimensions.

ATLAS creates three different sorts of output files. The first type of output file is the run-time output, the second type is the log file and the third type is the solution file, the last two files are processed by the "TonyPlot" visualization tool.

III.3. Programming logic and specific commands

There are five sets of statements that must be stated in the right order (see Fig. III.1) we will now present the order of the commands specific to the programming logic in this simulator.

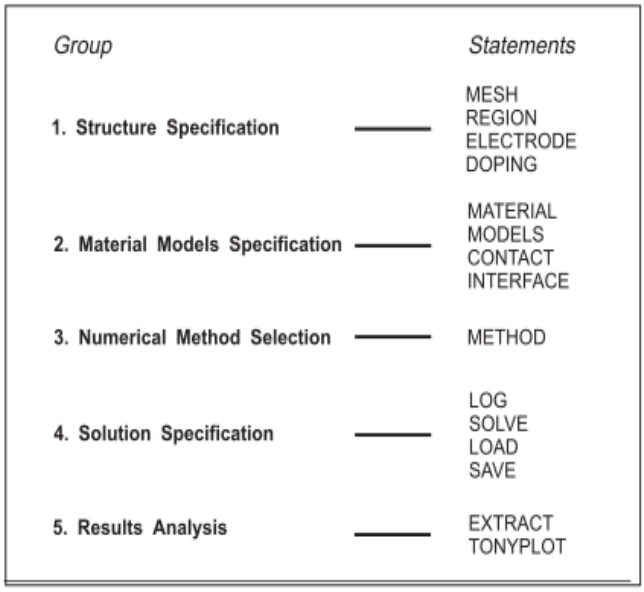

Fig. III.1: Primary statements for each group of ATLAS commands.

III.3.1. Structure specification

Structure specification is performed by defining the mesh, regions, electrodes and doping level. Atlas receives input files that contain simulation programs from DeckBuilt.

III.3.1.1. Mesh

The collections of both horizontal and vertical lines make up the mesh. The mesh in our study is two-dimensional, the mesh of our CIGS-based solar cell construction is displayed in Fig. III.2. The syntax for standard mesh specifications is [2]:

X.mesh location=<value> spacing=<value>
Y.mesh location=<value> spacing=<value>

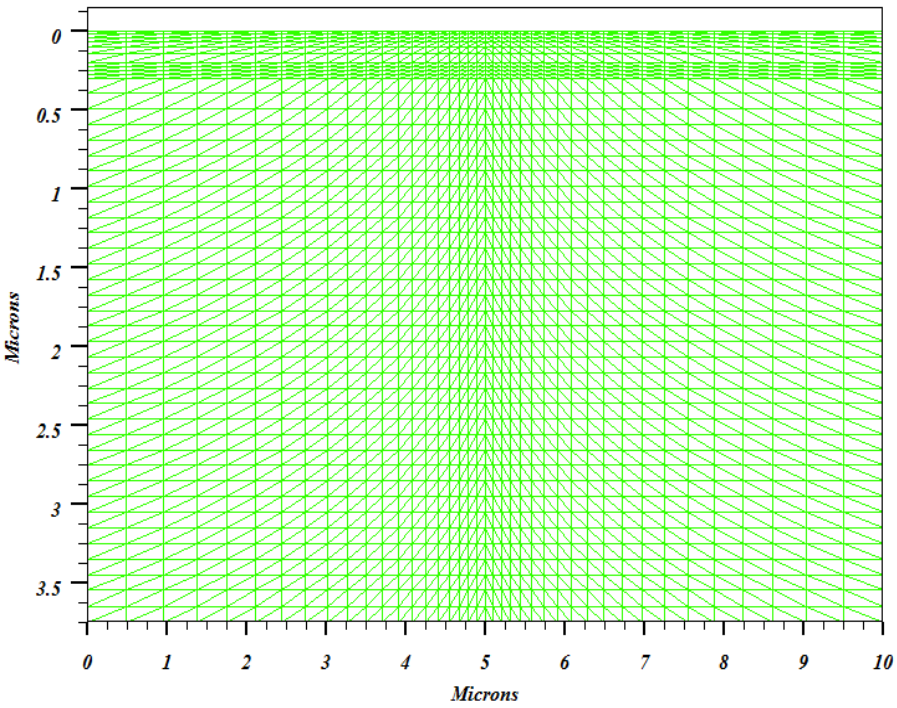


```
x.mesh loc=0      spac=0.5
x.mesh loc=5      spac=0.1
x.mesh loc=10     spac=0.5
y.mesh loc=0      spac=0.02
y.mesh loc=0.25   spac=0.02
y.mesh loc=0.3    spac=0.1
y.mesh loc=3.75   spac=0.1
```

Fig. III.2: Definition of Mesh in ATLAS.

The mesh is crucial to getting accurate simulation results. The mesh selection must be done in a way that strikes a balance between execution speed and outcome accuracy.

III.3.1.2. Region

The format for defining regions is as follows:

Region number=<integer> <material type> <position parameters>

The definition of materials for each layers of our CIGS solar cell structure is shown in Fig. III.3.

III.3.1.3. Electrode

The syntax for electrode definition is:

Electrode name=<electrode name> <position parameters>

X.min: Specifies the starting point of the electrode.

Right: The electrode is situated to the right of the structure (reverse: Left).

Top: The position of the electrode is at the top of the structure (reverse: Bottom).

III.3.1.4. Doping

Doping is the last component of the structural definition that needs to be clarified, and in Atlas, it is presented in the following formatted statement [2]:

Doping <distribution type> <doping type> <position parameters>

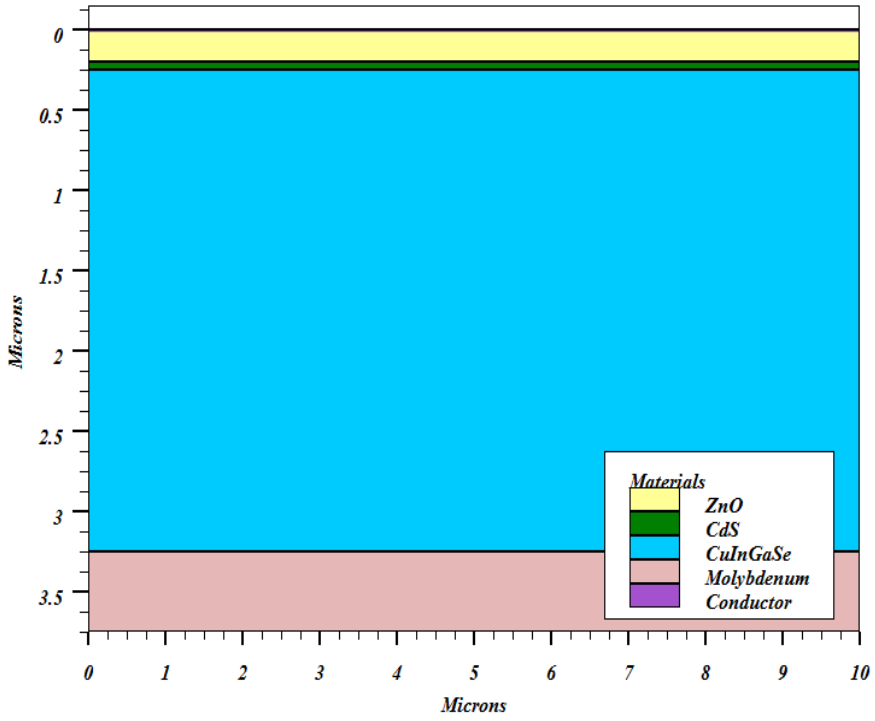

Fig. III.3: Definition of solar cell regions.

III.3.2. Material and model specifications

The next stage after specifying the structure is to specify the material models, which are broken down into four categories: material, models, contact, and interface.

III.3.2.1. Specifying material

The Atlas instruction that defines the material is given by:

Material <localization> < material-definition>

The material declaration can include additional parameters, including: the mobility of electrons (MUN) and the mobility of holes (MUP), (TAUN0) and (TAUP0) which are the lifetimes of electrons and holes respectively, the declaration of our material (CIGS) are as follows:

Material region=3 EG300 = 1.16 Permittivity = 13.6 Affinity = 4.8 MUN = 100 MUP = 25 Nc300 = 2.2e18 Nv300 = 1.8e19 Taup0 = 1e-7 Taun0 = 1e-7.

III.3.2.2. Physical model specifications

Mathematical expressions relating carrier density and electrostatic potential have been used to model physical patterns in semiconductors. Following is the syntax for the model specification:

Models <model flag> <general parameter> <model dependent parameters>

The following example enables multiple models:

```
Models  Conmob  Fldmob  SRH
```

III.3.2.3. Beam

The declaration of Beam command in our simulation program is as follows:

```
Beam num=1 X.origin=5 Y.origin=-1 angle=90 power.file=solarex10.spec
verbose  reflects=1 front.refl back.refl quantum.eff=1.
```

III.3.2.4. Contact

An illustration of Contact command from our program is as follows:

```
Contact name = anode   Surf.Rec VSurfN=1e5 VSurfP=1e5
Contact name = cathode Surf.Rec VSurfN=1e5 VSurfP=1e5
```

III.3.2.5. Interface

The interface charge density and surface recombination velocity at interfaces between semiconductors and insulators are defined by the Interface statement, the following example defines the interface with surface recombination for the electrons and the holes

```
Interface X.min=-4  X.max=4  Y.min=-0.5  Y.max=4  S.n=1E4  S.p=1E4
```

III.3.3. Numerical solution techniques

The problems in the semiconductor device can be solved numerically using a variety of techniques. The solution approach is specified in the manner shown below:

```
Method      Newton    Gummel    Block
```

The Gummel method will iteratively solve for each unknown while maintaining the other variables at their original values, continuing until a stable solution is reached. The Newton technique resolves the entire system of unknowns collectively. The third strategy (Block), which combines the preceding two methods, is beneficial for systems of mixed equations.

III.3.4. Solution specification

The solution specification statements are: Log, Solve, Load and Save.

III.3.4.1. Log and Solve

Log instructions allow the save all terminal characteristics in a data file, and the Solve statement follows the Log statement. It solves for one or more polarization points.

III.3.4.2. Load and Save

The Load instruction introduces, from an existing file, for each polarization point the previous solutions as an initial proposal. The Save instruction saves all information obtained for a node to an output file.

III.3.5. Extraction of results

The Tonyplot command is used to display the structure. This command will show the file "CIGS.str" as follows:

Tonyplot CIGS.str

In the next example, the extract instruction is used to obtain the current-voltage characteristic of a solar cell. This information is saved in the file "IV Characteristic CIGS single solar cell.log". So, TonyPlot draws the graph linking the information contained in this file. Fig. III.4 shows the result of a curve obtained by the TonyPlot instruction.

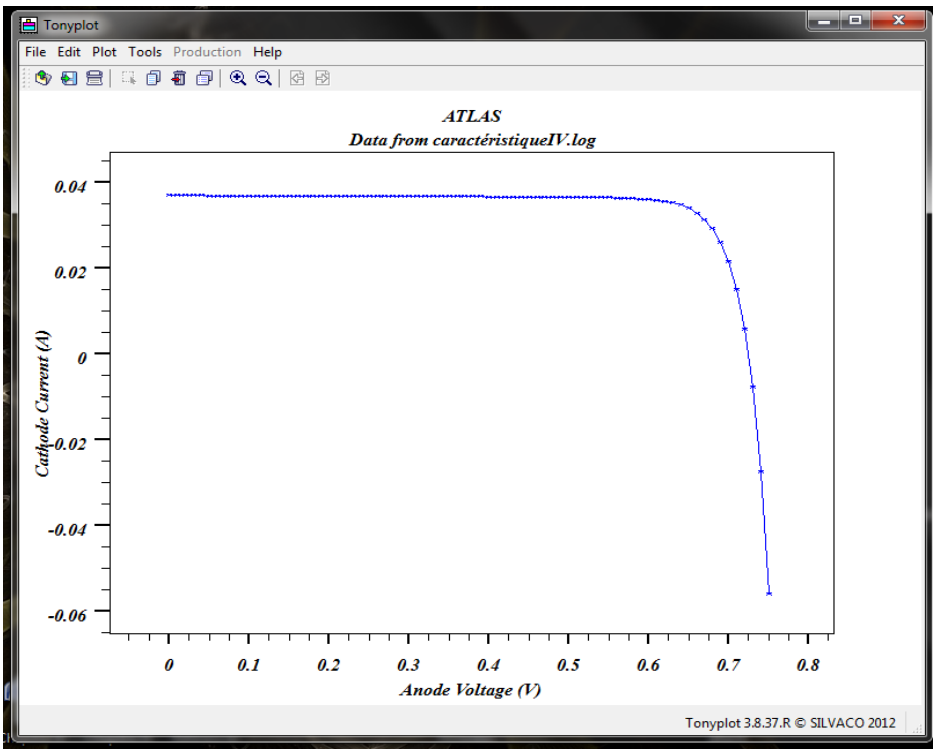

Fig. III.4: Extracting J-V characteristics of CIGS solar cell using Tonyplot.

III.4. Modeling of substrate CIGS solar cell

The conventional structure of CIGS solar cells consists of a glass substrate, a molybdenum back contact, a CIGS absorber layer, a buffer layer and a transparent front contact.

This structure is designed to optimize light absorption, charge transport, and collection in the CIGS layer.

The back-surface field (BSF) plays an important role in improving the device efficiency and reducing the thickness of the absorber layers [3-5]. The hydrogenated microcrystalline silicon (μc-Si:H) layer used as BSF can raise the conversion efficiency more than 4% compared to a solar cell without BSF layer [6].

In the conventional structure, the n-type CdS buffer layer is inserted between the ZnO window layer and p-type CIGS absorber layer to make a high-quality p-n junction in the interface [7]. In the proposed structure we have inserted a BSF layer based on μc-Si:H between the back-contact Molybdenum (Mo) layer and the CIGS absorber layer. The n-type CdS buffer layer was taken using 50 nm-thick and 2×10^{18} cm^{-3} donor density with a gap of 2.4 eV. The CIGS absorber layer is a p-type semiconductor with 3 μm-thick and 2×10^{16} cm^{-3} acceptor density [8] with a moderate gap Eg = 1.3 eV [9]. The degenerate ZnO(n+) window layer was taken as a wide band-gap Transparent Conducting Oxide (TCO) semiconductor (3.30 eV), with 100 nm-thick and 1×10^{19} cm^{-3} donor density [10]. In the proposed structure, a very thin Back Surface Field (BSF) μc-Si:H(p+) of 10 nm-thick, and heavily doped with 1×10^{21} cm^{-3}-hole density and band-gap of 1.45 eV [6]. A schematic view of the conventional CIGS solar cell structure and the proposed structure using BSF layer were displayed in Fig. III.5.

In this section, we will study the effect of CIGS layer thickness and doping concentration on the current density-voltage (J-V) characteristics and quantum efficiency (QE) of the conventional cell ZnO/CdS/CIGS and the effect of defect density on the performance of substrate CIGS solar cell using μc-Si:H as a BSF layer.

III.4.1. Physical model and simulation parameters

As we mentioned above, the SILVACO/Atlas simulator allows the solution of a set of basic semiconductor equations consisting of the Poisson equation and the continuity and transport equations for electrons and holes [11], the Newton method was selected for solving the basic semiconductor equations in the software as a default method. The band-gap E_g of $CuIn_{1-x}Ga_xSe_2$ alloys was calculated using the following expression [12]:

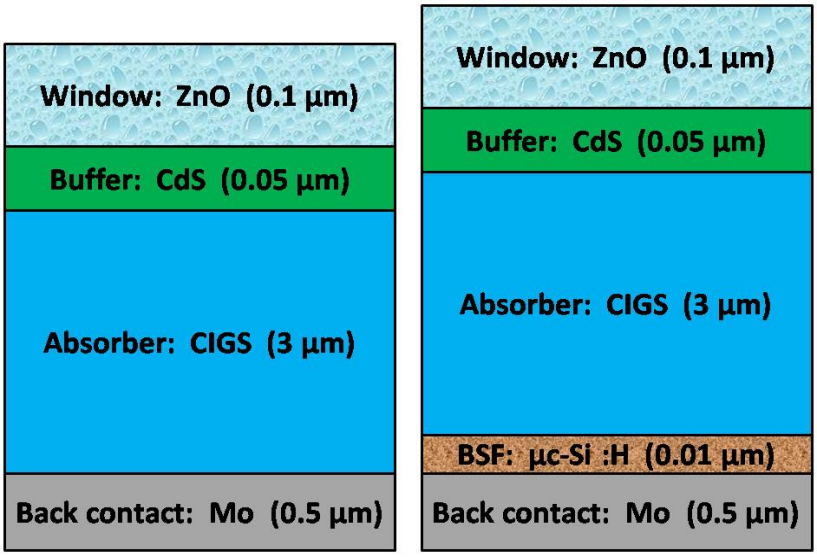

Fig. III.5: CIGS solar cell structures with and without µc-Si:H(p+) BSF layer.

$$E_g[eV] = 1.010 + 0.626.x - 0.167.x(1-x) \quad \text{(III.1)}$$

Where E_g ranges from 1.01 eV to 1.69 eV as x increases from 0 for CIS to 1 for CGS, respectively.

The input parameters of each layer of the proposed structure are summarized in Table III.1. These parameters are the thickness w, the permittivity constant εr, the band-gap E_g, the electron affinity χe, the electron/hole mobility μ_n/μ_p, the effective density of states in conduction/valence band N_C/N_V, and the donor/acceptor concentration N_D/N_A. At the front contact, the reflection was neglected. The values of the surface recombination velocity for holes/electrons S_n/S_p at front and back contacts were 1×10^7 cm/s.

Because all the layers are polycrystalline, they contain a wide range of defects [13]. Therefore, For CIGS and µc-Si:H layers, we used tow Gaussian deep donor defect distribution, and tow Gaussian deep acceptor defect distribution for ZnO and CdS layers. The donor and acceptor defect distributions are provided by ATLAS [11,12].

$$g_{GA}(E) = N_{GA} \exp\left[-\left[\frac{E_{GA}-E}{W_{GA}}\right]^2\right] \quad \text{(III.2)}$$

$$g_{GD}(E) = N_{GD} \exp\left[-\left[\frac{E-E_{GD}}{W_{GD}}\right]^2\right] \quad \text{(III.3)}$$

Where E is the defect energy, the subscripts (G, A, D) stand for Gaussian acceptor and donor defect states, respectively. The effective density of states (N_{GA} and N_{GD}), standard energy

deviation (W_{GA} and W_{GD}), and peak energy position all characterize the density of states (E_{GA} and E_{GD}).

Table III.1- Physical parameters and defect state of ZnO/CdS/CIGS/µc-Si :H(p+) structure used in the simulation.

Parameter	**ZnO(n)**	**CdS(n)**	**CIGS(p)**	**µc-Si :H(p+)**
Thickness *w* (µm)	0.1	0.05 [14]	3*	0.01 [6]
Band gap energy Eg (eV)	3.3 [16]	2.4 [12]	1.3 [9]	1.45 [6]
Doping density N_D/N_A (cm^{-3})	1×10^{19}	2×10^{18}[9]	2×10^{16} *	1×10^{21}*
Electron affinity χe (eV)	4.6 [4]	4.2[4]	4.5 [15]	4 [6]
Relative permittivity ε_r ($F.cm^{-1}$)	9 [3]	10 [12]	13.6 [16]	11.9 [6]
Density of states at conduction band N_C (cm^{-3})	2.2×10^{18}[14]	2.2×10^{18}[12]	2.2×10^{18}[16]	10^{19} [6]
Density of states at valence band N_V (cm^{-3})	1.8×10^{19}[14]	1.8×10^{19}[14]	1.8×10^{19}[16]	10^{19} [6]
Electron mobility µn (cm^2/Vs)	100 [12]	100 [15]	100 [12]	50 [6]
Hole mobility µp (cm^2/Vs)	25 [9]	25[3]	25 [4]	5 [6]
Gaussian defect density N_{GA}, N_{GD} (cm^{-3})	10^{14} (A) [15]	10^{14} (A) [15]	10^{14} (D)*	10^{14} (D)
Defect energy position E_{GA}, E_{GD} (eV)	mid-gap▪[12]	mid-gap▪[12]	mid-gap▪[12]	mid-gap▪
Standard energy deviation W_{GA}, W_{GD} (eV)	0.1(A) [14]	0.1(A) [12]	0.1(D) [12]	0.1(D)
Electron capture cross section σ_n (cm^2)	10^{-12} [9]	10^{-17} [9]	10^{-13} [9]	10^{-12}
Hole capture cross section σ_p (cm^2)	10^{-15} [9]	10^{-12} [9]	10^{-15} [9]	10^{-14}
Surface recombination velocity for electrons S_n and holes S_p ($cm.s^{-1}$)				
at front contact		10^7 [14]	10^7 [14]	
at CdS/CIGS interface		10^5 [12]	10^5 [12]	
at back contact		10^7 [14]	10^7 [14]	

▪ mid-gap is the middle of the band gap **(A) denote Acceptor defects**
*** A variable field** **(D) denote Donor defects**

The optical parameters of the real and imaginary parts of the wavelength-dependent refractive index n(λ) and extinction coefficient k(λ) for the CGS and CIGS materials are obtained from Paulson et *al.* (2003) [6]. For CdS and ZnO materials from Palik et *al.* (1998) [7] and from Richter et *al.* (2013) [8]. For the metal contact material Mo, optical constants available in the Sopra database of the SILVACO/Atlas simulator were used in the present simulation. In this study, the solar cells operating temperature was set as 300 K.

III.4.2. Band diagram

Understanding the behavior and dependability of any semiconductor device depends on the band diagram derived from such a configuration [17]. The band diagram of the simulated structure in this investigation was produced using Tonyplot from SILVACO/Atlas. The

obtained band diagram is displayed in Fig. III.6. A good band alignment was obtained between CIGS absorber layer and the μc-Si:H back surface field. After introducing a thin μc-Si:H BSF layer, an upward facing slope is created towards the surface so that the electrons are repelled from going near the surface as seen in Fig. III.6. The created back-side built-in electric field opposes minority carrier travel to the back surface, which has a high recombination velocity; hence electrons are reflected away from the back surface, minimizing rear surface recombination.

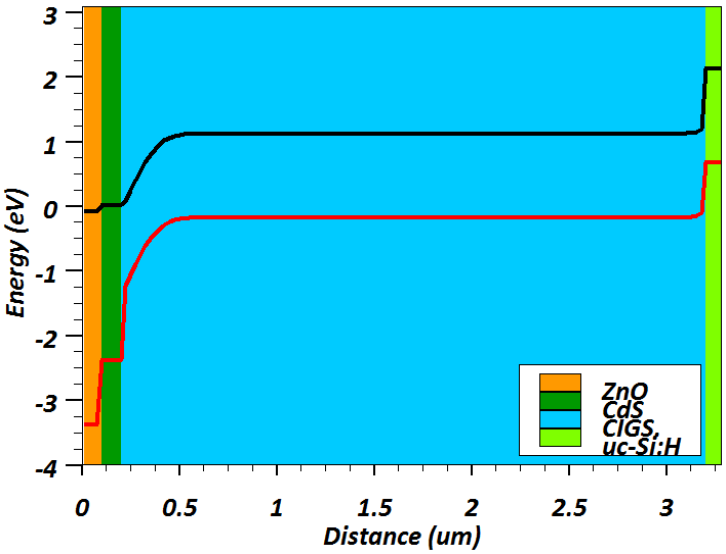

Fig. III.6: Band diagram of ZnO/CdS/CIGS solar cell with μc-Si:H BSF layer.

III.4.3. Thickness optimization of CIGS absorber layer

In this part, we'll look at the performance of the ZnO/CdS/CIGS solar cell using the material parameters listed in Table III.1. Fig. III.7 shows the evolution patterns of V_{oc}, J_{sc}, *FF* and η of ZnO/CdS/CIGS solar cell as a function of p-CIGS absorber layer thickness. When the CIGS layer thickness *w*(CIGS) is increased from 0.5 to 5 μm, J_{sc} rise significantly from 24 mA/cm^2 to approximately 33.95 mA/cm^2 and η increases rapidly from 14.37% to about 23.39% (by 40.17%), respectively. V_{oc} reches 0.84 V and *FF* reaches 83%. All photovoltaic properties are nearly identical for a thick p-CIGS absorber layer (more than 5 μm). This overall behavior is resulted from the increase of the photons absorption and even the increase of the electron-hole generation in the p-CIGS absorber layer. Therefore, the thickness of 5 μm is chosen as an optimum thickness for p-CIGS absorber layer for an efficient ZnO/CdS/CIGS solar cell [9]. If the absorber layer thickness is reduced the back contact will be very close to the depletion region [18]. Additionally, for comparison, similar behaviors of the performance parameters were achieved by Benmir et *al.* [19] and Heriche et *al.* [20].

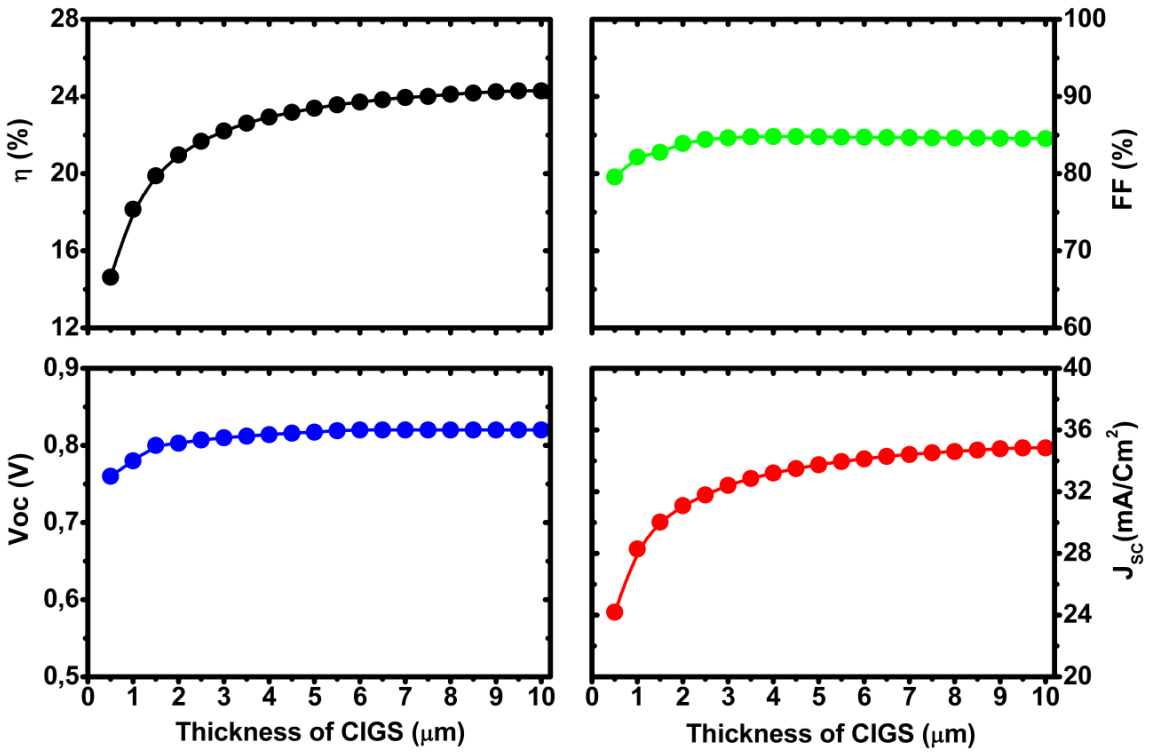

Fig. III.7: Cell performance as a function of CIGS absorber layer thickness.

III.4.4. Optimization of acceptor density N_A(CIGS)

The acceptor concentration of p-CIGS absorber layer has been discovered to be significant factors that have a direct impact on the performance of CIGS based solar cells. As a result, the absorber layer's acceptor concentration, N_A(CIGS), is adjusted from 10^{12} cm^{-3} to 10^{18} cm^{-3}, and the simulated photovoltaic characteristics are displayed in Fig. III.8. The J_{sc} exhibits a very modest drop from 34.08 mA/cm^2 for a concentration of 10^{14} cm^{-3} to an acceptable limit of 31.55 mA/cm^2 for a concentration of 4×10^{17} cm^{-3}, which is caused by an increase in free carrier charge recombination that occurs inside the bulk [21]. On the other hand, V_{oc}, *FF* and efficiency are increased significantly with the increase of N_A(CIGS) from 10^{12} cm^{-3} to 10^{17} cm^{-3} whereas the optimum efficiency achieved is 22.49% in the acceptor concentration of about 10^{17} cm^{-3}, the $V_{oc} \approx 0.83$ V and $FF \approx 84.37\%$. After this value the structure presents a strong decrease in the V_{oc}, *FF* and efficiency. The result indicates that the N_A(CIGS) must be higher than 10^{16} cm^{-3} and lower than 2×10^{17} cm^{-3} to obtain a good performance.

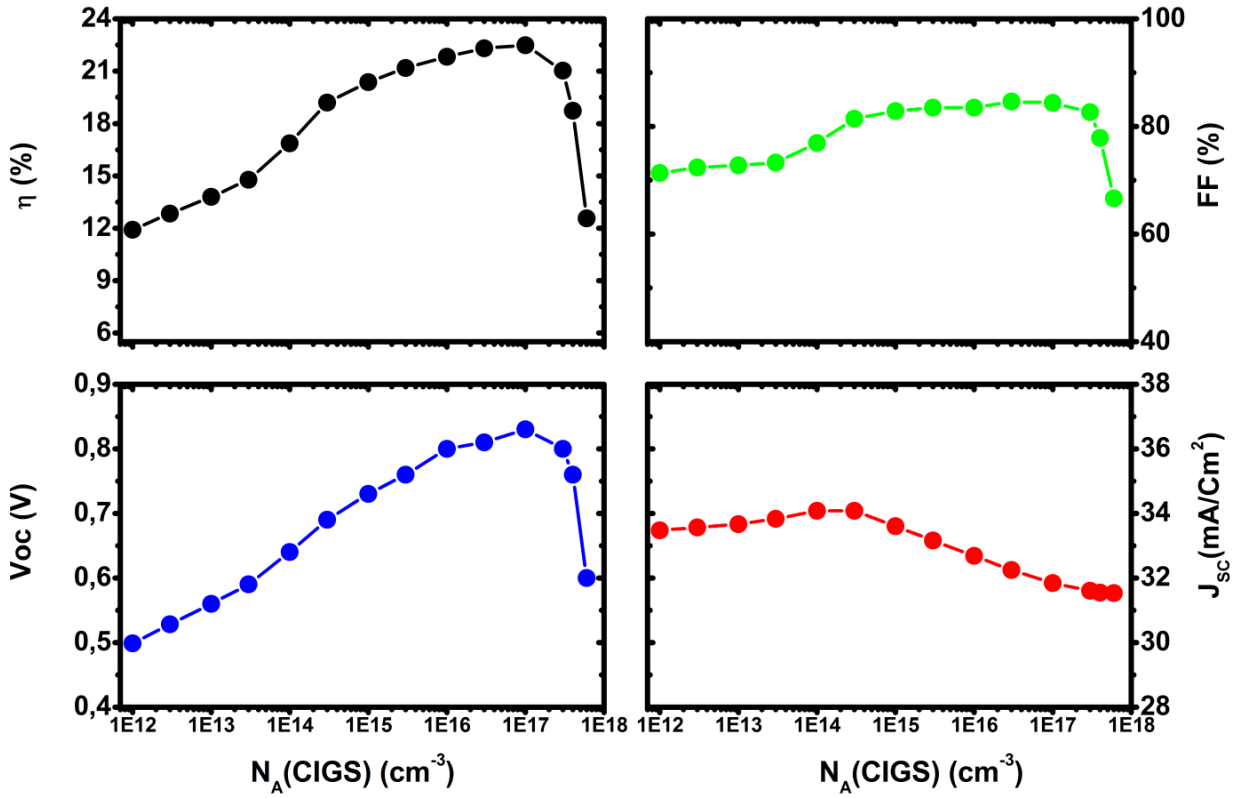

Fig. III.8: Effect of acceptor concentration of absorber layer N_A(CIGS) on cell performances.

III.4.5. Influence of defect state density of CIGS absorber layer N_G(CIGS)

The conversion efficiency of CIGS solar cells is drastically influenced by defects caused by increasing of Ga content. The simulation results of CIGS solar cell with various Gaussian defect state densities positioned in CIGS band-gap, N_G(CIGS), are presented in Fig. III.9. When N_G(CIGS) > 10^{15} cm^{-3}, the result depicts a negative influence on the device's performance. All the photovoltaic parameters, including V_{oc}, J_{sc}, *FF*, and η, are reduced. The carriers are trapped or recombined in flaws, resulting a waste of energy that does not contribute to the transportation of the current to the external load. When N_G(CIGS) = 10^{14} cm^{-3}, a good performance was reached: J_{sc} = 32.41 mA/cm^2, V_{oc} = 0.81 V, *FF* = 84.65% and η = 22.21%. At a high defect concentration of around 3 × 10^{18} cm^{-3}, J_{sc} = 18.95 mA/cm^2, V_{oc} = 0.57 V, *FF* = 22.1% and η = 2.4% were obtained. As a result, the bulk defect density, which is connected to creating trapping (recombination state) in the CIGS absorber bulk, may have a significant impact on current transport [22].

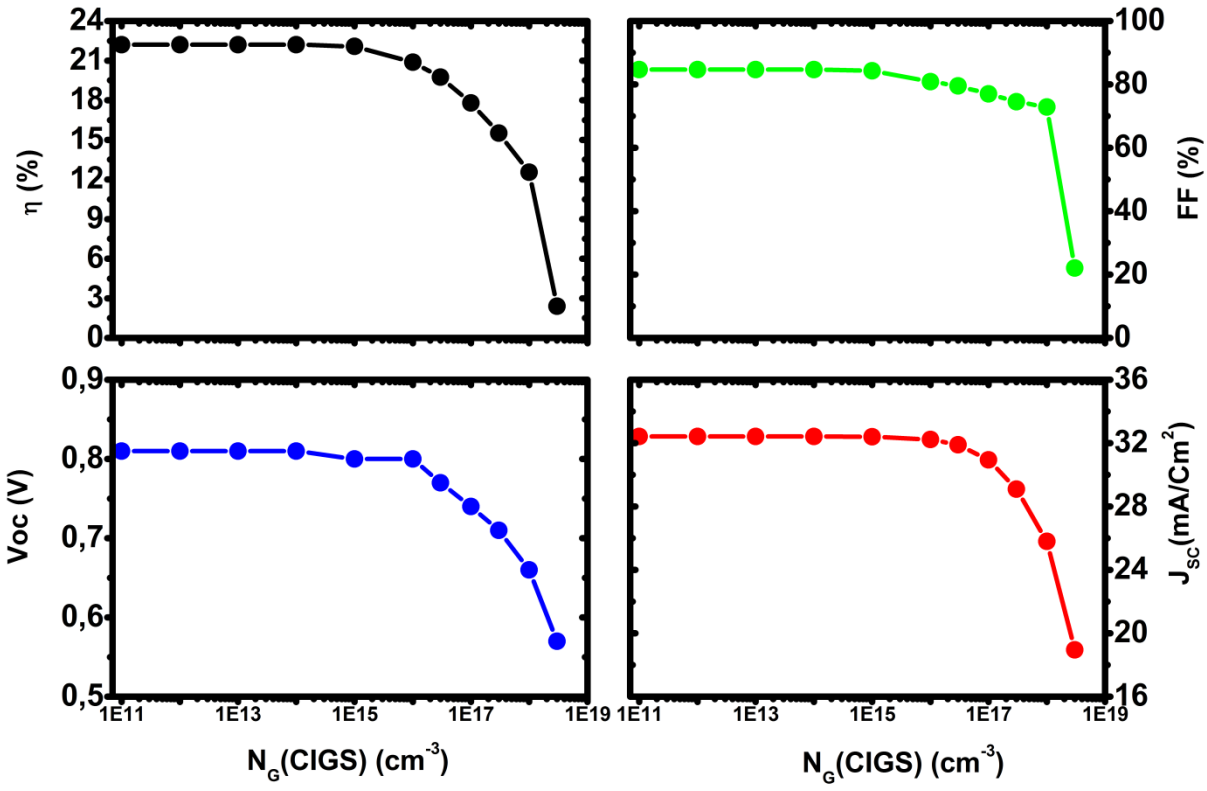

Fig. III.9: Photovoltaic parameters of CIGS solar cell as a function of Gaussian defects concentration, N_G(CIGS).

III.4.6. Effect of µc-Si:H BSF layer on CIGS solar cell performance

In Fig. III.10, the quantum efficiency (QE) of ZnO/CdS/CIGS/µc-Si:H(p+)/Mo solar cell structure, with various CIGS absorber layer thicknesses, is shown. We can see that QE increases as the CIGS layer thickness increases, this means that more photons are absorbed [23].

The simulation results for a conventional solar cell with and without µc-Si:H(p+) BSF layer are given in Fig. III.11 taking a thickness of 10 nm of µc-Si:H BSF layer. The optimum CIGS thickness observed was 5 µm, which corresponds to an efficiency of 23.39% of the conventional cell. By using BSF layer, a new optimum thickness obtained is 1.5 µm gives an efficiency of 23.42%. It is noteworthy that the solar cell efficiency has jumped from 18.6% to 22.08% for CIGS layer thickness of 0.5 µm and 1 µm, respectively. This is owing to the fact that the majority of electron/hole pairs are created when the absorber layer is bulky. Because the high cost of gallium and indium materials in CIGS solar cells [24,25], lowering the usage of indium and gallium materials by reducing the layer thickness is sufficient to minimize the cost of CIGS cell manufacture.

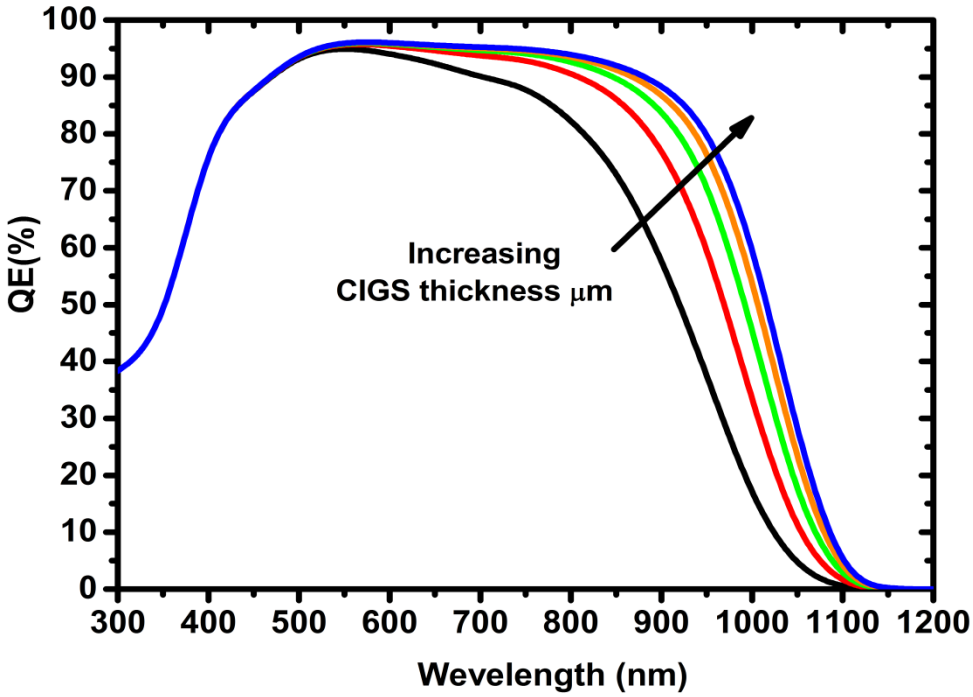

Fig. III.10: Quantum efficiency of CIGS solar cell with μc-Si:H BSF layer.

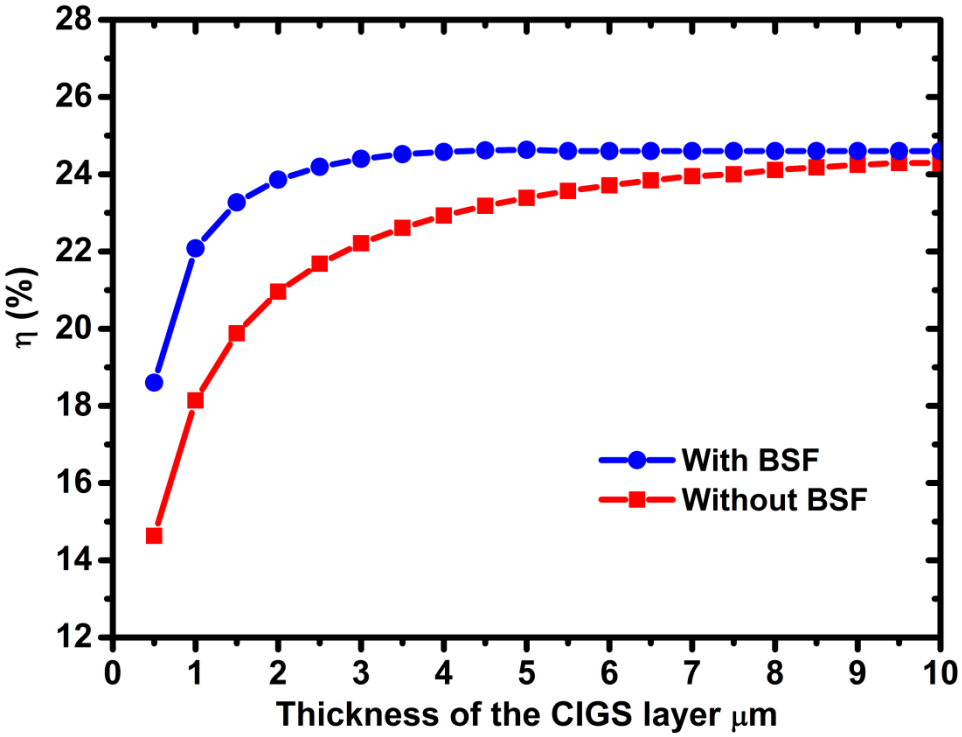

Fig. III.11: Performance evolution with variable CIGS thickness of conventional CIGS solar cell with and without BSF layer.

In Fig. III.12, the CIGS solar cell with BSF layer exhibited better J-V characteristics. Indeed, it is clear that the cell with BSF possesses better performances comparing to the basic

cell. In Table III.2, the obtained results are displayed. It is evident that all these parameters are improved by the insertion of BSF layer.

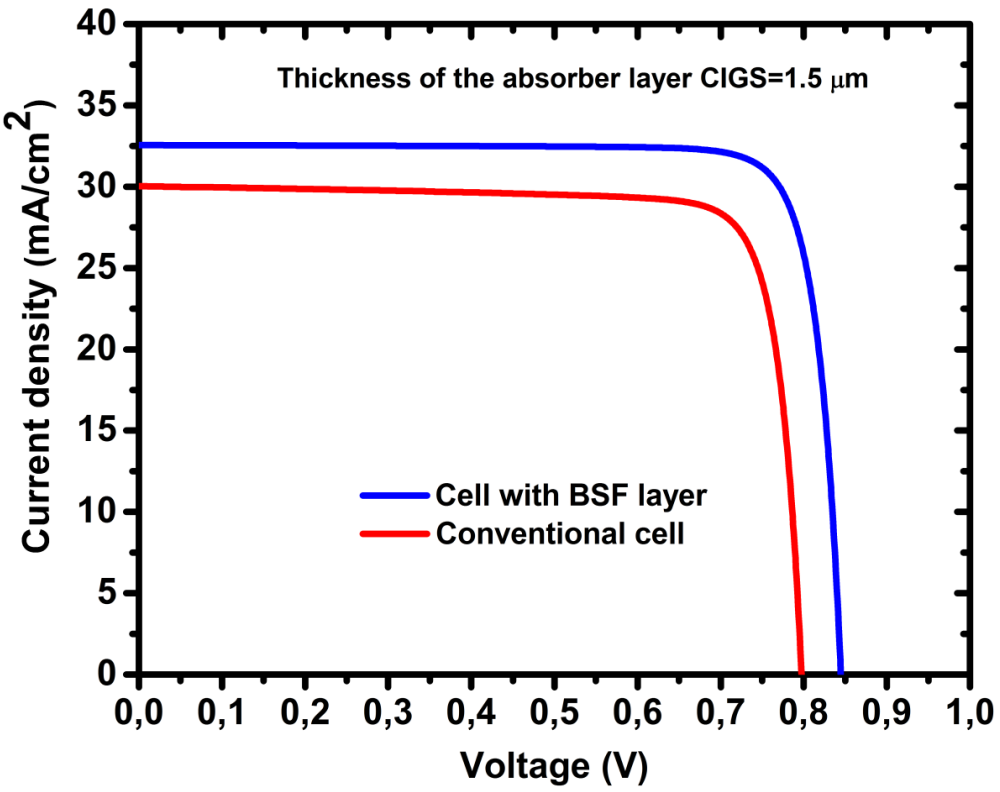

Fig. III.12: J-V characteristics for CIGS solar cell with and without BSF layer.

III.4.7. Influence of acceptor density of BSF layer on cell performance

The influence of BSF doping concentration on cell performance is given in Fig. III.13. The doping concentration of μc-Si:H BSF layer was varied from 10^{13} cm^{-3} to 10^{21} cm^{-3}. We noticed that the photovoltaic parameters such as the open-circuit voltage and efficiency increased significantly when the doping concentration of BSF layer increased. This is due to the electrical field distribution at the rear contact, which prevents minority carrier recombination [4]. The raising of BSF doping concentration from 10^{17} cm^{-3} to an acceptable limit has no significant effect on the short-circuit current and fill factor. The efficiency improvement is restricted between 23% and 24%. As a result, it can be stated that using a highly-doped BSF layer will be preferred.

Table III.2: Impact of CIGS absorber thickness with BSF layer on cell performance and comparison with some results reported in bibliography.

No	Type of research	CIGS (nm) thickness	Jsc (mA/cm^2)	Voc (V)	FF (%)	η (%)	Ref
1	Experimental	2500	38.50	0.74	79.70	22.92	[26]
2	Experimental	1000	35.71	0.69	78.12	19.20	[28]
3	Experimental	2200	35.50	0.69	81.20	19.90	[13]
4	Theoretical	2000	38.90	0.74	79.68	22.94	[9]
5	Theoretical	3000	33.50	0.78	82.00	21.32	[18]
6	Theoretical	1000	34.47	0.74	83.09	21.30	[15]
7	Theoretical	3500	44.39	0.65	77.49	22.69	[27]
8	Theoretical	1500	32.55	0.84	85.31	23.42	[•]

No	Type of research	Absorber Layer	BSF Layer	η without BSF (%)	η with BSF (%)	Enhancement in η (%)	Ref
1	Experimental	Si	ZnS	6.40	11.02	72.19	[29]
2	Experimental	CIGS	$MoSe_2$	9.00	14.00	55.55	[30]
3	Theoretical	CdTe	SnS	17.40	21.83	25.45	[3]
4	Theoretical	CIGS	Si	16.39	21.30	29.96	[15]
5	Theoretical	CIGS	µc-Si: H	19.80	23.42	18.28	[•]

[•] **Our Work**

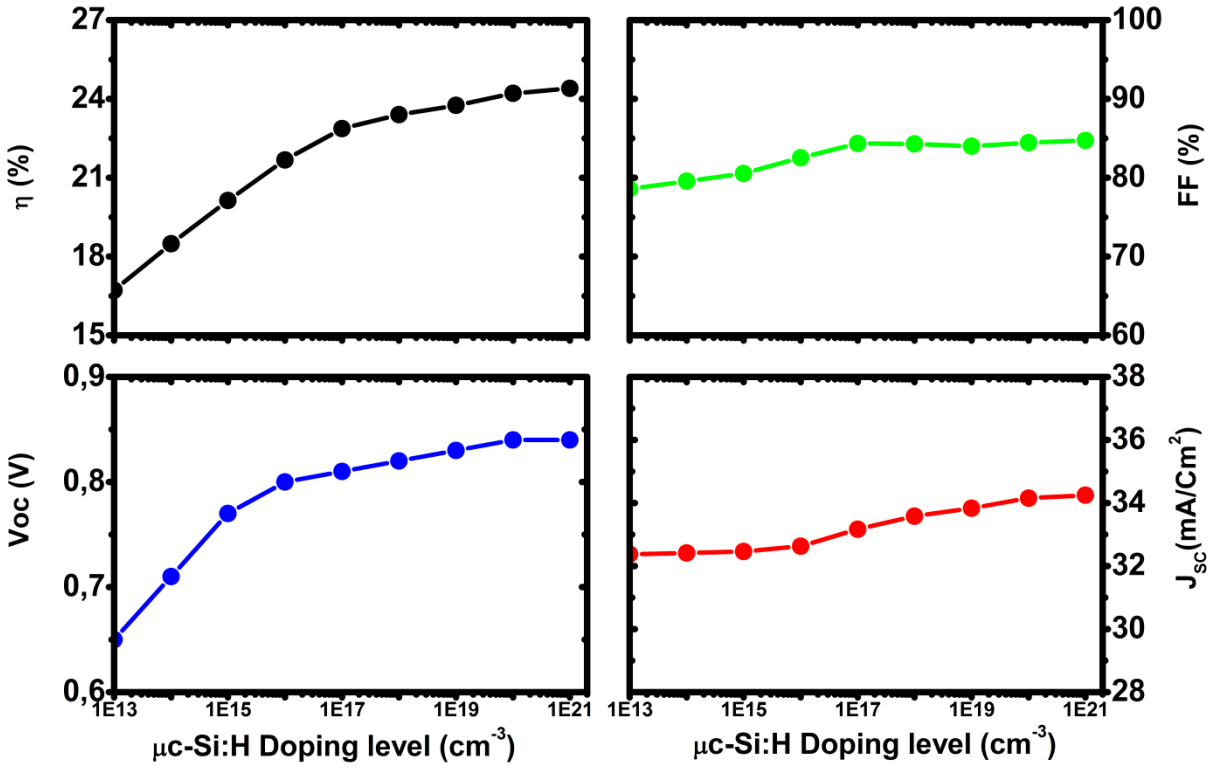

Fig. III.13: Output characteristics of CIGS solar cells versus BSF doping level.

III.4.8. Effect of operating temperature on efficiency using BSF layer

As illustrated in Fig. III.14, lowering the temperature has a favorable and significant impact on the cell performance metrics. The efficiency gain is around 0.28%, at a temperature of 300 K. As a result, 300 degrees Fahrenheit is the ideal temperature. Similar behaviors of performance parameters were reported in Ref. [31] where the temperature is a fundamental determinant of CIGS solar cell performance and a drop in temperature boosts cell efficiency greatly. Lowering the cell temperature to 300 K is preferable and installing the cell in low-temperature areas or employing PV panel cooling methods is two ways to lower the cell temperature.

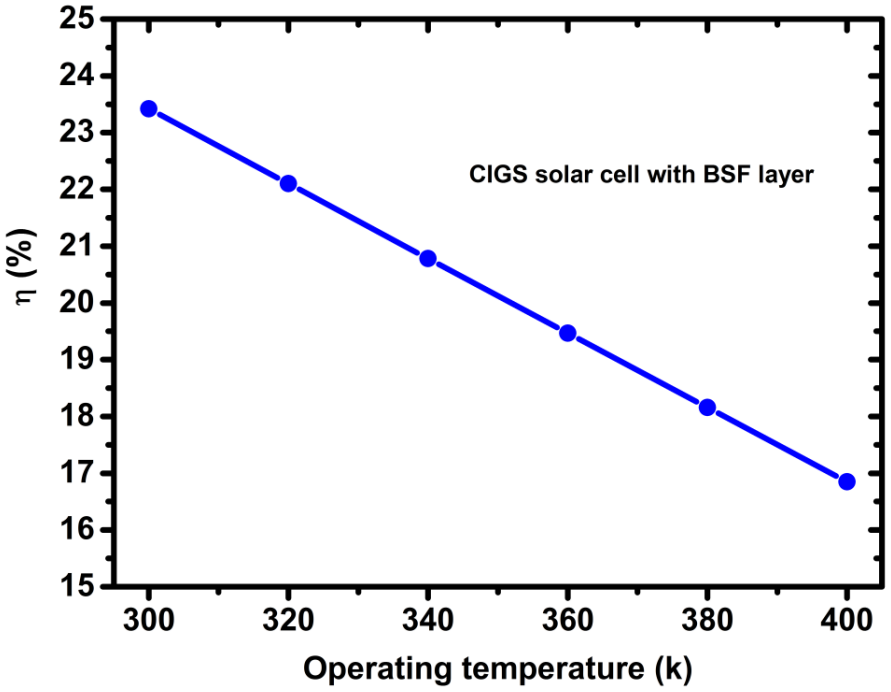

Fig. III.14: Efficiency variation for CIGS solar cell with BSF layer as a function of operating temperature.

III.5. Tandem solar cell modeling

To enhance light absorption and achieve high conversion efficiency, a variety of absorbers with various energy band gaps should be used. Fig. III.15 depicts the CGS/CIGS tandem solar cells structural layout.

The structure composed two solar cells: The top-cell with a small adjustable band-gap (E_G = 1.69 eV) and the bottom-cell with a regular 5 µm band-gap (E_G = 1.16 eV) [32]. The goal of this design is to maximize the output power while converting a broad range of incident photons on the solar cell. The top-cell n-CdS/p-CGS heterojunction and the bottom-cell n-

CdS/p-CIGS heterojunction of this tandem cell are joined optically and electrically by ZnO layer acting as a transparent conducting oxide (TCO). The tandem cell was assumed to be lit up under AM1.5 G solar spectrum conditions with an incident power density of 100 mW/cm^2. ZnO layer, which stands in for the front cathode contact for the molybdenum (Mo) layer that serves as the back-anode contact, was assumed to receive solar radiation normally. Fig. III.15 shows all layers' name indicating the thickness and doping concentrations that were employed in the simulation.

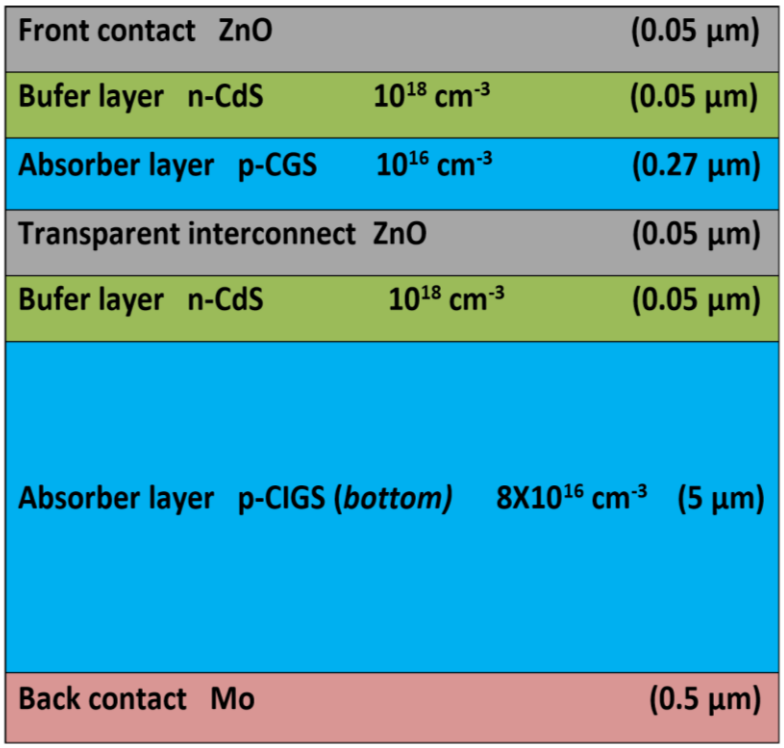

Fig. III.15: Design of the simulated tandem solar cell with CGS/CIGS sub-cells connected by an interconnect formed by conducting transparent ZnO layer.

III.5.1. Physical model of CGS/CIGS tandem solar cell

The input data of each layer used by SILVACO/Atlas is given in Table III.3. The band gap value of $CuIn_{1-x}Ga_xSe_2$ absorber was estimated using an empirical expression in equation (III.1). For the top and bottom cells, the value of x is taken as 1 and 0.31, respectively.

Gaussian distribution was used to model the defect density within the CIGS and CdS layers as mentioned in equations (III.2) and (III.3). The Shockley-Read-Hall recombination relation was used to access the Gaussian defect distribution in semiconducting layers of solar cells:

$$R_{SRH} = \frac{pn - n_i^2}{\tau_p\left(n + n_i exp^{\frac{E_i - E_T}{kT_L}}\right) + \tau_n\left(p + n_i exp^{\frac{-(E_i - E_T)}{kT_L}}\right)} \quad \text{(III.4)}$$

$$\tau_n = \frac{1}{\sigma_n v_{th} N_t} \quad \text{and} \quad \tau_p = \frac{1}{\sigma_p v_{th} N_t} \quad \text{(III.5)}$$

Table III.3: Material parameters used in the simulation.

Parameter	**CdS(n)**	**CGS/CIGS**	
Band gap energy *Eg* (eV)	2.4 [12]	1.69/1.16 [12]	
Electron affinity χe (eV)	4.2 [4]	4.5 [15]	
Relative permittivity ε_r (F.cm^{-1})	10 [12]	13.6 [16]	
Density of states at conduction band N_C (cm^{-3})	2.2×10^{18} [12]	2.2×10^{18}[16]	
Density of states at valence band N_V (cm^{-3})	1.8×10^{19} [14]	1.8×10^{19}[16]	
Electron mobility μn (cm^2/Vs)	100 [15]	100 [12]	
Hole mobility μp (cm^2/Vs)	25 [3]	25 [4]	
Gaussian defect states	**CdS**	**CGS/CIGS**	
Gaussian defect density N_{GA} , N_{GD} (cm^{-3})	10^{15} (A)	10^{15} (D)	
Peak energy position E_{GA} , E_{GD} (eV)	1.2 (A) [12]	0.84/0.58 (D) [12]	
Standard energy deviation W_{GA} , W_{GD} (eV)	0.1 (A) [12]	0.1 (D) [12]	
Electron capture cross section σ_n (cm^2)	10^{-17} [9]	$2*10^{-13}$ [9]	
Hole capture cross section σ_p (cm^2)	10^{-12} [9]	$3*10^{-15}$ [9]	
Surface recombination velocity for electrons and holes (cm.s^{-1})		***S$_n$***	***S$_p$***
CdS/CGS interface		10^5[12]	10^5[12]
CdS/CIGS interface		10^5[12]	10^5[12]
Front contact		10^7[14]	10^7[14]
Back contact		10^7[14]	10^7[14]

Where τ_n and τ_p represent the lifetime parameter for electrons and holes, respectively, σ_n and σ_p represent the capture cross-section, v_{th} represents the thermal velocity, N_t represents the bulk trap density, n_i represent the spatially changing level of intrinsic concentration, E_i represents the Fermi level, E_T represents the trap energy level and T_L represents the temperature [33].

It is obvious that there would be a high defect concentration at the interfaces due to lattice mismatching [34] and the surface recombination can be expressed as:

$$R_{Surf} = \frac{pn - n_i^2}{\tau_p^{eff}\left(n + n_i exp^{\frac{E_i - E_T}{kT_L}}\right) + \tau_n^{eff}\left(p + n_i exp^{\frac{-(E_i - E_T)}{kT_L}}\right)} \quad \text{(III.6)}$$

$$\frac{1}{\tau_n^{eff}} = \frac{1}{\tau_n^i} + \frac{d_i}{A_i} S.N \quad \text{and} \quad \frac{1}{\tau_p^{eff}} = \frac{1}{\tau_p^i} + \frac{d_i}{A_i} S.P \quad \text{(III.7)}$$

Where τ_n^i and τ_p^i are the bulk lifetime calculated at node i along the interface and which may be a function of the impurity concentration as well. i Parameter is the length and area of the interface. The S.N and S.P Parameters are the recombination velocities for electrons and holes, respectively [35].

The optical parameters like refractive index and extinction coefficient were taken from the literature [36-38] and used to study the characteristics of triple-junction solar cells. The optical parameters for metal contacts are obtained from the Sopra database. The overall simulations for the proposed configuration are carried out at 300 K.

III.5.2. Photovoltaic parameters for CGS top-cell, CIGS bottom-cell and CGS/CIGS tandem solar cells

The CIGS bottom-cell is presented in Fig. III.16 as comprising of p-type CIGS absorber layer and n-type CdS buffer layer. The cell is topped with a ZnO window layer as transparent conducting oxide, while Mo back contact is used for back metallization to establish electrical contacts. The band-gap energy of p-CIGS absorber layer is approximately 1.16 eV, which corresponds to *x* of about 0.31. In a good study by Jackson et *al.* [32], CIGS solar cells were manufactured by adjusting the composition *x* from 0.30 to 0.35, which resulted a maximum efficiency of 20.3%. Fig. III.16 illustrates the structure of single CIGS solar cell and some information such as doping concentrations and thickness of CdS and CIGS layers.

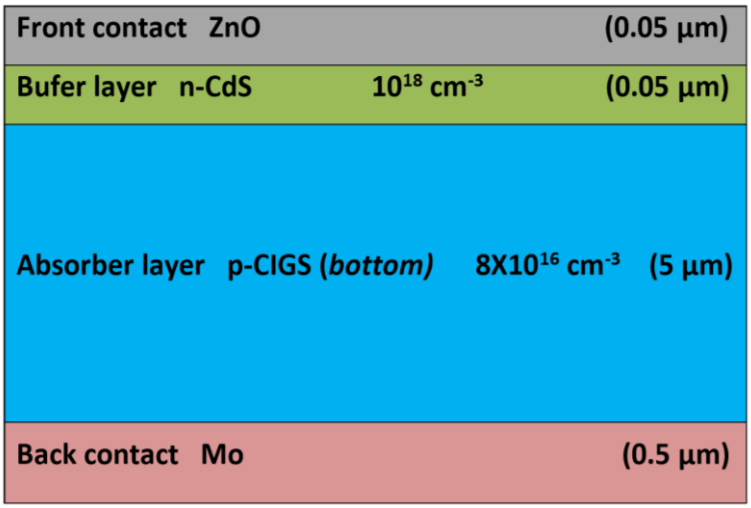

Fig. III.16: Single CIGS solar cell structure.

Fig. III.17 displays the structure of single CGS solar cell, where the Ga composition was *x* = 1, corresponds to energy band-gap of 1.69 eV. To enhance the conversion efficiency of the CGS solar cell, the doping concentrations of CdS and CGS were optimized.

Fig. III.18 illustrates the J-V characteristics for the individual CIGS and CGS solar cells. Table III.4 includes the photovoltaic parameters obtained of single CIGS bottom-cell, which were extracted from its corresponding J-V characteristic and compared with other simulation and experimental works.

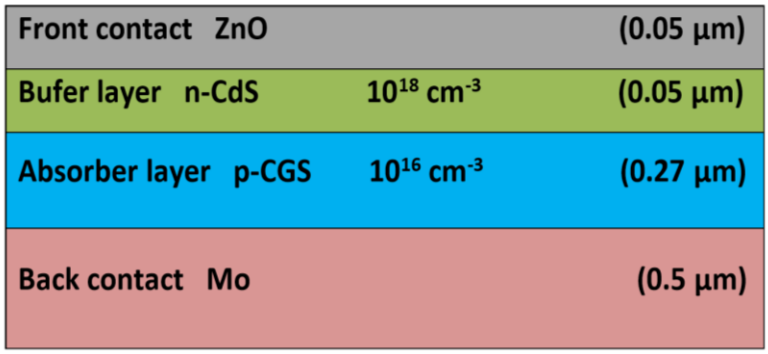

Fig. III.17: Single CGS solar cell structure.

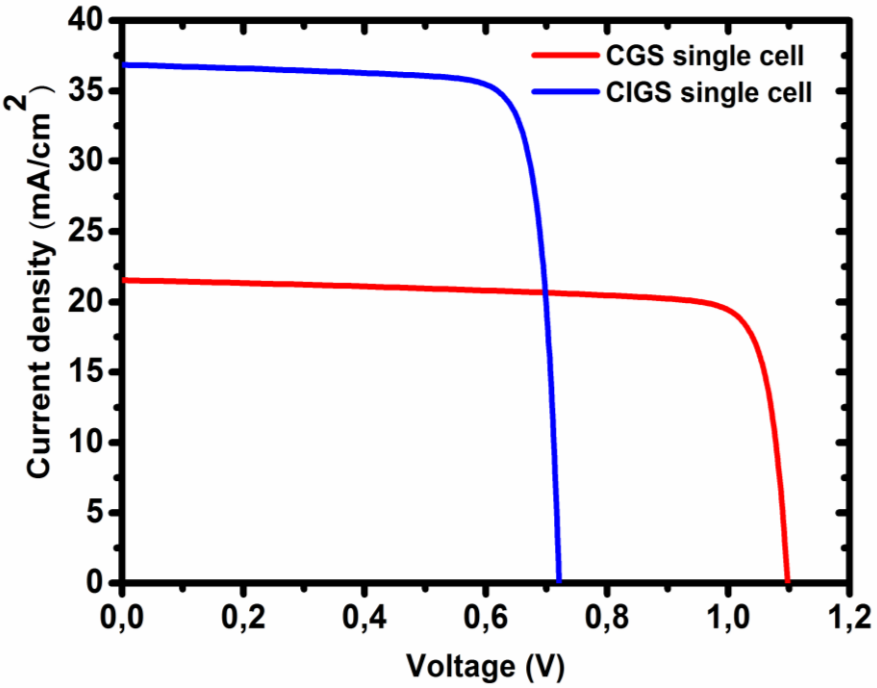

Fig. III.18: J-V characteristics of both single CIGS and CGS solar cells.

Table III.5 summarizes the photovoltaic parameters of single CGS solar cells extracted from the corresponding J-V characteristic. We notice that the simulation results for V_{oc} and *FF* are reasonable, while the J_{sc} is comparatively low, resulting a lower η of about 19.58%.

Table III.4: Results obtained from single CIGS solar cell were compared to simulations and experimental data from other studies.

No	Type of research	Jsc (mA/cm^2)	Voc (V)	FF (%)	η (%)	Ref
1	Experimental	35.40	0.74	77.50	20.30	[32]
2	Experimental	35.71	0.69	78.12	19.20	[28]
3	Experimental	35.50	0.69	81.20	19.90	[13]
5	Theoretical	33.50	0.78	82.00	21.32	[18]
6	Theoretical	34.47	0.74	83.09	21.30	[20]
7	Theoretical	34.86	0.67	79.88	18.50	[31]
8	Theoretical	36.84	0.72	82.66	22.01	[*]

[*] **Our Work**

Fig. III.19 displays the combined J-V characteristics of CGS top-cell, the CIGS bottom-cell and CGS/CIGS tandem solar cell. The photovoltaic parameters obtained from these characteristics are listed in Table III.5. To calculate J-V curves of the top and the bottom solar cells, the anode and the cathode of CGS top-cell were placed on the interconnect ZnO layer and the ZnO front layer. Similarly, for the bottom-cell, the anode and the cathode contacts were positioned on the back Mo layer and the interconnect ZnO layer.

Table III.5: Photovoltaic parameters of CIGS bottom-cell, CGS top-cell and CGS/CIGS tandem solar cell.

	Jsc (mA/cm^2)	Voc (V)	FF (%)	η (%)
CGS single cell	21.53	1,08	82.61	19.58
CGS top-cell	20.77	1.08	82.72	18.75
CIGS bottom-cell	16.48	0.72	82.50	09.92
CGS/CIGS tandem cell	16.53	1.81	85.93	25.85

The current density J_{sc} of CGS/CIGS tandem cell is constrained due to the low current of the CIGS bottom-cell. The J_{sc} value of tandem cell, which is 16.53 mA/cm^2, is approximately equivalent to the J_{sc} value of the bottom-cell, which is 16.48 mA/cm^2. However, the V_{oc} value of tandem cell, which is 1.81 eV, is approximately equal to the sum of the V_{oc} of the top-cell, which is 1.08 eV, and the V_{oc} of the bottom-cell, which is 0.72 eV. These results suggest that the series connection of CGS and CIGS cells in a tandem structure is functioning properly. Moreover, the tandem cell has a higher fill factor (85.93%) compared to the top-cell (82.72%) and bottom-cell (82.50%). The increase in *FF* and V_{oc} is responsible for the efficiency improvement to 25.85% compared to single CIGS cell (22.01%) and single CGS cell (19.58%).

Tandem solar cells using CGS and CIGS cells have been studied in only by few works. Jiyon et *al.* [39] conducted numerical studies on the performance of the CGS/CIGS tandem cell with a double band-gap graded ClGS bottom-cell at different CGS absorber thicknesses, using AMPS-1D software. According to the simulation outcomes in our work, the optimized CGS and CICS cell structure could give potentially efficiency of about 25% of CCS/CIGS tandem cell. As a comparison, the unoptimized GGS/CIGS tandem solar cell simulated in our work give at least 25.11% higher than the efficiency reported by Jiyon et *al.*, 2003 [39].

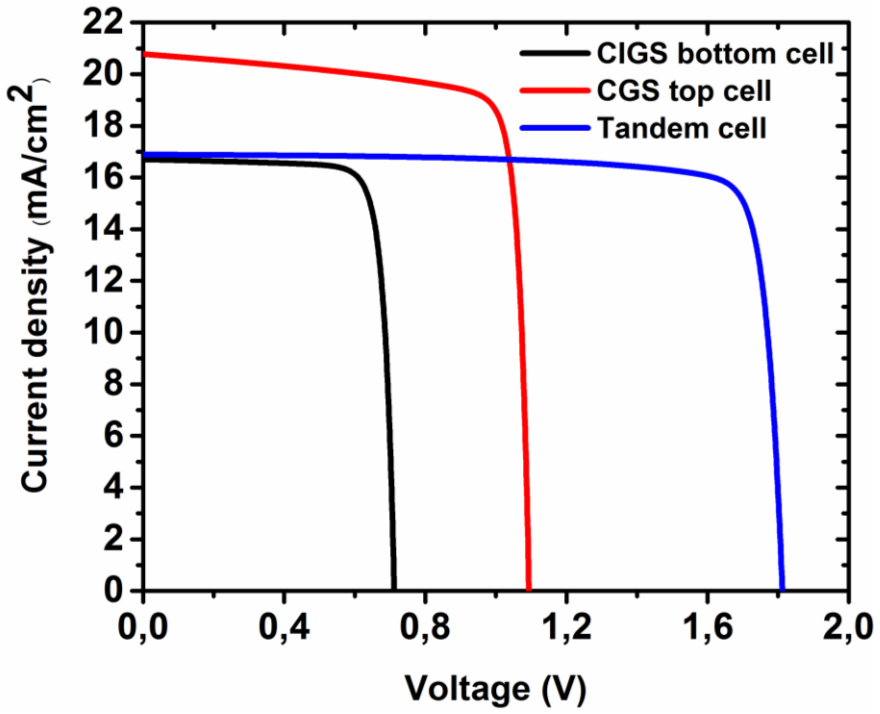

Fig. III.19: J-V characteristics of CIGS bottom-cell, CGS top-cell and CGS/CIGS tandem cell.

When we compare the outcomes of the CIGS single cell and the CIGS bottom-cell in the tandem cell (Fig III.19), we can notice a significant degradation in the photovoltaic parameters of the CIGS bottom-cell. This degradation can be attributed to the high absorption of the incident light by CGS top-cell. Due to a current mismatch between the top and bottom cells, the J_{sc} of CGS/CIGS tandem cell is limited by the low J_{sc} of both cells, resulting a relatively low efficiency of CGS/CIGS tandem cell.

III.5.3. Impact of CGS layer thickness on the CGS/CIGS tandem cell performance

When the CGS layer thickness of CGS top-cell is thinner, it allows more light to pass through the structure, resulting an increase of J_{sc} in CIGS bottom-cell and vice versa. In this

work, we experimented with varying the CGS layer thickness of top-cell from 0.14 µm to 0.29 µm, while keeping the CIGS layer thickness of bottom-cell unchanged (5 µm).

Fig. III.20 illustrates the relation between the CGS layer thickness and the short-circuit current densities of the top and the bottom cells. Both current densities exhibit a strong dependency on the CGS layer thickness. An increase of CGS layer thickness results an increase of current density in CGS top-cell, J_{sct}, and a decrease of J_{scb} of CIGS bottom cell, because a thick top-cell absorbs more light, reducing the amount transmitted to the bottom-cell. Conversely, a thin top-cell absorbs less light, allowing more light to pass through to the bottom-cell. As the CGS layer thickness increases, the J_{sct} and J_{scb} cross at an optimal CGS thickness of 0.21 µm, satisfying the current matching condition: $J_{sct} = J_{scb} = 19.34$ mA/cm^2. To optimize the efficiency of CGS/CIGS tandem cell, the current-density (J_{sc}) is constrained by an optimum value between the J_{sct} and J_{scb} named: The current matching point.

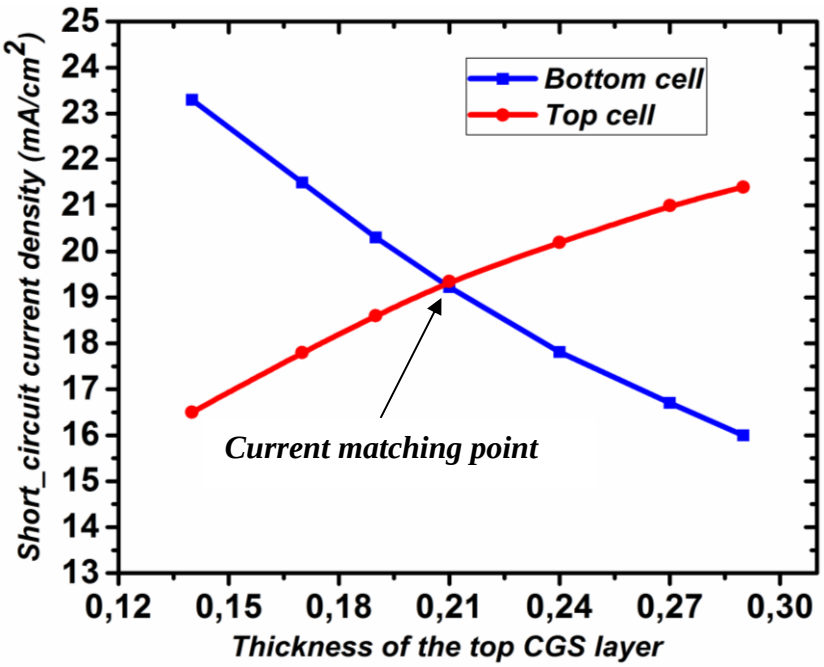

Fig. III.20: Short-circuit current densities of the CIGS bottom-cell and CGS top-cell as a function of CGS layer thickness.

Fig. III.21 displays the conversion efficiency η of CGS/CIGS tandem solar cell plotted as a function of CGS layer thickness. The tandem cell efficiency reaches a maximum of 27.7% at the optimal CGS layer thickness of 0.21 µm, where the current matching condition between the top and bottom cells is achieved. The tandem cell efficiency gradually increases from 24.13%

at 0.14 µm to a maximum of 27.7% as the CGS layer thickness increases. However, it decreases from the maximum back to around 25.04% at 0.29 µm.

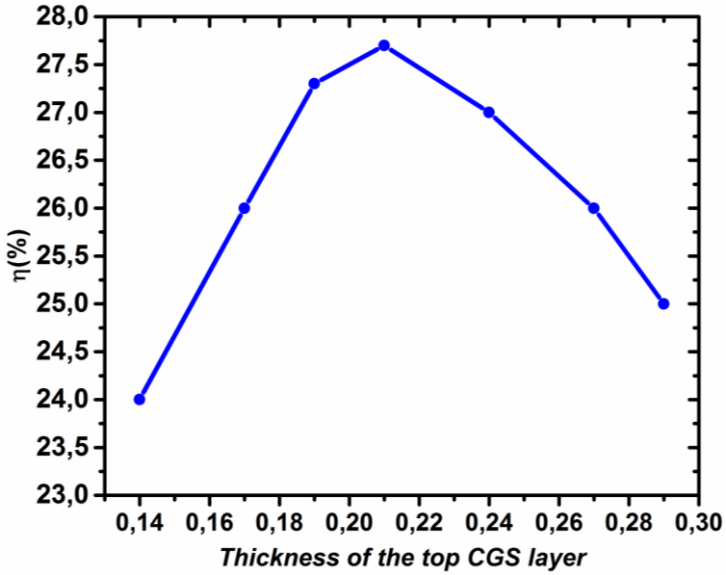

Fig. III.21: Conversion efficiency of CGS/CIGS tandem solar cell as function of CGS layer thickness.

The J-V characteristics of top-cell, bottom-cell and tandem solar cell are presented in Fig. III.22. The optimum CGS layer thickness was set at 0.21 µm as a matching condition point corresponds a maximum of short-circuit current density J_{sc} of about 19.34 mA/cm^2. Additionally, the individual V_{oc} of the top and bottom cells are 1.08 V and 0.72 V, respectively. the open-circuit voltage V_{oc} obtained of CGS/CIGS tandem cell is 1.81 V, which is exactly equal to the sum of V_{oc} of both the top and bottom cells. The conversion efficiency has been increased to 27.7% under current matching point condition. The improvement over the 25.85% conversion efficiency was observed for CGS/CIGS tandem cell that operated with mismatched short-circuit current densities.

Finally, to achieve maximum efficiency, it is necessary to work in the optimal condition named "current matching point", where the top, bottom and tandem cells exhibit the same short-circuit current density J_{sc} of about19.34 mA/cm^2. This value is exactly the maximum J_{sc} of CGS/CIGS tandem solar cell at the optimal CGS layer thickness. We notice that the photovoltaic behavior of CGS/CIGS tandem solar cell is largely due to the light absorption by the top-cell, which is dependent on the thickness of CGS layer.

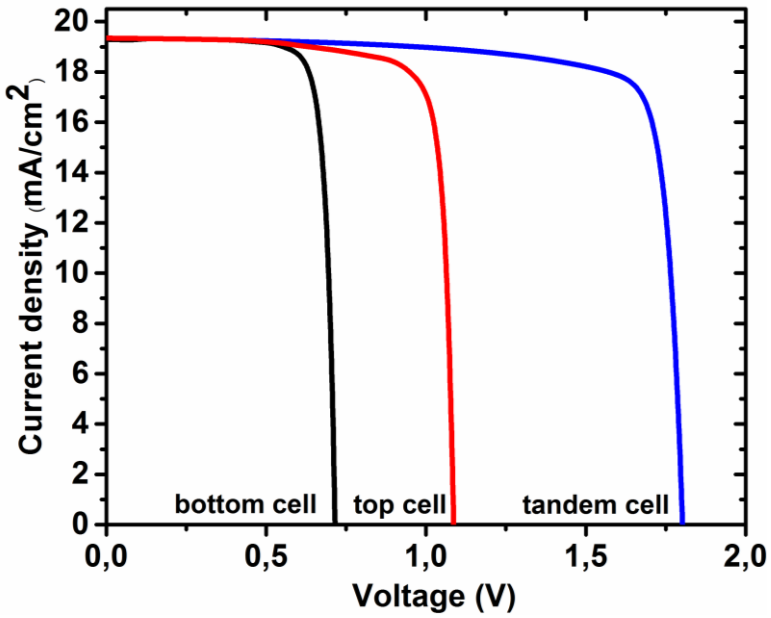

Fig. III.22: J-V characteristics of CGS top-cell, CIGS bottom-cell, and CGS/CIGS tandem solar cell under current matching condition.

In the next section, we will add a third cell to tandem solar cell to achieve a higher conversion efficiency of new design CGS/CIGS triple-junction solar cells.

III.6. Modeling of CGS/CIGS triple-junction solar cell

Triple-junction solar cell is configured by using three different cells (top, middle and bottom). The presentation of this structure including the name, the thickness and band-gap energy of each layer was given by Fig. III.23. A CGS thin layer with a bang-gap of 1.69 eV was used in the top-cell. The CIGS absorber layer with a band-gap energy of 1.36 eV was used in the middle-cell and a slightly thick CIGS absorber layer was used in the bottom-cell with a band gap energy of 1.16 eV [32]. All these layers are coupled with a ZnO window layer which acts as a transparent conducting oxide, TCO, layer [14]. Table III.6 presents the input data parameters for each layer used in the simulation by SILVACO/Atlas software using a drift diffusion transport model. The proposed design aims to transmit the maximum number of incident photons and to generate sufficient output power.

The CGS/CIGS triple-junction cell was illuminated by a power density of 100 mW/cm^2 under AM1.5 G solar spectrum. The photons are incident normally onto the ZnO window layer used as front cathode contact, however, a Molybdenum Mo layer was used as back anode contact.

Table III.6: Material parameters used in the simulation.

Parameter	**CdS**	**CGS/CIGS/CIGS**
Band gap energy *Eg* (eV)	2.4	1.69/1.36/1.16
Electron affinity χe (eV)	4.2	4.5
Relative permittivity ε_r (F.cm^{-1})	10	13.6
Density of states at conduction band N_C (cm^{-3})	2.2×10^{18}	2.2×10^{18}
Density of states at valence band N_V (cm^{-3})	1.8×10^{19}	1.8×10^{19}
Electron mobility μn (cm^2/Vs)	100	100
Hole mobility μp (cm^2/Vs)	25	25
Gaussian defect states	**CdS**	**CGS/CIGS/CIGS**
Gaussian defect density N_{GA} , N_{GD} (cm^{-3})	10^{15} (A)	10^{15} (D)
Peak energy position E_{GA} , E_{GD} (eV)	1.2 (A)	0.84/0.68/0.58 (D)
Standard energy deviation W_{GA} , W_{GD} (eV)	0.1 (A)	0.1 (D)
Electron capture cross section σ_n (cm^2)	10^{-15}	$2*10^{-15}$
Hole capture cross section σ_p (cm^2)	10^{-17}	$3*10^{-13}$

Surface recombination velocity for electrons and holes (cm.s^{-1})	S_n	S_p
CdS/CGS interface	10^5	10^5
CdS/CIGS interface	10^5	10^5
CdS/CIGS interface	10^5	10^5
Front contact	10^5	10^5
Back contact	10^5	10^5

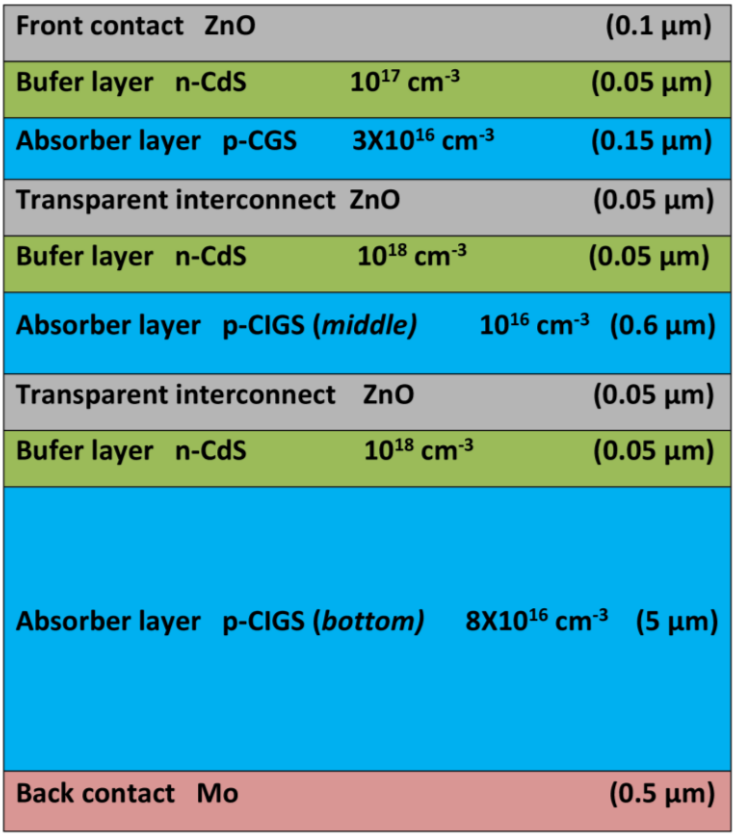

Fig. III.23: Design of CGS/CIGS triple-junction solar cell studied, an interconnect formed by transparent ZnO was used to connect the sub-cells.

III.6.1. Modeling of individual CGS, $CIGS_M$ and $CIGS_B$ solar cells

Individual (single) CIGS solar cell consists of a heap of layers with an active area of 1 cm^2. The structure from bottom to top consist of: A back metal contact of Mo (0.5 µm), a p-CIGS absorber layer (5 µm) with x = 0.33 (E_g = 1.16 eV), an n-doped CdS buffer layer (0.05 µm) and finally a ZnO window layer (0.1 µm). The geometrical dimensions of the proposed structure are similar to those available in the Ref. [40] and are shown in Fig. III.24.

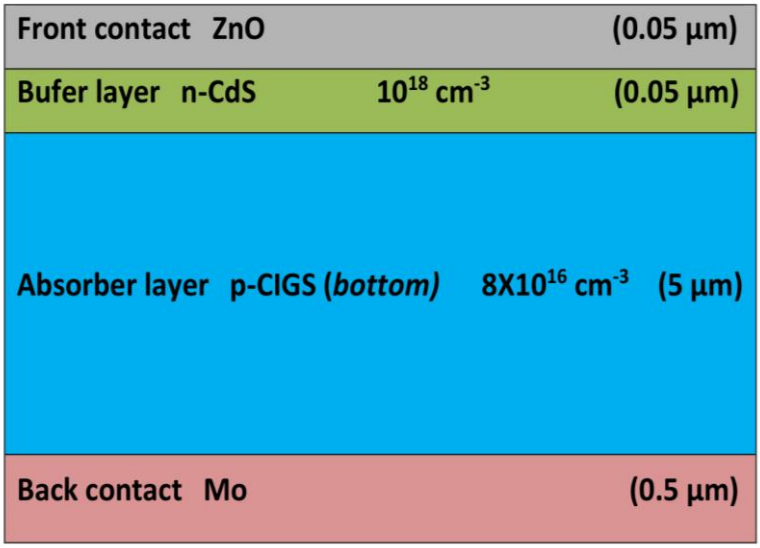

Fig. III.24: Single CIGS solar cell structure.

The CIGS top and middle cells are similar to the previous CIGS bottom-cell studied in the last section, but with different layer characteristics. Specifically, the CIGS middle-cell consists of p-type CIGS absorber layer, n-type CdS buffer, ZnO window layer on top and Mo back contact layer. This structure is shown in Fig. III.25, with Ga composition x = 0.66 and an energy band-gap of 1.36 eV.

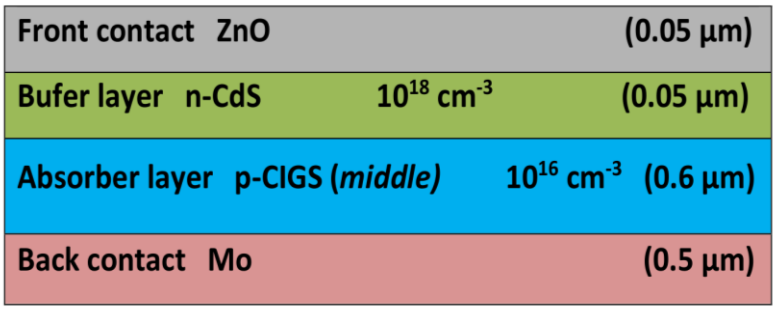

Fig. III.25: Single CIGS middle-cell structure.

On the other hand, the top-cell based on CGS absorber layer consists of p-CGS absorber, n-type CdS buffer, ZnO window layer as a TCO material, with Ga composition x = 1 and an

energy band-gap of 1.69 eV, as seen in Fig. III.26. The doping concentrations of CGS, CIGS, and CdS layers were optimized to enhance the conversion efficiency of the cells and were mentioned in Fig. III.24-26.

Front contact ZnO		(0.1 µm)
Bufer layer n-CdS	10^{17} cm^{-3}	(0.05 µm)
Absorber layer p-CGS	$3X10^{16}$ cm^{-3}	(0.15 µm)
Back contact Mo		(0.5 µm)

Fig. III. 26: Single CGS top-cell structure.

Fig. III.27 shows the J-V characteristics for the individual CGS and CIGS solar cells. To verify the accuracy of our model, we compared the performance parameters of CIGS bottom-cell with those reported in the literature, and the findings are presented in Table III.4.

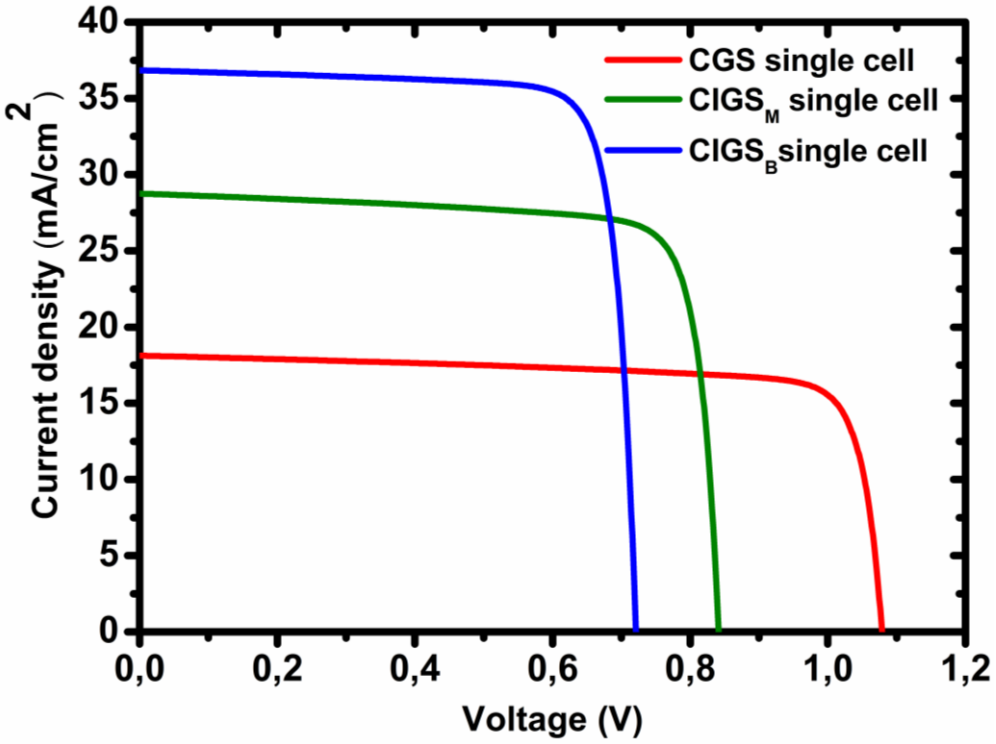

Fig. III.27: J-V characteristics for $CIGS_B$ single-cell, $CIGS_M$ single-cell and CGS single-cell.

III.6.2. Photovoltaic parameters of CGS/CIGS triple-junction solar cell

Fig. III.28 displays the J-V characteristics for 4 types of cells: CGS top-cell, CIGS middle-cell, CIGS bottom-cell and CGS/CIGS triple-junction solar cell. Table III.7 provides a summary of the electrical parameters these different cells.

Table III.7: Photovoltaic parameters of CIGS bottom-cell, CIGS middle-cell, CGS top-cell and CGS/CIGS triple-junction solar cells.

# Solar cell structure	J_{sc} (mA/cm^2)	V_{oc} (V)	*FF* (%)	η (%)
CGS single cell	18.13	1.08	80.35	15.79
CGS top-cell	17.58	1.08	80.79	15.41
CIGS single cell	28.75	0.84	81.03	19.71
CIGS middle-cell	16.26	0.83	78.20	10.58
CIGS bottom-cell	13.36	0.71	82.17	07.69
CGS/CIGS triple-junction cell	13.49	2.64	86.56	30.85

It has been observed that the open-circuit voltage of CGS/CIGS triple-junction cell is found to be 2.64 V and is equivalent to the sum of open-circuit voltage for the top, middle and bottom cells i.e., 1.08, 0.83 and 0.71 Volt, respectively. It is important to mention that the proposed model of CGS/CIGS triple-junction solar cell is correct. Our opinion is validated by the J_{sc} current of triple-junction cell (13.35 mA/cm^2) which is limited by small current of CIGS bottom-cell of about 13.17 mA/cm^2. This observation regarding the non-ideal current matching between the top, middle and bottom cells.

The fill factor of triple-junction is observed to be 86.56% with an efficiency of 30.85% which is better than the top-cell 80.79% with an efficiency of 22.01%, and about 78.2% of middle-cell with efficiency of 19.71% and finally about 82.17% of bottom-cell with an efficiency of 15.79%. Upon comparing the results of the CIGS single cell with the CIGS bottom-cell in the triple-junction solar cell, a significant decrease in the photovoltaic parameters of the CIGS bottom-cell can be observed. This degradation can be attributed to the top layers absorbing a portion of the incident light.

It is noteworthy that the obtained results of CGS/CIGS triple-junction solar cell have not been previously reported.

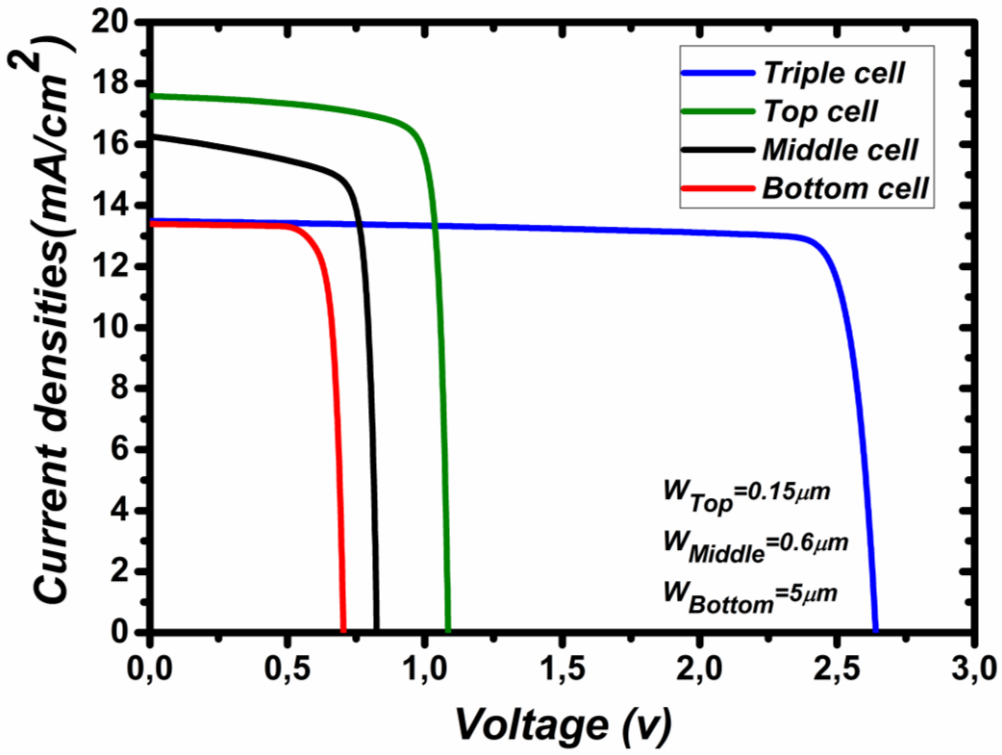

Fig. III.28: J-V characteristics for CIGS bottom-cell, CIGS middle-cell, CGS top-cell and CGS/CIGS triple-junction solar cell.

III.6.3. Optimization of photovoltaic cell parameters

By reducing the thickness of the top and middle cells in a triple-junction solar cell, the distribution of light between the three sub-cells can be altered, resulting in an increase in the current of the bottom-cell at the expense of the top and middle cells. However, for optimal efficiency, the short-circuit current density of the bottom-cell (J_{scb}) must be lower than that of the top-cell (J_{sct}) and middle-cell (J_{scm}). In such cases, reducing the thickness of the middle and top cells can achieve current matching point, where $J_{scb} = J_{scm} = J_{sct} = J_{sc}$. This ensures that the triple-junction cell current density is limited by the lowest of J_{scb}, J_{scm} and J_{sct}. The cell efficiency is optimized by reducing the thickness of the top and middle cells to achieve current matching.

To improve the performance of the CGS/CIGS triple-junction solar cell, we conducted calculations that involved adjusting the thickness of the CGS layer in the top-cell from 0.1 µm to 0.15 µm, while simultaneously varying the thickness of the CIGS layer in the middle-cell from 0.3 µm to 0.5 µm. While maintaining a constant thickness of 5 µm for the CIGS layer in the bottom-cell, the optimal range of thickness for the best performance was identified through the cell's structure, as illustrated in Fig. III.23.

Fig. III.29 illustrates how the open-circuit voltage (V_{oc}) of the triple-junction cell is affected by changes in the thicknesses of the CGS and CIGS layers. Across the entire range of thicknesses, an increase in both CGS and CIGS thicknesses leads to an increase in the open-circuit voltage. It is worth noting that the minimum voltage is 2.57 Volt at the lowest pair of thicknesses (0.12 µm CGS and 0.3µm CIGS), while the maximum voltage is 2.63 V at the highest pair of thicknesses (0.15µm CGS and 0.5µm CIGS). This indicates that both the CGS and CIGS thicknesses have a same impact on the V_{oc} of the triple-junction cell. Additionally, the open-circuit voltage of the triple-junction cell in all cases is simply the sum of the open circuit voltages of the top, middle, and bottom cells.

The variation of the fill factor of CGS/CIGS triple-junction solar cell with changes in the thicknesses of the CGS and CIGS layers can be observed in the Fig. III.30. When the thicknesses of CGS and CIGS layers are set at 0.12 and 0.4, respectively, the fill factor of the triple-junction solar cell drops to a minimum value of 78% to 81%. It's worth mentioning that the fill factor is directly affected by any changes made to the CIGS layer thickness in the middle cell.

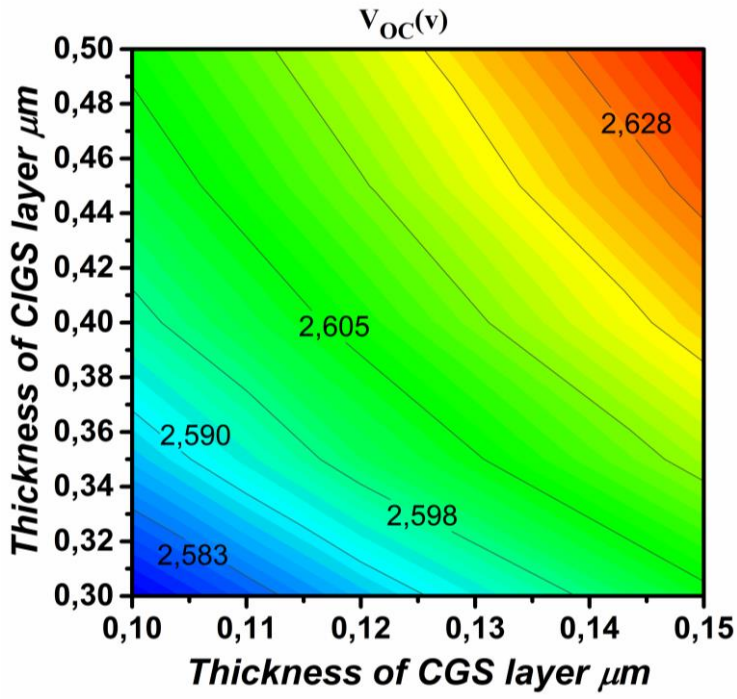

Fig. III.29: Contour plot of V_{oc} variation as a function of CGS and CIGS layers thicknesses.

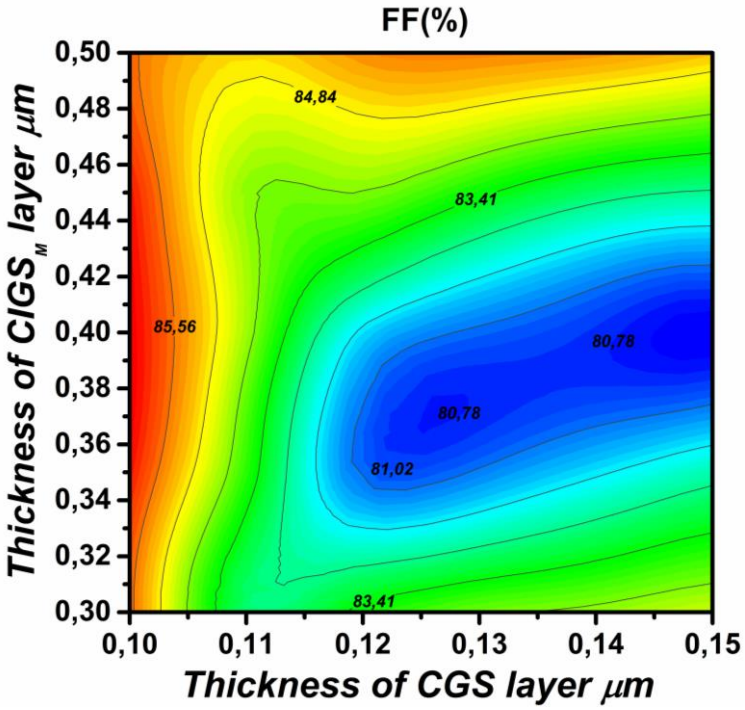

Fig. III.30: Contour plot of *FF* variation as a function of CGS and CIGS layers thicknesses.

Fig. III.31 illustrates the short-circuit current density J_{sc} of triple-junction as a function of CGS and CIGS layers thicknesses. The results suggest that a thickness of 0.12 µm for CGS layer and 0.4 µm for CIGS layer achieves a maximum J_{sc} of about 15.58 mA/cm^2. We can consider this value as a current matching point.

Fig. III.32 showcases contour plots that display the correlation between changes in the thickness of CGS and CIGS layers and the energy conversion efficiency. It's clear that the thicknesses of the CGS and CIGS layers correspond to the point (0.12 µm, 0.4 µm) where the highest efficiency level of about 33.27% is achieved. The top, middle, and bottom cells reach optimal current exactly in current matching point.

Fig. III.33 illustrates the J-V curves, which exhibit the electrical properties of the recommended solar cell design at the ideal thicknesses of the top and middle layers, approximately 0.12 and 0.4 µm, respectively. As a result, Table III.8 summarizes the photovoltaic properties of the solar cell design at the current matching point.

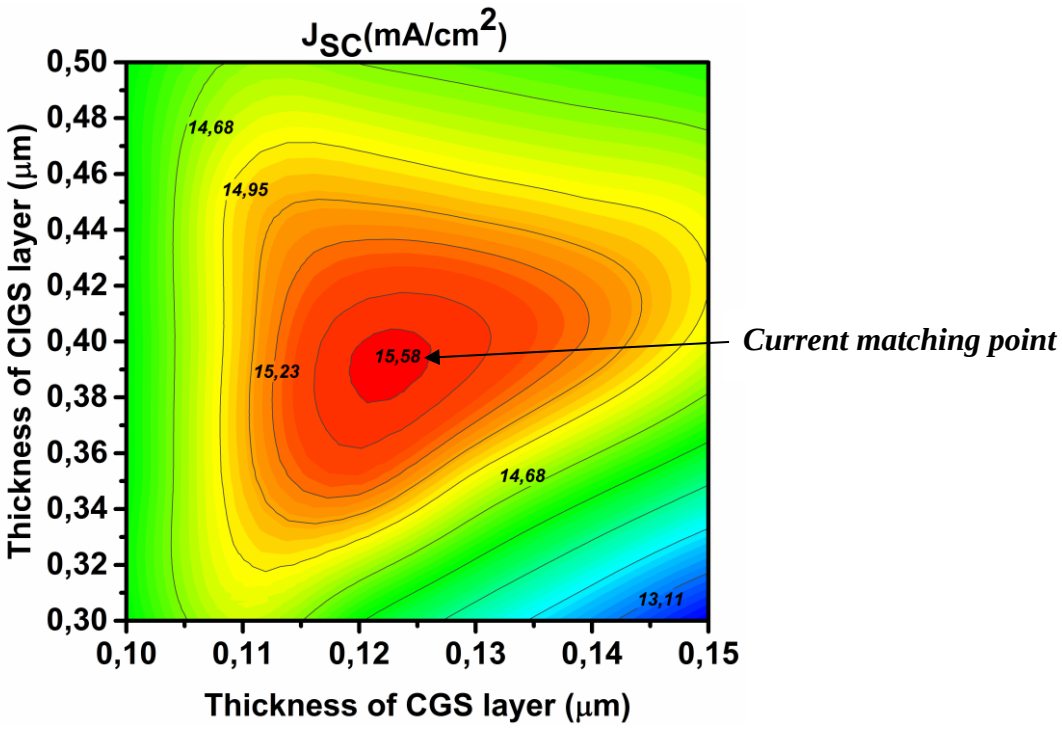

Fig. III.31: Short-circuit current densities of CGS/CIGS triple-junction solar cell as a function of CGS and CIGS layers thicknesses.

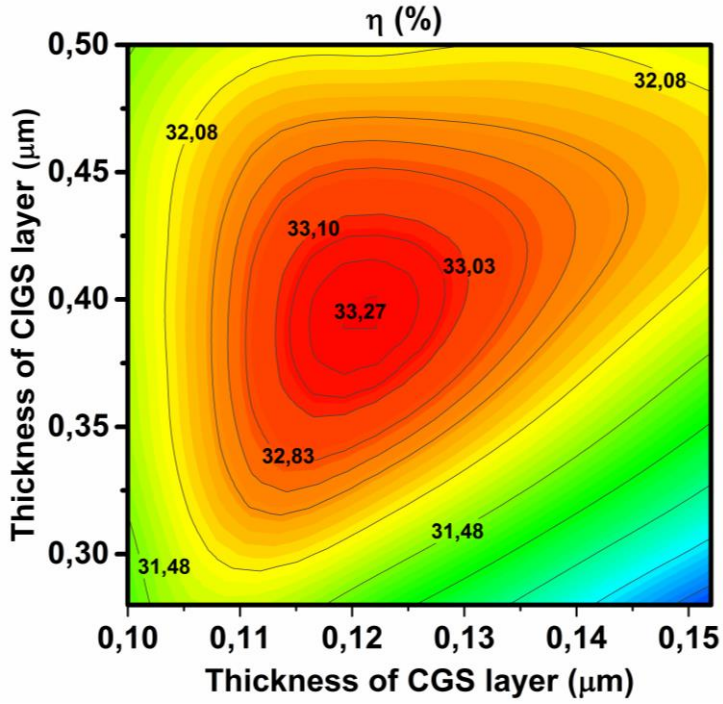

Fig. III.32: Efficiency variation of CGS/CIGS triple-junction solar cell as a function of CGS and CIGS layers thicknesses.

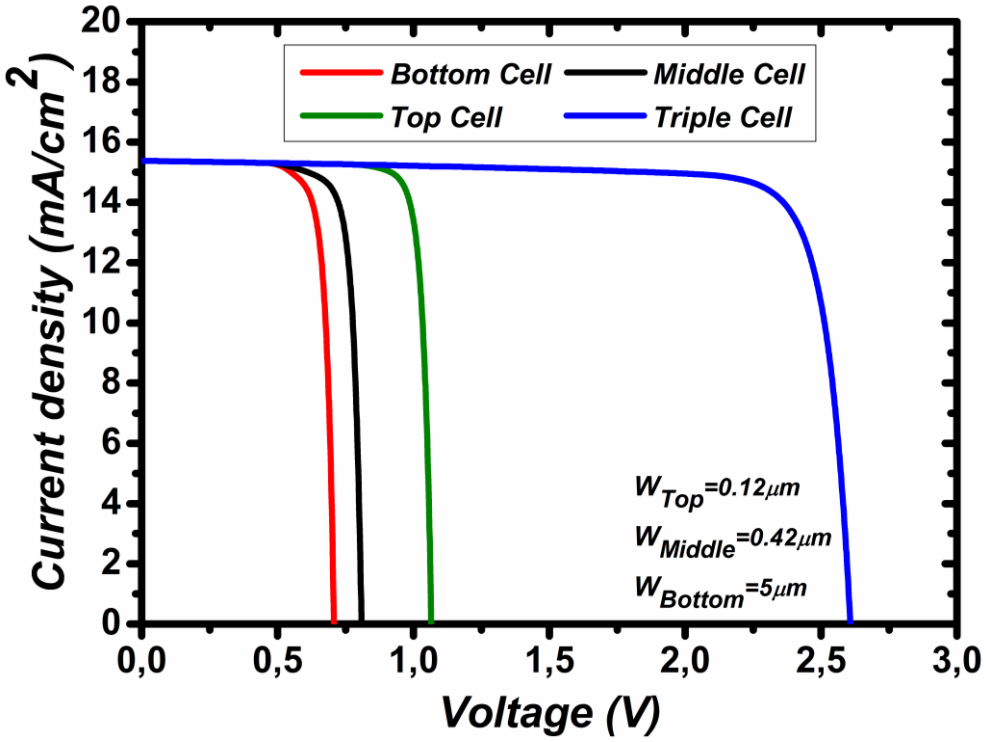

Fig. III.33: J-V characteristics of CGS top-cell, CIGS middle-cell, CIGS bottom-cell and CGS/CIGS triple junction solar cell under optimized J_{sc} current.

At the current matching point, all cells -top, -middle, -bottom, and triple-junction achieve their maximum short-circuit current densities, reaching J_{sc} = 15.58 mA/cm^2. The triple-junction cell has an open-circuit voltage (V_{oc}) of 2.6 V, which is the sum of the V_{oc} of the top-cell (1.07 V), middle-cell (0.82 V) and bottom-cell (0.71 V). This result show that the conversion efficiency of the triple-junction cell was enhanced to 33.27%, due to current matching point, which is an improvement from the 30.85% achieved for the CGS/CIGS triple-junction in section III.6.2.

Table III.8: Photovoltaic parameters of CGS top-cell, CIGS middle-cell, CIGS bottom-cell and CGS/CIGS triple-junction solar cells optimized under current matching point condition.

	J_{sc} (mA/cm^2)	V_{oc} (V)	*FF* (%)	η (%)
CGS top-cell	15.58	1.07	84.21	14.14
CIGS middle-cell	15.58	0.82	78.72	10.07
CIGS bottom-cell	15.58	0.71	82.34	09.06
CGS/CIGS triple-junction cell	15.58	2.60	84.13	33.27

III.7. Conclusion

In conclusion, our study demonstrates the utility of SILVACO/Atlas in modeling CIGS solar cells to optimize design and fabrication parameters, such as layer thicknesses, doping concentrations, and material defects. By analyzing different designs and configurations, we can identify the most efficient and cost-effective solar cell structures.

Our work specifically focused on three heterojunction solar cell structures (substrate, tandem and triple-junction), and we used 2D SILVACO/Atlas simulator to analyze their performance under various conditions. By varying factors such as thicknesses, carrier concentration, defect density and operating temperature, we were able to extract photovoltaic parameters and investigate the impact on the overall performance of the cells. The use of SILVACO/Atlas in our research highlights its powerful role in the development of high-performance solar energy technologies.

References

[1] Li, D., Song, L., Chen, Y., Huang, W. (2019). Modeling Thin Film Solar Cells: From Organic to Perovskite. Advanced Science, 1901397.doi:10.1002/advs.201901397

[2] Software, D. S. Atlas User's Manual. 567-1000 (2016).

[3] Benabbas, S., Rouabah, Z., Bouarissa, N., Chelali, N. (2016). The role of back surface field SnS layer in improvement of efficiency of CdTe thin film solar cells, Optik. 127 6210-6217. https://doi:10.1016/j.ijleo.2016.04.050.

[4] Cherouana, A., Labbani, R. (2018). Numerical simulation of CZTS solar cell with silicon back surface field, Mater. Today Proc. 5 13795-13799.https://doi:10.1016/j.matpr.2018.02.020.

[5] Kim, S., Dao, V.A. Shin, C., Balaji, N., Yi, J. (2014). Influence of n-doped μc-Si: H back surface field layer with micro growth in crystalline-amorphous silicon heterojunction solar cells, J. Nanosci. Nanotechnol. 14 9258-9262.https://doi:10.1166/jnn.2014.10123

[6] Rawat, A., Sharma, M., Chaudhary, D., Sudhakar, S., Kumar, S. (2014). Numerical simulations for high efficiency HIT solar cells using microcrystalline silicon as emitter and back surface field (BSF) layers, Sol. Energy. 110 691-703.

[7] Ouédraogo, S., Zougmoré, F., Ndjaka, J. (2014). Computational analysis of the effect of the surface defect layer (SDL) properties on Cu (In, Ga) Se_2-based solar cell performances, J. Phys. Chem. Solids. 75 688-695.https://doi:10.1016/j.jpcs.2014.01.010.

[8] Pudov, A., Kanevce, A., Al-Thani, H. J. (2005). Secondary barriers in CdS-$CuIn_{1-x}Ga_xSe_2$ solar cells, J. Appl. Phys. 97, 064901.https://doi:10.1063/1.1850604.

[9] Bouabdelli, M. W., Rogti, F., Maache, M., Rabehi, A. (2020). Performance enhancement of CIGS thin-film solar cell. Optik. 216, 164948. https://doi:10.1016/j.ijleo.2020.164948.

[10] Wagner, S., Shay, J. L., Migliorato, P., Kasper, H. M. (1974). $CuInSe_2$/CdS heterojunction photovoltaic detectors. Applied Physics Letters. 25(8), 434-435. https://doi:10.1063/1.1655537.

[11] Inc. Silvaco, Atlas User's Manual. Santa Clara, CA 95054, California (2017).

[12] Elbar, M., Tobbeche, S. (2015). Numerical Simulation of CGS/CIGS Single and Tandem Thin-film Solar Cells using the Silvaco-Atlas Software. Energy Procedia. 74, 1220-1227. https://doi:10.1016/j.egypro.2015.07.766.

[13] Repins, I., Contreras, M., Romero, M., Yan, Y., Metzger, W., Li, J., Noufi, R. (2008). Characterization of 19.9%-efficient CIGS absorbers. In 33rd IEEE Photovoltaic Specialists Conference (pp. 1-6). IEEE.https://doi:10.1109/pvsc.2008.4922628.

[14] Gloeckler, M., Sites, J. R., Metzger, W. K. (2005). Grain-boundary recombination in Cu(In,Ga)Se_2 solar cells. Journal of Applied Physics. 98(11), 113704. https://doi:10.1063/1.2133906.

[15] Heriche, H., Rouabah, Z., Bouarissa, N. (2017). New ultra-thin CIGS structure solar cells using SCAPS simulation program. International Journal of Hydrogen Energy. 42(15), 9524-9532. https://doi:10.1016/j.ijhydene.2017.02.099.

[16] Biplab, S. R. I., Ali, M. H., Moon, M. M. A., Pervez, M. F., Rahman, M. F., Hossain, J. (2019). Performance enhancement of CIGS-based solar cells by incorporating an ultrathin $BaSi_2$ BSF layer. Journal of Computational Electronics. 19(1), 342-352. https://doi:10.1007/s10825-019-01433-0.

[17] Mutch, M. J., Pomorski, T., Bittel, B. C., Cochrane, C. J., Lenahan, P. M., Liu, X., Nemanich, R., Brockman, J., French, M., Kuhn, M., French, B., King, S. W. (2016). Band diagram for low-k/Cu interconnects. The starting point for understanding back end of line (BEOL) electrical reliability. Microelectronics Reliability. 63, 201-213. https://doi:10.1016/j.microrel.2016.04.004.

[18] Chelvanathan, P., Hossain, M. I., Amin, N. (2010). Performance analysis of copper-indium-gallium-diselenide (CIGS) solar cells with various buffer layers by SCAPS. Current Applied Physics. 10(3), 387-391. https://doi:10.1016/j.cap.2010.02.018.

[19] Benmir, A., Aida, M. S. (2013). Analytical Modeling and Simulation of CIGS Solar Cells. Energy Procedia. 36, 618-627. https://doi:10.1016/j.egypro.2013.07.071.

[20] Heriche, H., Rouabah, Z., Bouarissa, N. (2016). High-efficiency CIGS solar cells with optimization of layers thickness and doping. Optik - International Journal for Light and Electron Optics. 127(24), 11751-11757. https://doi:10.1016/j.ijleo.2016.09.071.

[21] Boudour, S., Bouchama, I., Bouarissa, N., Hadjab, M. (2019). A study of CdTe solar cells using Ga-doped $Mg_xZn_{1-x}O$ buffer/TCO layers: Simulation and performance analysis. Journal of Science: Advanced Materials and Devices. 4(1), 111-115. https://doi:10.1016/j.jsamd.2018.12.001.

[22] Rougieux, F. E., Sun, C., Macdonald, D. (2018). Determining the charge states and capture mechanisms of defects in silicon through accurate recombination analyses: A review. Solar Energy Materials and Solar Cells. 187, 263-272. https://doi:10.1016/j.solmat.2018.07.029.

[23] Amin, N., Sopian, K., Konagai, M. (2007). Numerical modeling of CdS/CdTe and CdS/CdTe/ZnTe solar cells as a function of CdTe thickness. Solar Energy Materials and Solar Cells. 91(13), 1202-1208. https://doi:10.1016/j.solmat.2007.04.006.

[24] Tanaka, K., Oonuki, M., Moritake, N., Uchiki, H. (2009). $Cu_2ZnSnS_4Cu_2ZnSnS_4$ thin film solar cells prepared by non-vacuum processing. Solar Energy Materials and Solar Cells. 93(5), 583-587. https://doi:10.1016/j.solmat.2008.12.009.

[25] Jimbo, K., Kimura, R., Kamimura, T., Yamada, S., Maw, W. S., Araki, H., Katagiri, H. (2007). $Cu2ZnSnS_4$-type thin film solar cells using abundant materials. Thin Solid Films. 515(15), 5997-5999. https://doi:10.1016/j.tsf.2006.12.103.

[26] Kato, T., Wu, J., Hirai, Y., Sugimoto, H., Bermudez, V.: Record Efficiency for Thin-Film Polycrystalline Solar Cells Up to 22.9% Achieved by Cs-Treated Cu(In,Ga)(Se,S). IEEE Journal of Photovoltaics, 9(1), 325-330. https://doi:10.1109/jphotov.2018.2882206.

[27] Ghorbani, T., Zahedifar, M., Moradi, M., Ghanbari, E. (2020). Influence of affinity band gap and ambient temperature on the efficiency of CIGS solar cells. Optik.223, 165541. https://doi:10.1016/j.ijleo.2020.165541.

[28] Ramanathan, K., Contreras, M.A., Perkins, C.L., Asher, S., Hasoon, F.S., Keane, J., Young, D., Romero, M., Metzger, W., Noufi, R., Ward, J., Duda, A. (2003). Properties of 19.2% efficiency ZnO/CdS/$CuInGaSe_2$ thin-film solar cells. Prog. Photovolt. Res. Appl.5, 4. https:// doi. org/ 10. 1002/ pip. 494.

[29] Yang, X., Chen, B., Chen, J., Zhang, Y., Liu, W., Sun, Y. (2018). ZnS thin film functionalized as back surface field in Si solar cells. Mater. Sci. Semicond. Process. https:// doi. org/ 10. 1016/j. mssp. 2017. 08. 011.

[30] Kohara, N., Nishiwaki, S., Hashimoto, Y., Negami, T., Wada, T. (2001). Electrical properties of the Cu(In, Ga)Se_2/$MoSe_2$ /Mo structure. Sol. Energy Mater. Sol. Cells. https:// doi. org/ 10. 1016/ S0927- 0248(00) 00283-X

[31] Fathi, M., Abderrezek, M., Djahli, F., Ayad, M. (2015). Study of thin film solar cells in high temperature condition. Energy Procedia.74, 1410-1417.https://doi.org/10.1016/j.egypro.2015.07.788

[32] Jackson, P., Hariskos, D., Lotter, E., Paetel, S., Wuerz, R., Menner, R., Wischmann, W., Powalla, M. (2011). New world record efficiency for Cu(In,Ga)Se_2 thin-film solar cells beyond 20%. Prog. Photovoltaics Res. Appl. 19, 894-897.

[33] Raymond J. Kilway ii. thesis; five junction solar cell optimization using silvaco atlas. naval postgraduate school monterey, california. September 2017

[34] Olson, J.M., Friedman, D.J., Kurtz, S. (2003). Handbook of Photovoltaic Science and Engineering, first ed. John Wiley and Sons, West Sussex

[35] Silvaco, Inc. Atlas user's Manual device simulation software. 701 Patrick Henry Drive, Bldg. 2 March 20, 2012.

[36] Paulson, P.D., Birkmire, R.W., Shafarman, W.N. (2003). Optical characterization of $CuIn_{1-x}Ga_xSe_2$ alloy thin films by spectroscopic ellipsometry. J. Appl. Phys. 94, 879-888.

[37] Palik, E.D. (1998). Handbook of Optical Constants of Solids III. Boston Academic press, San Diego, London.

[38] Richter, M., Schubbert, C., Eraerds, P., Riedel, I., Keller, J., Parisi, J., Dalibor, T., Avella´n-Hampe, A. (2013). Optical characterization and modeling of Cu(In,Ga)$(Se,S)_2$ solar cells with spectroscopic ellipsometry and coherent numerical simulation. Thin Solid Films 535, 331-335.

[39] Jiyon, S., Sheng, S.L., Huang, C.H., Anderson, T.J., Crisalle, O.D. (2003). Modeling and simulation of a $CuGaSe_2$ /Cu(In, Ga)Se_2 tandem solar cell. In: Proc. 3rd World Conference on Photovoltaic Energy Conversion, Osaka, Japan, pp. 555-558.

[40] Bouanani B, Joti A, Bachir Bouiadjra FS, Kadid A. (2020). Band Gap And Thickness Optimization For Improvement Of CIGS/CIGS Tandem Solar Cells Using Silvaco Software, Optik,doi: https://doi.org/10.1016/j.ijleo.2020.164217.

Chapter IV: Impact of crystalline defects in CIGS material on CIGS solar cell performances

Chapter IV
Impact of crystalline defects in CIGS material on CIGS solar cell performances

IV.1 introduction

The focus of this chapter is to examine the impact of the ordered defect compound layer formation between the buffer layer and absorber component on solar cell performance. Through a lot of works, it is demonstrated that the presence of this defect layer plays a crucial role in enhancing the photovoltaic performance of CIGS devices. In the second section, we will present the results of activation energies effects for acceptor and donor levels, E_A and E_D Trap states, respectively, carried out using SILVACO/Atlas software.

IV.2 Ordered defect compound layer formation

Several hypotheses have been proposed in the literature to explain the formation of the p-n junction in the In_2Se_3/CIGS and/or In_2S_3/CIGS structures. Recently, a study conducted by S. Gall et *al*. focused on elucidating this phenomenon specifically in the In_2Se_3/CIGS structure [1]. Their investigation was based on analyzing the phase diagram of the Cu-In-Se system and the atomic diffusion of copper towards In_2Se_3 from CIGS. The authors concluded that when the concentration of copper is significant, it can be integrated into the crystal structure of In_2Se_3, forming solid solutions known as Ordered Defect Compounds (ODC). Several examples of such compounds are $CuIn_3Se_5$, $CuIn_5Se_8$, and $Cu_2In_4Se_7$.

K. Djessas et *al.* [2] conducted experimental research on the In_2Se_3/CIGS/SnO_2:F/glass structure, revealing that depositing In_2Se_3 or (In,Se) on a CIGS layer creates a p-n junction in the p-CIGS absorbing layer close to SnO_2:F [2-4]. When light is passed through SnO_2:F, it generates a significant voltage of approximately 600 mV. The p-n junction is formed spontaneously if the temperature higher than 300°C while depositing In_2Se_3 on CIGS. The inter-diffusion of intrinsic atoms, particularly copper Cu and indium In, from the thin (In,Se) and CIGS layers leads to the spontaneous creation of a pseudo-homojunction in the In_2Se_3/CIGS couple [5]. This pseudo-homojunction is created by transforming a portion of the p-CIGS absorber from p-type to n-type.

According to Zunger et *al.* [6,7], In_{Cu} point defects have a deep donor level (250 meV) and have a high formation energy. Conversely, complex defects ($2V_{Cu}^{-} + In_{Cu}^{++}$) have shallow

donor levels and very low or negative formation energies for ($2V_{Cu}^{-} + In_{Cu}^{++}$), owing to the strong electronic attraction between V_{Cu} and In_{Cu} point defects. Complex defects are stable and can form a secondary Structure within the CIGS matrix, as illustrated in Fig. IV.1.

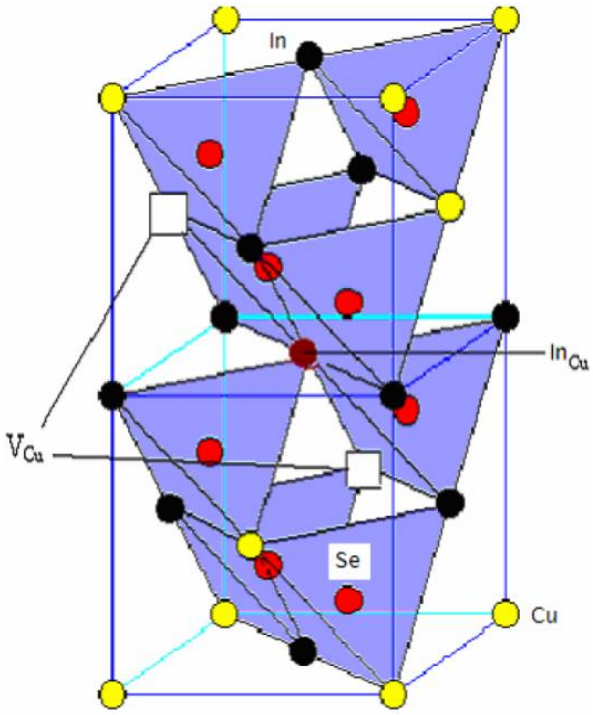

Fig. IV.1: Structural model of defect pair ($2V_{Cu}^{-} + In_{Cu}^{++}$) in a $CuInSe_2$ matrix proposed by Zunger et *al.* [8].

IV.3. ODC layer impact

The simulation uses a simple model depicted in Fig. IV.2, which can define the cell structure using a maximum of five regions with distinct material parameters.

In this simulation, the solar cell model comprises of Mo/CIGS/ODC/In_2Se_3/ZnO solar cell structure, where the ZnO layer serves as a window layer to enter the sun light. Including an n-type layer of Ordered Defect Compounds (ODC) between the In_2Se_3 and CIGS layers in the model is highly significant. Typically, this layer is formed through experimental means by depositing an In_2Se_3 buffer layer onto Mo/CIGS substrate with a high substrate temperature.

The primary objective for using SILVACO/Atlas tool is to demonstrate the impact of ODC layer on the performance of CIGS solar cell. This layer has a larger band-gap than CIGS, which reduces recombination at the buffer/absorber interface, resulting in improved cell

performance [9,10]. Furthermore, the ODC inversion layer that formed between In_2Se_3 and CIGS thin films has been defined by some authors as:

- The nature of the interface formed has a significant impact on the performance of CIGS solar cell. Interface formed is critical area of interaction between the different layers: materials possessing various crystalline structures, lattice parameters, electron affinities, and diffusion coefficients [11].
- The presence of a discontinuity at the buffer/absorber interface impacts the junction quality between the buffer layer and CIGS absorber, it affects the flow of minority carriers in the device. However, this energy barrier could be advantageous as it increases the n-type inversion at the absorber's surface by bringing the buffer layer closer to the Fermi level. This surface inversion is crucial to prevent interfacial recombination [12].
- Several diffusion phenomena occur at this interface: copper diffuses into In_2Se_3, and indium diffuses from In_2Se_3 into CIGS absorber [13]. Additionally, the surface layer of CIGS has naturally occurring physical properties that differ from those of the volume, creating a hetero-interface within the absorber [14,15]. Some research groups suggest that the surface of CIGS be covered with an n-ODC layer derived from the ordered chalcopyrite structure of CIGS by replacing In with Cu sites and leaving some Cu sites vacant [16,17]. According to calculations conducted by Zhang Wei and Zunger, the ($2V_{Cu}^{-} + In_{Cu}^{++}$) defect pair exhibits unusually low formation energy and is electronically inactive. $CuIn_5Se_8$, $CuIn_5Se_6$, and $Cu_3In_5Se_9$ are explained to exist as a repetition of a single unit of defects ($2V_{Cu}^{-} + In_{Cu}^{++}$) [18,19]. This allows the p-n junction to form between the n-deficient copper-doped CIGS surface (n-ODC) and the p-doped indium-rich absorber (p-CIGS) [20].

Table IV.1 presents a summary of the input parameters for all layers in the structure. These parameters were taken from other research work [21,22].

Table IV.1: Physical parameters and defect state of all layers used in the simulation.

Parameter	**ZnO (n)**	**In_2Se_3 (n)**	**ODC (n)**	**CIGS (p)**
Thickness *w* (µm)	0.1	0.05	0.1 *	2.9
Band gap energy E_g (eV)	3.3	2.4	1.3	1.16
Doping density N_D/N_A (cm^{-3})	1×10^{19}	1×10^{18}	1×10^{15}*	2×10^{16}
Electron affinity χe (eV)	4.6	4.2	4	4.5
Relative permittivity ε_r ($F.cm^{-1}$)	9	10	11.9	13.6
Density of states at conduction band N_C (cm^{-3})	2.2×10^{18}	2.2×10^{18}	10^{19}	2.2×10^{18}
Density of states at valence band N_V (cm^{-3})	1.8×10^{19}	1.8×10^{19}	10^{19}	1.8×10^{19}
Electron mobility µn (cm^2/Vs)	100	100	50	100
Hole mobility µp (cm^2/Vs)	25	25	5	25
defect density N_t (cm^{-3})	10^{14} (A)	10^{14} (A)	10^{14} (D) *	10^{14} (D)
Defect energy position E_A, E_D (eV)	mid-gap▪	mid-gap▪	mid-gap▪	mid-gap
Standard energy deviation W_A, W_D (eV)	0.1(A)	0.1(A)	0.1(D)	0.1(D)
Electron capture cross section σ_n (cm^2)	10^{-12}	10^{-17}	10^{-12}	10^{-13}
Hole capture cross section σ_p (cm^2)	10^{-15}	10^{-12}	10^{-14}	10^{-15}
Surface recombination velocity for electrons S_n and holes S_p ($cm.s^{-1}$)				
at front contact		10^7	10^7	
at CdS/CIGS interface		10^5	10^5	
at back contact		10^7	10^7	

▪ mid-gap is the middle of the band gap **(A) denote Acceptor defects**
*** Variable field** **(D) denote Donor defects**

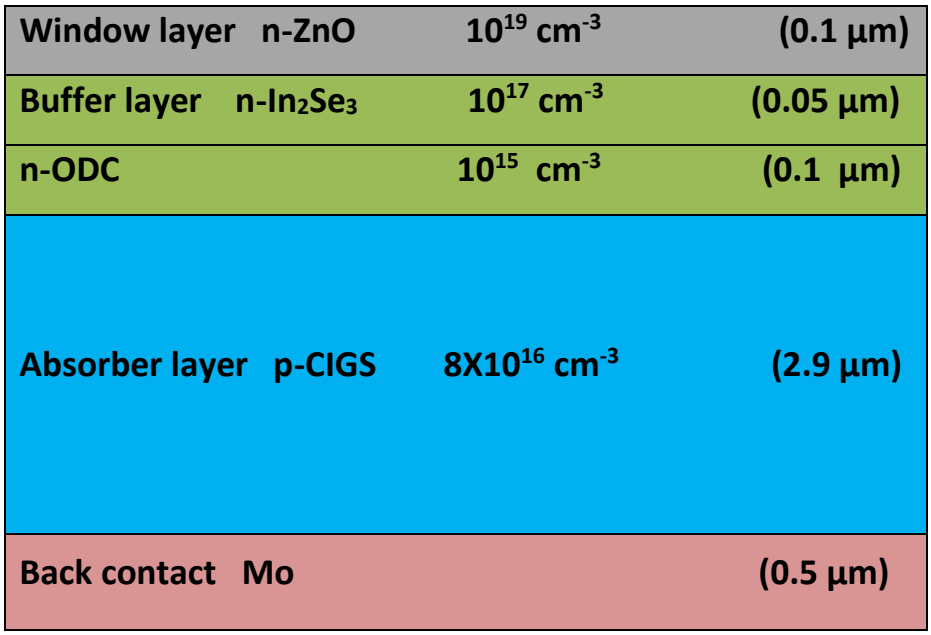

Fig. IV. 2: Schematic cross section of CIGS solar cell structure.

IV.3.1. Impact of thickness and defect density of ODC Layer

We present the findings of our numerical simulation study that aimed to investigate the impact of the ordered defect compound (ODC) layer on the performance of CIGS solar cells. We varied the thickness and defect density of the ODC layer under baseline conditions. By changing both parameters simultaneously, we were able to isolate the effect of each parameter on CIGS solar cell performance. The cell performance is: fill factor *FF*, open-circuit voltage V_{oc}, efficiency η and short circuit current density J_{sc}. The contour plot illustrated in Fig. IV.3 presents the variation of both the thickness and defect density of ODC layer versus the CIGS solar cell performance. The thickness and the defect density of ODC layer were varied from 10 nm to 100 nm and from 1×10^{10} cm^{-3} to 1×10^{19} cm^{-3}, respectively. Increasing of ODC layer thickness can lead a decrease in all photovoltaic parameters with higher defect density. Additionally, higher defect density has significant negative impact on device performance at thinner ODC layer thicknesses. A good cell performance was obtained for both lower ODC thickness and defect density, typically lower than 30 nm and 1×10^{17} cm^{-3}, respectively.

As a result, this results emphasize the importance of optimizing both the thickness and defect density of the ODC layer to achieve a best possible CIGS solar cell performance. In the other word, this study highlights the formation of ODC layer in the solar cell structure as a promising strategy to improve the efficiency of CIGS solar cell.

Future investigations could explore the impact of additional device parameters on the performance of CIGS solar cells with ODC layers and provide valuable insights into the practical implementation of ODC layer into solar cell structure.

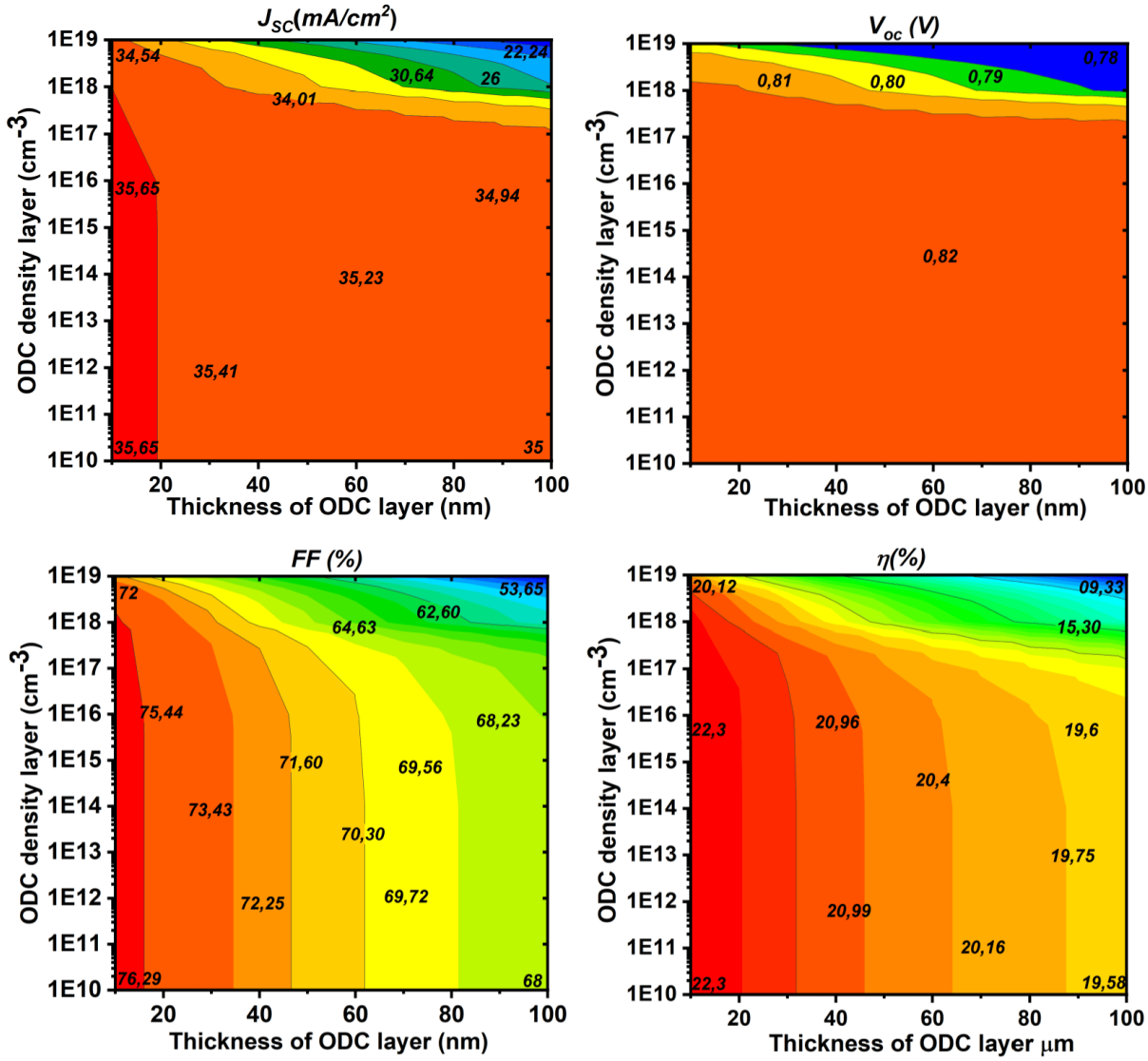

Fig. IV. 3: Evolution of photovoltaic parameters of CIGS solar cell according to the thickness and defect density of ODC layer.

IV.3.2. Impact of ODC layer thickness and ODC/In_2Se_3 interface defect density

In this section, we aimed to investigate the influence of ODC layer thickness and ODC/In_2Se_3 interface defect density on the performance of CIGS solar cell. We conducted some simulations by varying the thickness and defect density of ODC/In_2Se_3 interface to analyze the photovoltaic parameters of CIGS solar cells. By systematically varying the thickness of ODC layer from 10 nm to 100 nm and the ODC/In_2Se_3 interface defect density from 1×10^{10} cm^{-2} to 1×10^{19} cm^{-2}, we were able to isolate the effects of each parameter on CIGS solar cell performance. The results are presented in Fig. IV. 4 as a contour plot. This curve provides valuable insights into the optimal values ODC layer thickness and ODC/In_2Se_3 interface defect density to achieve maximum performance.

As indicated the Fig. IV.4, an increase in both ODC thickness and ODC/In_2Se_3 interface defect density leads a decrease in open-circuit voltage, efficiency, Fill Factor and short-circuit current density, across the entire range of input parameters. Notably, at the lowest values (10 nm and 1×10^{10} cm^{-2}), the minimum voltage was 0.83 V, short-circuit current density was 37.38 mA/cm^2 and the conversion efficiency of about 24.93%. Conversely, at the highest values (100 nm and 1×10^{19} cm^{-2}), the minimum voltage is 0.81 V, short-circuit current density was 32.52 mA/cm^2, and the efficiency decreased to 17.65%. The fill factor is directly influenced by the interface defect density, which is decreased across the entire range of ODC thickness at any given value of interface defect density. This is due to the fact that the transport of carriers across the ODC/In_2Se_3 interface is highly influenced by the presence of band discontinuities and interface defects. Such barriers can restrict the flow of current and cause a considerable reduction in *FF* [23].

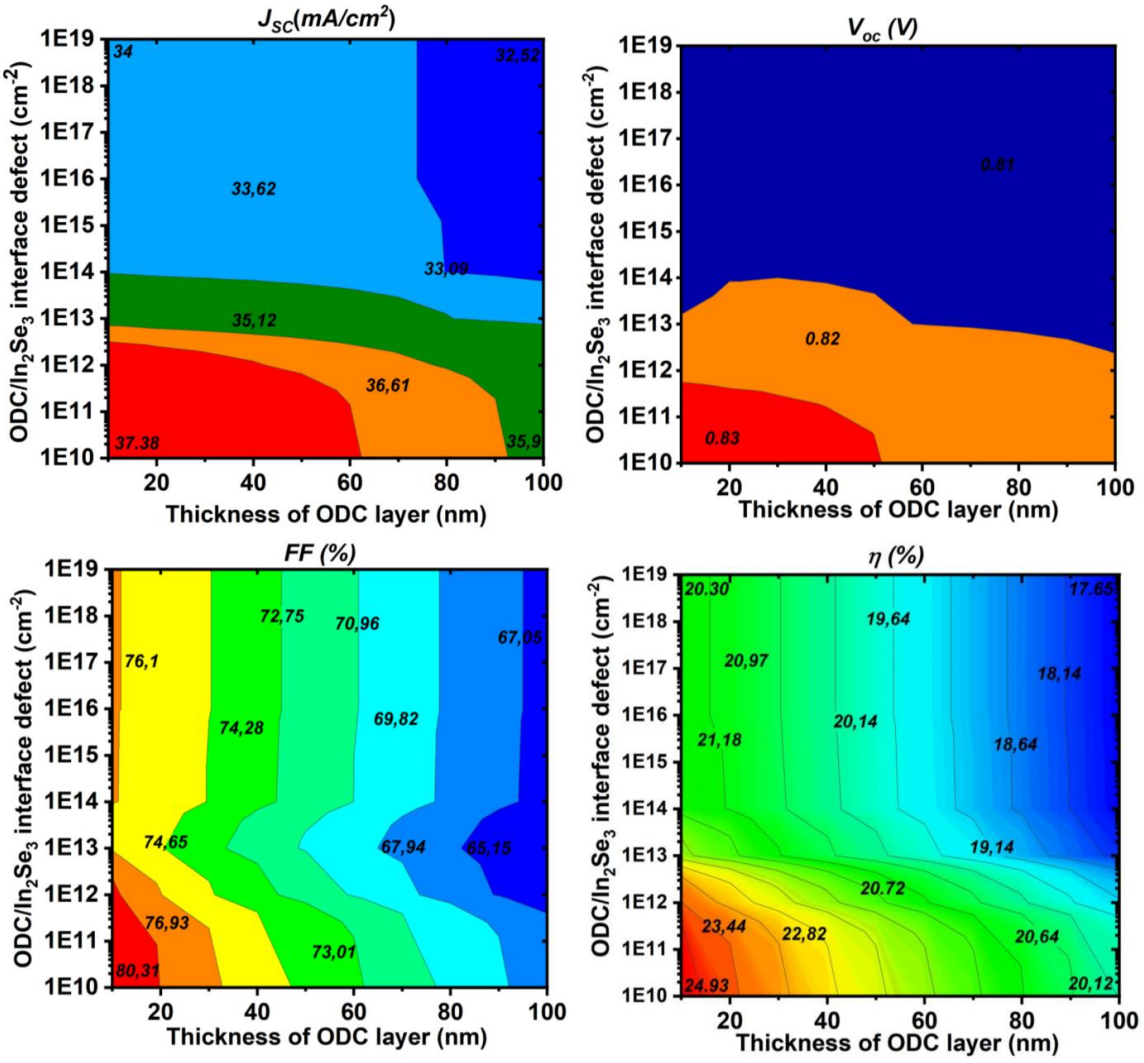

Fig. IV.4: Contour plot analysis of the effect of ODC layer thickness and ODC/In_2Se_3 interface defect density on the photovoltaic parameters of CIGS solar cells.

IV.4. Effect of activation energy levels in $CuInSe_2$ solar cell

In semiconductor materials, there can be crystal flaws due to the presence of impurities in the substrate or dangling bonds at interfaces. These crystal flaws, or traps, can greatly impact the electrical properties of the device. These traps are located within band-gap and can transfer charge with the conduction and valence bands by emitting and recombining electrons. As a result, these trap centers can change the density of space charge within the bulk of the semiconductor and have an effect on the recombination statistics [24].

A trap of the donor-type can exist in either a positive or neutral state, similar to the donor itself. On the other hand, a trap of the acceptor-type can exist in either a negative or neutral state, similar to the acceptor. When empty, a donor-like trap is positively charged or ionized, but becomes neutral when filled with an electron. An empty donor-type trap with a positive charge can capture an electron or emit a hole, while a filled trap with a neutral charge can emit an electron or capture a hole. In contrast, an acceptor-like trap is neutral when empty but becomes negatively charged or ionized when filled with an electron. A filled acceptor-like trap can emit an electron or capture a hole, whereas an empty acceptor-like trap can capture an electron or emit a hole. Donor-like traps are generally located near the valence band, while acceptor-like traps are typically situated near the conduction band [25].

In the context of CIGS, the activation energy for acceptor traps is the energy required for an electron to be liberated from the trap and become available for electrical conduction in the material. Similarly, the activation energy for donor traps is the amount of energy required for a hole to escape from the trap and participate in conduction [25]. The activation energies of acceptor and donor traps can be measured experimentally using methods such as Deep-Level Transient Spectroscopy (DLTS) [26]. The activation energy is a crucial parameter for understanding the electrical behavior of semiconductor devices and can significantly impact their electrical properties [27].

According to F.A. Abou-Elfotouh et *al.* [28], two major traps were found in the heterostructure (Cd, Zn)S/p- $CuInSe_2$ (CIS), occurring at 234 meV and 493 meV, respectively. In the Schottky diode AI/p-CIS, only one level was detected at 282 meV.

In-Hwan Choi et *al.* [29] observed that the CIGS/Al Schottky junction sample exhibited activation energies of 440 meV and 73 meV for the hole and electron traps, respectively. The capture cross-sections of the electron σ_n and the hole σ_p were measured to be 1.27×10^{14} cm^2 and 4.6×10^{19} cm^2, respectively.

The estimated value of the activation energy falls between 0.4 ± 0.6 eV, and its actual value depends on the capture cross section assumed [30].

Pran Krishna Paul's measurements in CIGS [31], indicated the presence of a mid-gap trap, which exhibits a linear variation in activation energy measured from the valence band edge with respect to the band-gap, but the activation energy remains constant when measured from the conduction band edge (E_C - 0.72 eV). Moreover, the measurements reveal the existence of another trap with a constant activation energy measured from the valence band edge (E_V + 0.98 eV) this trap is originated from the (V_{Cu} + V_{Se}) divacancy complex.

The efficiency of $CuInSe_2$ solar cells is negatively impacted by the presence of inherent point defects, such as vacancies, interstitials, and cation-cation and cation-anion antisites. To understand the impact of these defects on solar cell performance, C. Rinco et *al.* [32], conducted a study on the acceptor and donor trap levels in CIS layer. The results of their analysis indicated that the majority of the observed acceptor and donor levels were caused by the inherent point defects present in CIS layer.

The particulars of these defects and their likely origins are summarized in Table IV.2. To understand the practical implications of these traps on solar cell performance, three cases each from the hole traps (0.18, 0.4, 0.54 eV) and electron traps (0.06, 0.26, 0.57 eV) we selected and will be examined in this Chapter.

Table IV.2: Activation energies of acceptor and donor levels with the possible origin in $CuInSe_2$ layer [32].

E_A (meV)	Possible origin	E_D (meV)	Possible origin
10 - 50	V_{cu}^{-}	0-5	Se_{cu}^{+}
80 - 90	Se_i^{-}	0-10	V_{se}^{+} (or I_{cu}^{+})
160 - 180	Se_i^{--}	10-20	V_{se}^{++} (or I_{cu}^{++})
110 - 130	V_{In}^{-}	55-60	Cu_{In}^{+}
250 - 280	V_{In}^{--}	80-90	In_{se}^{+}
390 - 400	V_{In}^{---}	120-160	In_{cu}^{+} (or V_{se}^{+})
520 - 540	?	230-260	In_{cu}^{++} (or V_{se}^{++})
		160-180	In_i^{+}
		340-350	In_i^{++}
		570	In_i^{+++}

A schematic view of the conventional ZnO/CdS/$CuInSe_2$/Mo solar cell structure used in this study is displayed in Fig. IV.5. The Table IV.3 summarizes the input parameters for each layer in the proposed structure [33-35].

Table IV.3: Input parameters of each layer in the proposed structure.

Parameter	**ZnO(n)**	**CdS(n)**	**CIS(p)**
Thickness *w* (µm)	0.1	0.05	3
Band gap energy Eg (eV)	3.3	2.4	1.02
Doping density N_D/N_A (cm^{-3})	1×10^{19}	1×10^{18}	2×10^{16}
Electron affinity χe (eV)	4.6	4.2	4.5
Relative permittivity ε_r ($F.cm^{-1}$)	9	10	13.6
Density of states at conduction band N_C (cm^{-3})	2.2×10^{18}	2.2×10^{18}	2.2×10^{18}
Density of states at valence band N_V (cm^{-3})	1.8×10^{19}	1.8×10^{19}	1.8×10^{19}
Electron mobility µn (cm^2/Vs)	100	100	100
Hole mobility µp (cm^2/Vs)	25	25	25
Trap defect density N_t (cm^{-3})	10^{14} (A)	10^{14} (A)	10^{14} (A)/(D)*
Defect energy position E_A, E_D (eV)	mid-gap▪	mid-gap▪	*
Electron capture cross section σ_n (cm^2)	10^{-12}	10^{-17}	10^{-13}
Hole capture cross section σ_p (cm^2)	10^{-15}	10^{-12}	10^{-15}
Surface recombination velocity for electrons S_n and holes S_p ($cm.s^{-1}$)			
at front contact		10^7	10^7
at CdS/CIGS interface		10^5	10^5
at back contact		10^7	10^7

▪ mid-gap is the middle of the band gap **(A) denote Acceptor defects**
*** Variable field** **(D) denote Donor defects**

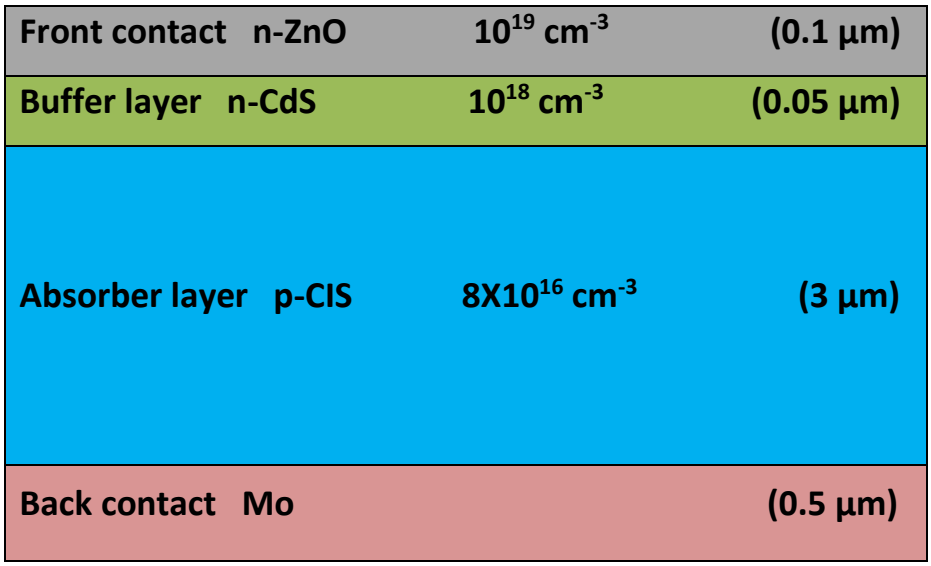

Fig. IV.5: Schematic view of $CuInSe_2$ solar cell structure.

IV.5. Effect of acceptor trap states on J-V characteristics

Fig. IV.6 displays the J-V characteristics of $CuInSe_2$ solar cell illuminated under AM1.5 and T = 300 K, representing three acceptor trap energy levels in $CuInSe_2$ absorber layer. These trap levels are denoted as E_A for all of them. These trap levels have been identified and assigned to the Selenium interstitial (Se_i) for the first trap level with E_A of 0.18 eV, the Indium vacancy (V_{In}) for E_A of 0.4 eV. However, the origin of the last activation energy, equal to 0.54 eV, was undefined.

In more detail, assuming a trap concentration in the limit of 10^{15} cm^3, considering the shallow trap level which is located at 0.18 eV from the valence-band edge E_V (E_V + 0.18 eV), then the less deep trap level (E_V + 0.4 eV) and the deep trap level (E_V + 0.54 eV) [32]. The simulation of J-V characteristics in the presence of all trap levels and without the tap levels are presented in Fig IV.6.

When the three cases of acceptor trap energy levels are considered, the J-V characteristics undergo a reduction before the cutoff point are reached, especially in the case of the deepest levels. This decrease in J-V characteristics can mainly be attributed to a decrease in the majority carrier as the trap level becomes deeper. It is worth noting that the solar cell without any trap level exhibited better J-V characteristics than those with the acceptor trap levels.

IV.5.1. Effect of acceptor trap (E_V + 0.54 eV) on cell performance

This section focuses on simulating the impact of an acceptor trap level situated at 0.54 eV above the valence band edge (E_V + 0.54 eV) on cell performance. To achieve this, we varied the trap concentration $N_{tA}(0.54)$ between 10^{13} cm^{-3} - 10^{19} cm^{-3} under AM1.5 light intensity and at T = 300 K. The results obtained from these simulations have been presented in Fig. IV. 7.

When $N_{tA}(0.54)$ exceeds 10^{15} cm^{-3}, the cell's performance is negatively impacted, as shown in the Fig. IV. 7. This leads a decrease in all photovoltaic parameters such as *Voc*, *Jsc*, *FF* and η. The reason for this decline is that the charge carriers are trapped or recombined in this defects, resulting in a loss of energy that cannot be utilized for the transportation of current to the external load. On the other hand, when $N_{tA}(0.54)$ is equal to 10^{14} cm^{-3}, the highest achievable values of photovoltaic parameters were observed, then in $N_{tA}(0.54) = 10^{14}$ cm^{-3}, the maximum values of *Jsc* = 32.41 mA/cm^2, *Voc* = 0.55 eV, *FF* = 79.8%, and η = 16.18% were achieved. Conversely, the J-V characteristics were reduced due to an increase in defect concentration to around 10^{19} cm^{-3}, resulting in lower values of *Jsc* = 5.2 mA/cm^2, *Voc* = 0.3 V, *FF* = 54.5% and η = 0.9%.

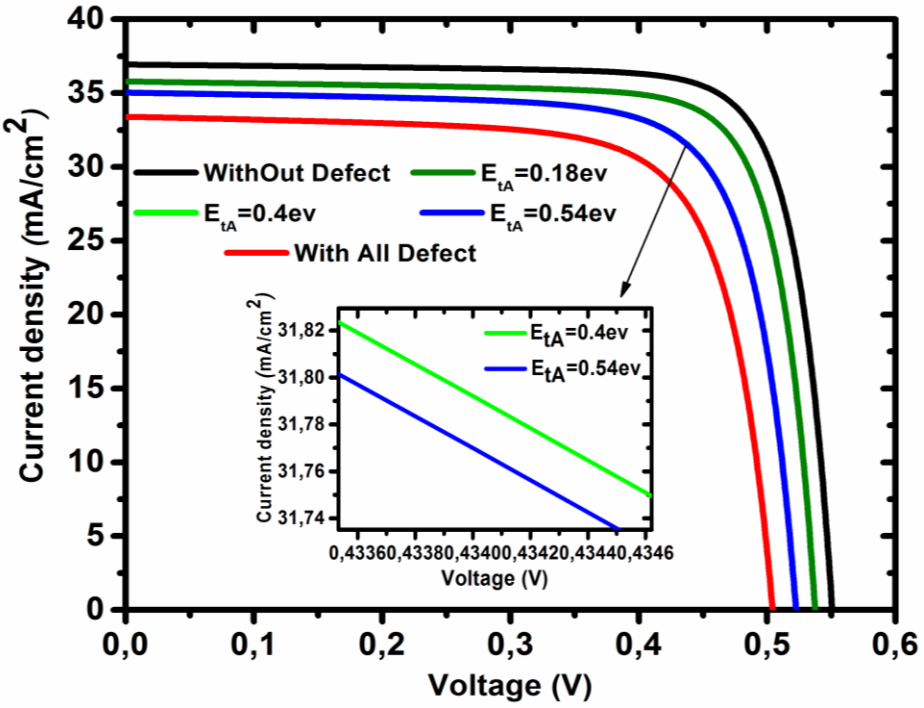

Fig. IV. 6: *J-V* characteristics for $CuInSe_2$ solar cell with different acceptor trap energy levels.

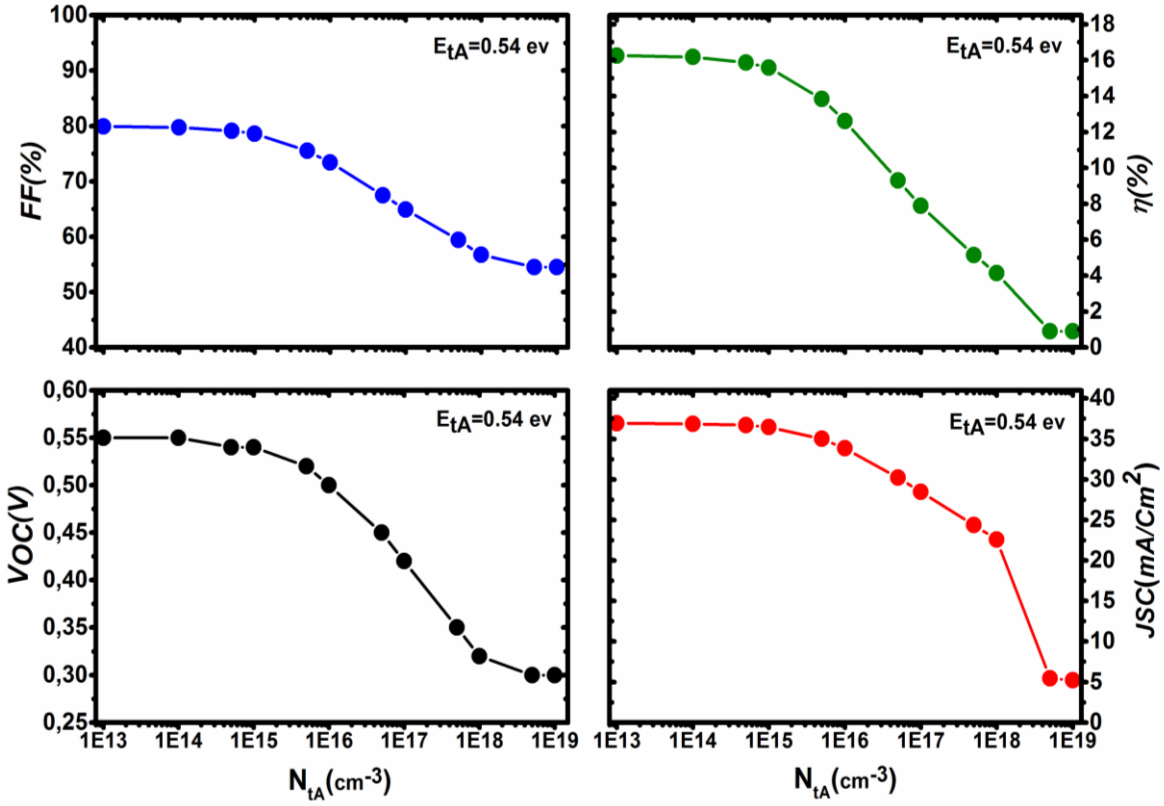

Fig. IV. 7: Effect of acceptor trap concentration on cell performance with activation energy of 0.54 eV.

IV.5.2. Effect of acceptor trap density at (E_V + 0.54 eV) on Quantum efficiency

Fig. IV.8 depicts the quantum efficiency QE for different defect state densities positioned within the CIS bulk band-gap $N_{tA}(0.54)$. Notably, the plot shows a positive QE in the short and visible wavelength range, which is distinct from the rest of the spectra. Additionally, as the density of defect states increases, there is a corresponding rise in QE, which ultimately saturates. These findings indicate that the density of defect states plays a critical role in the performance of CIS-based solar cells, particularly in the short and visible wavelength range. The observed saturation effect suggests that there exists an optimal density of defect states that maximizes the QE, which could be a significant factor to consider in optimizing the solar cell design.

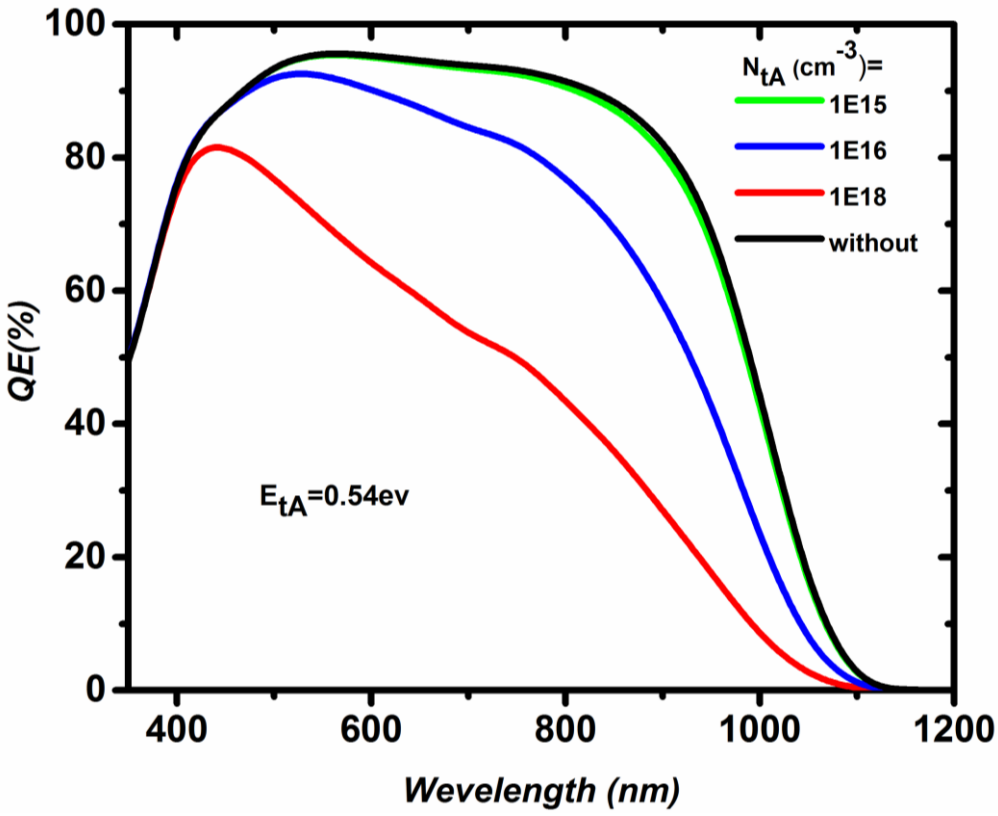

Fig. IV.8: Quantum efficiency of CIS cell structure with different trap density at E_{tA}=0.54 eV.

IV.6. Effect of donor trap states on J-V characteristics

Fig. IV.9, shows the J-V characteristics for three donor trap energy levels in $CuInSe_2$ absorber layer, labeled E_{tD} for all trap levels, when illuminated under AM1.5 and T = 300 K. These trap levels have been identified as Copper interstitial (Cu_i) for the first trap level with an E_{tD} of 0.06 eV, donor Indium atom in the Copper site (In_{Cu}) or Selenium-vacancy (V_{Se}) for E_{tD} of 0.26 eV, and Indium interstitial (In_i) for the origin of the last activation energy, which is equal to 0.57 eV.

We analyzed the J-V characteristics of the $CuInSe_2$ solar cell by considering trap concentrations up to 10^{15} cm^{-3}. Specifically, we examined three trap levels: a shallow trap level located at 0.06 eV from the bottom of the conduction band edge E_C (E_C - 0.06 eV), a less deep trap level (E_C - 0.26 eV), and a deep trap level (E_C - 0.57 eV) [32]. The impact of the presence and absence of all three trap levels on the J-V characteristics were presented in Fig. IV.9.

Upon evaluating the three scenarios of acceptor trap energy levels, a decline in the J-V characteristics is observed, specifically for the most profound levels. As the energy level of a trap becomes deeper, the probability of electrons being released and reaching the conduction band edge decreases, making it increasingly difficult for them to contribute to the electrical conductivity of $CuInSe_2$ solar cell.

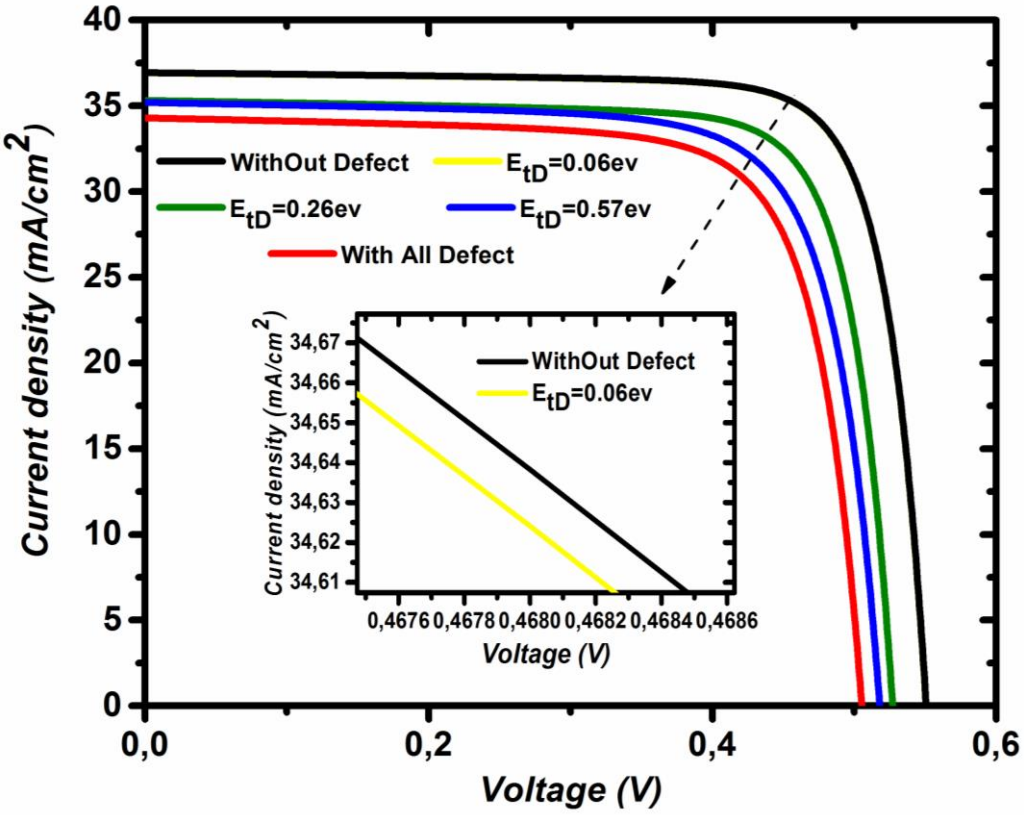

Fig. IV. 9: J-V characteristics of $CuInSe_2$ solar cell with different donor trap energy levels.

IV.6.1. Effect of donor trap (E_C - 0.57 eV) on the cell performance

The purpose of this section is to simulate how a donor trap level positioned at the bottom of the conduction band edge (E_C - 0.57 eV) at 0.57 eV affects the cell performance. The simulations were carried out by adjusting the trap concentration $N_{tD}(0.57)$ between 10^{13} cm^{-3} - 10^{17} cm^{-3}, with T = 300 K and under an AM1.5 light intensity. The simulation results are

illustrated in Fig. IV.10. This figure shows that exceeding 10^{15} cm^{-3} for N_{tD} (0.57) has a detrimental effect on the solar cell performance. This results in a decline in photovoltaic parameters such as *Voc*, *Jsc*, *FF*, and η due to the trapping or recombination of charge carriers in defects, resulting in energy loss that cannot be utilized for current transportation to the external load. In contrast, the highest achievable photovoltaic parameters were observed at N_{tD} (0.57) = 10^{13} cm^{-3}. The maximum values of *Jsc* = 36.92 mA/cm^2, *Voc* = 0.55 eV, *FF* = 79.92%, and η = 16.26% were obtained at N_{tD} (0.57)= 10^{14} cm^{-3}. However, an increase in the defect concentration to approximately 10^{17} cm^{-3} resulted in a reduction in J-V characteristics, leading to lower values of *Jsc* = 1.28 mA/cm^2, *Voc* = 0.16 V, *FF* = 37% and η = 0.07%.

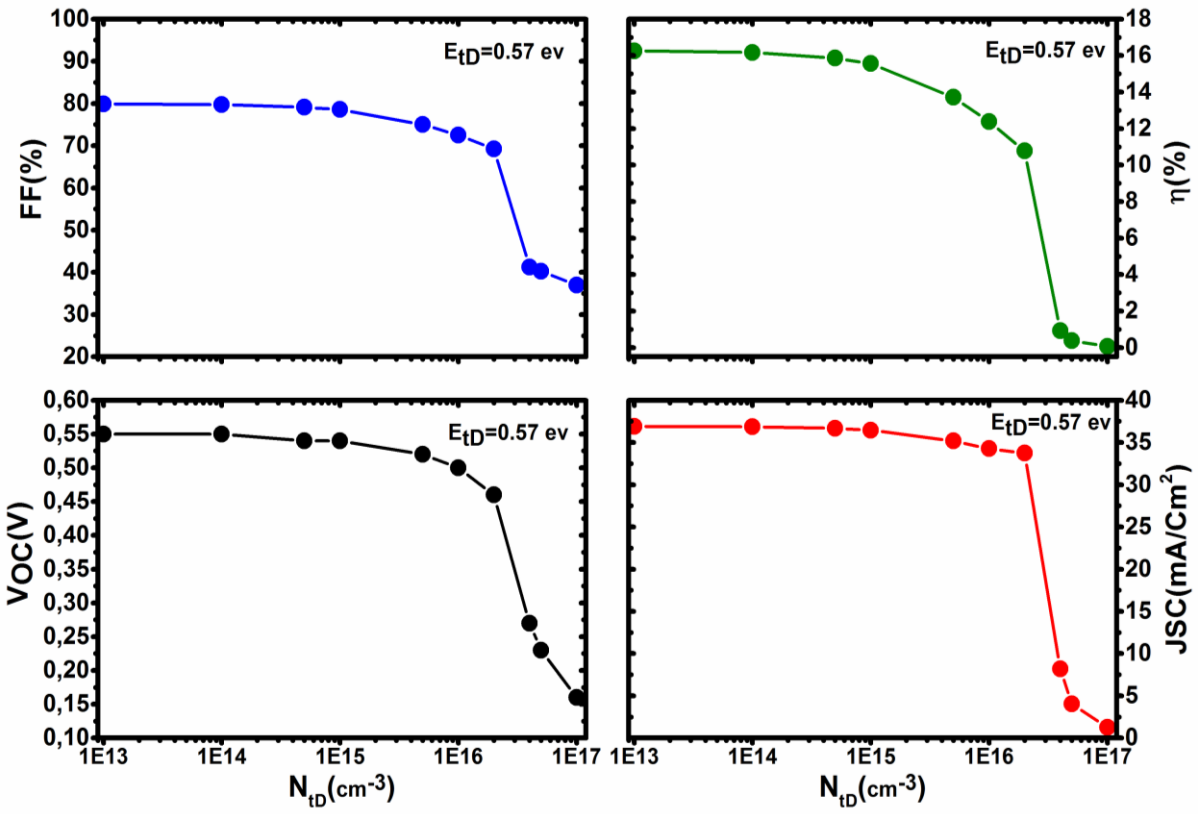

Fig. IV. 10: Effect of donor trap concentration on the cell performance with activation energy of 0.57 eV.

IV.6.2. Effect of donor trap (E_C - 0.57 eV) on quantum efficiency

In Fig. IV. 11, we have observed that the trap concentrations below 10^{15} cm^{-3} do not affect the quantum efficiency QE. As the concentration of traps increases beyond this threshold, there is a decrease in the quantum efficiency QE at the level of visible waves. Additionally, we have noticed a significant collapse and reduction in QE at trap concentrations exceeding 3×10^{16} cm^{-}

^{3}, which corresponds to the concentration of the CIS layer, with the exception of the wave at 1000 nm.

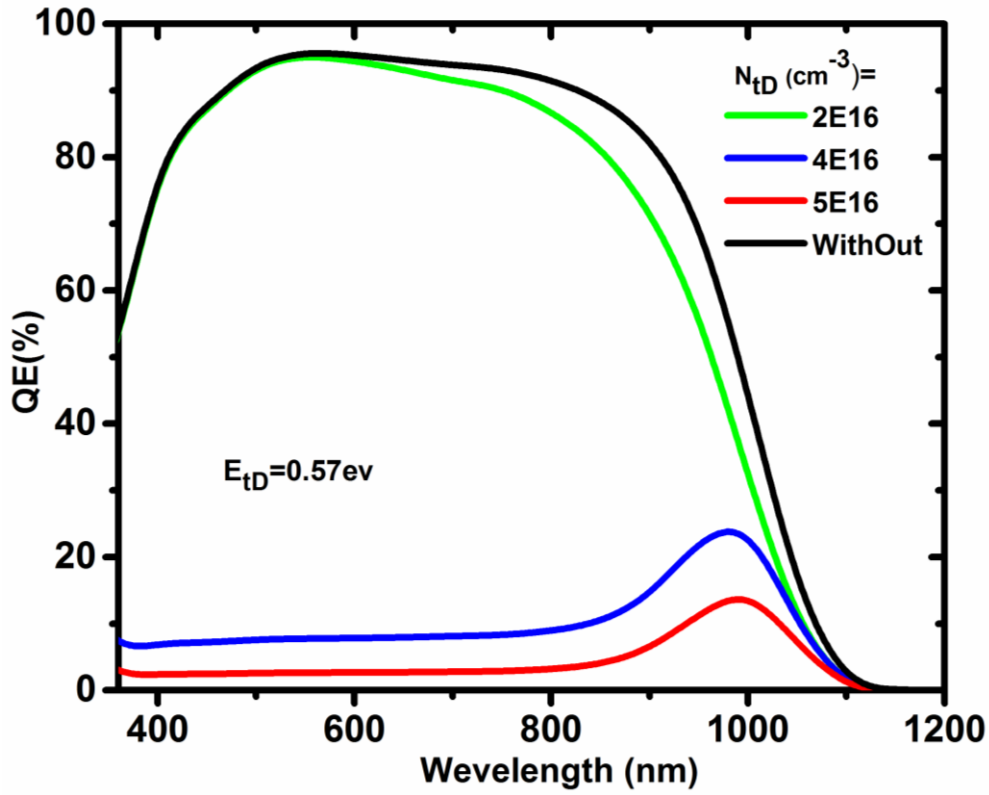

Fig. IV.11: Quantum efficiency of CIS cell structure with different donor trap density at 0.57 eV.

IV.7. Conclusion

To summarize, we used the SILVACO/Atlas simulator to investigate the behavior of CIGS/In_2Se_3/ZnO and CIGS/CdS/ZnO solar cells in two different cases. In the first section, we examined how the Ordered Defect Compound layer (ODC) affected the performance of CIGS solar cells. Our simulation results revealed that the presence of ODC defects had a negative impact on the efficiency of the solar cell, as evidenced by a decrease in the J-V characteristics. Therefore, it is important to minimize the ODC layer defects and/or ODC layer thickness to improve the efficiency of CIGS solar cells.

The second simulation focused on the variation of the activation energy levels in $CuInSe_2$ absorber layer that affects the solar cell performance. Our results showed that the activation energy levels for donor and acceptor types significantly influenced the electrical properties of the solar cell.

Finally, our simulations provide valuable insights into the factors that affect the performance of solar cells. By identifying specific parameters such as ODC layer defects and activation energy levels that impact the solar cell performance. This research can aid in the development of more efficient and cost-effective CIGS solar cells.

References

[1] Gall, S., Barreau, N., Harel, S., Bernède, J. C., and Kessler, J. (2005). Material analysis of PVD-grown indium sulphide buffer layers for Cu(In,Ga)Se_2-based solar cells. Thin Solid Films, 480-481, 138-141. doi:10.1016/j.tsf.2004.11.017.

[2] Djessas, K., Abatchou, A., and Massé, G. (2000). Diffusions in (In,Se)-Cu(In,Ga)Se_2/SnO_2 thin film structures. Journal of Applied Physics, 88(10), 5710-5715. doi:10.1063/1.1320005.

[3] Massé, G., and Djessas, K. (2003). p-n junctions in (In,Se)/Cu(In,Ga)$(Se,S)_2$ photovoltaic systems. Journal of Applied Physics, 94(10), 6985-6987. doi:10.1063/1.1621715.

[4] Djessas, K., Yapi, S., Massé, G., Ibannain, M., and Gauffier, J. L. (2004). Diffusion of Cu, In, and Ga in In_2Se_3/$CuGaSe_2$/SnO_2 thin film photovoltaic structures. Journal of Applied Physics, 95(8), 4111-4116. doi:10.1063/1.1652252.

[5] Kwon, S. H., Ahn, B. T., Kim, S. K., Yoon, K. H., and Song, J. (1998). Growth of $CuIn_3Se_5$ layer on $CuInSe_2$ films and its effect on the photovoltaic properties of In_2Se_3/$CuInSe_2$ solar cells. Thin Solid Films, 323(1-2), 265-269. doi:10.1016/s0040-6090(97)00928-0.

[6] Zhang, S. B., Wei, S.-H., Zunger, A., and Katayama-Yoshida, H. (1998). Defect physics of the $CuInSe_2$ chalcopyrite semiconductor. Physical Review B, 57(16), 9642-9656. doi:10.1103/physrevb.57.9642.

[7] Zhang, S. B., Wei, S.H., and Zunger, A. (1997). Stabilization of Ternary Compounds via Ordered Arrays of Defect Pairs. Physical Review Letters, 78(21), 4059-4062. doi:10.1103/physrevlett.78.4059.

[8] Wei, S., and Zunger, A. (1995). Band offsets and optical bowings of chalcopyrites and Zn-based II-VI alloys. Journal of Applied Physics, 78(6), 3846-3856. doi:10.1063/1.359901.

[9] Bouchama, I., Zouache, R., Djessas, K., Bouloufa, A., and Ghribi, F. (2015). Size and grain-boundary effects on the performance of polycrystalline CIGS-based solar cells. IREC2015 The Sixth International Renewable Energy Congress. doi:10.1109/irec.2015.7110920.

[10] Malm, U., and Edoff, M. (2009). 2D device modelling and finite element simulations for thin-film solar cells. Solar Energy Materials and Solar Cells, 93(6-7), 1066-1069. doi:10.1016/j.solmat.2008.11.058.

[11] Chelvanathan, P., Hossain, M. I., and Amin, N. (2010). Performance analysis of copper-indium–gallium–diselenide (CIGS) solar cells with various buffer layers by SCAPS. Current Applied Physics, 10(3), S387-S391. doi:10.1016/j.cap.2010.02.018.

[12] Pudov, A. O., Kanevce, A., Al-Thani, H. A., Sites, J. R., Hasoon, F. S. (2005). Secondary barriers in CdS-$CuIn_{1-x}Ga_xSe_2$ solar cells. Journal of Applied Physics, 97(6), 064901. doi:10.1063/1.1850604.

[13] T. Nakada, Y. Kanda, S. Kijima, Y. Komiya, D. Ohmori, H. Ishizaki, and N. Yamada. (2005). Bifacial CIGS thin film solar cells, 20th European Photovoltaic Solar Energy Conference, Barcelona, Spain, pp.1736-1739.

[14] H. Simchi, Back surface studies of Cu(In,Ga)Se_2 thin film solar cells, PhD Thesis, (2014). University of Delaware.

[15] Yan, Y., Jones, K. M., Abushama, J., Young, M., Asher, S., Al-Jassim, M. M., and Noufi, R. (2002). Microstructure of surface layers in Cu(In,Ga)Se_2 thin films. Applied Physics Letters, 81(6), 1008-1010. doi:10.1063/1.1498499.

[16] Lee, S. M., Ikeda, S., Otsuka, Y., Septina, W., Harada, T., and Matsumura, M. (2012). Homogeneous electrochemical deposition of in on a Cu-covered Mo substrate for fabrication of efficient solar cells with a $CuInS_2$ photoabsorber. Electrochimica Acta, 79, 189–196. doi:10.1016/j.electacta.2012.06.1.

[17] Schmid, D., Ruckh, M., Grunwald, F., and Schock, H. W. (1993). Chalcopyrite/defect chalcopyrite heterojunctions on the basis of $CuInSe_2$. Journal of Applied Physics, 73(6), 2902-2909. doi:10.1063/1.353020.

[18] Gloeckler, M., Sites, J. R., and Metzger, W. K. (2005). Grain-boundary recombination in Cu(In,Ga)Se_2 solar cells. Journal of Applied Physics, 98(11), 113704. doi:10.1063/1.2133906.

[19] Nakada, T., Kume, T., Mise, T., and Kunioka, A. (1998). Superstrate-Type Cu(In, Ga)Se_2 Thin Film Solar Cells with ZnO Buffer Layers. Japanese Journal of Applied Physics, 37 (Part 2, No. 5A), L499-L501. doi:10.1143/jjap.37.l499.

[20] Lee, D. Y., Yun, J. H., Yoon, K. H., and Ahn, B. T. (2002). Characterization of Cu-poor surface on Cu-rich $CuInSe_2$ film prepared by evaporating binary selenide compounds and its effect on solar efficiency. Thin Solid Films, 410(1-2), 171-176. doi:10.1016/s0040-6090(02)00249-3.

[21] Bouchama, I., Boudour, S., Bouarissa, N., and Rouabah, Z. (2017). Quantum and conversion efficiencies optimization of superstrate CIGS thin-films solar cells using In_2Se_3 buffer layer. Optical Materials, 72, 177-182. doi:10.1016/j.optmat.2017.05.056.

[22] Mouhoub, A., Bouloufa, A., Djessas, K., and Messous, A. (2020). Device modeling approach and simulation of the effect of the ODC thin layer on bifacial solar cells based on $CuIn_{1-x}Ga_xSe_2$ thin films absorbers. Journal of Physics and Chemistry of Solids, 109520. doi:10.1016/j.jpcs.2020.109520.

[23] Bouchama, I., Djessas, K., Djahli, F., and Bouloufa, A. (2011). Simulation approach for studying the performances of original superstrate CIGS thin films solar cells. Thin Solid Films, 519(21), 7280-7283. doi:10.1016/j.tsf.2011.01.182.

[24] Trimpl, M. J., Wright, A. D., Schutt, K., Buizza, L. R. V., Wang, Z., Johnston, M. B., Herz, L. M. (2020). Charge-Carrier Trapping and Radiative Recombination in Metal Halide Perovskite Semiconductors. Advanced Functional Materials, 2004312. doi:10.1002/adfm.202004312.

[25] Bouzid, F. (2018). Simulation des propriétés électriques d'une jonction à base de nitrure de gallium. Application au détecteur de rayonnement. Thèse de doctorat. Université Mohamed Khider -Biskra. Algerie.

[26] Eric C. Larkins, James S. HarrisJr., in Molecular Beam Epitaxy: Applications to Key Materials, (1995).

[27] Bouzid, F., Dehimi, L., Pezzimenti, F. (2017). Performance Analysis of a Pt/n-GaN Schottky Barrier UV Detector. Journal of Electronic Materials, 46(11), 6563-6570. doi:10.1007/s11664-017-5696-1.

[28] Abou-Elfotouh, F. A., Moutinho, H., Bakry, A., Coutts, T. J., and Kazmerski, L. L. (1991). Characterization of the defect levels in copper indium diselenide. Solar Cells, 30(1-4), 151–160. doi:10.1016/0379-6787(91)90048-t.

[29] Choi, I.-H., Choi, C.-H., and Lee, J.-W. (2012). Deep centers in a $CuInGaSe_2$/CdS/ZnO:B solar cell. Physica Status Solidi (a), 209(6), 1192-1197. doi:10.1002/pssa.201127596.

[30] Igalson, M., and Zabierowski, P. (2000). Transient capacitance spectroscopy of defect levels in CIGS devices. Thin Solid Films, 361-362, 371-377. doi:10.1016/s0040-6090(99)00822-6.

[31] Krishna Paul, P. (2019) Impact of deep traps on CIGS solar cell performance and reliability, PhD Thesis. The Ohio State University.

[32] Rincón, C., Márquez, R. (1999). Defect physics of the $CuInSe_2$ chalcopyrite semiconductor. Journal of Physics and Chemistry of Solids, 60(11), 1865-1873. doi:10.1016/s0022-3697(99)00190-0.

[33] Heriche, H., Rouabah, Z., and Bouarissa, N. (2017). New ultra-thin CIGS structure solar cells using SCAPS simulation program. International Journal of Hydrogen Energy, 42(15), 9524-9532. doi:10.1016/j.ijhydene.2017.02.09.

[34] Bouabdelli, M. W., Rogti, F., Maache, M., and Rabehi, A. (2020). Performance enhancement of CIGS thin-film solar cell. Optik, 216, 164948. doi:10.1016/j.ijleo.2020.164948.

[35] Zouache, R., Bouchama, I., Saidani, O., Djedoui, L., and Zaidi, L. (2022). Numerical study of high-efficiency CIGS solar cells by inserting a BSF μc-Si:H layer. J Comput Electron 21, 1386-1395. https://doi.org/10.1007/s10825-022-01942-5.

Chapter V: Experimental study of $Cu(In,Ga)Se_2$ thin film

Chapter V
Experimental study of Cu(In,Ga)Se_2 thin film

V.1. Introduction

Copper indium gallium selenide (CIGS) thin films are widely used in the fabrication of high-efficiency thin-film solar cells due to their excellent optical and electrical properties [1-3]. The deposition of CIGS thin films onto Metal-covered substrates or Soda-Lime Glass (SLG) substrates are commonly achieved using the physical vapor deposition technique such as Magnetron sputtering technique [4-6]. This technique is preferred due to its ability to produce high-quality films with good adhesion, uniformity, and reproducibility.

Some of the main advantages of using RF-magnetron sputtering to deposit CIGS thin films include:

- Control over film properties: RF magnetron sputtering provides a high degree of control over the deposition of CIGS thin films, allowing for precise tuning of film composition, thickness, and crystal structure. This enables optimization of the film's properties for specific photovoltaic applications.
- High-quality films: The films deposited using RF magnetron sputtering are of high quality, exhibiting excellent electrical and optical properties, such as high carrier mobility, high absorption coefficients, and low recombination rates. This results in enhanced solar cell efficiency and performance.
- Wide range of substrate materials: RF magnetron sputtering is compatible with a wide range of substrate materials, including soda-lime glass, flexible polymers, and metal foils. This allows for greater flexibility in the design and manufacture of CIGS thin-film solar cells.
- Scalability and cost-effectiveness: RF magnetron sputtering is a scalable and cost-effective technique for the deposition of CIGS thin films, making it an attractive option for large-scale commercial production of CIGS-based solar cells.

V.2. Magnetron sputtering technique

Magnetron sputtering includes many types, such as direct current (DC) magnetron sputtering and radio frequency (RF) magnetron sputtering, each has a different working principle and application objects (See Fig V.1). The main advantage of RF magnetron

sputtering over DC magnetron sputtering is that it does not require the target as an electrode be electrically conductive. Therefore, any material can be sputter-deposited theoretically using RF magnetron sputtering.

RF magnetron sputtering is a process used to deposit high quality CIGS thin films of various materials onto a large-scale substrate [7-10]. The process involves the use of a magnetron and an inert gas such as argon, which is introduced into a vacuum chamber. An RF power source is used to create an oscillating electric field in the chamber, which ionizes the gas and generates a high-density plasma. The plasma then bombards a target material placed in the chamber, causing atoms to be ejected from the surface of the target (see Fig. V.1). These ejected atoms then travel through the plasma and deposit onto a substrate placed in the vacuum chamber, forming a thin film. By controlling the power and gas flow rates, as well as the distance between the target and substrate, it is possible to control the properties of the deposited thin film, such as its thickness and composition [11-13].

In general, the principle of RF magnetron sputtering involves using a plasma generated by an RF power source to eject atoms from a target material and deposit them onto a substrate, allowing for precise control over the properties of the deposited thin film.

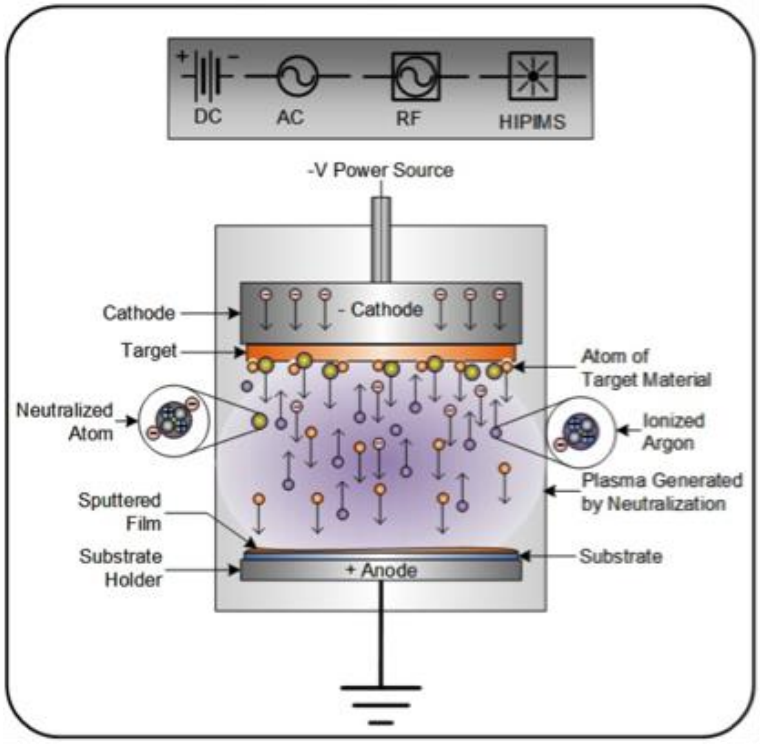

Fig.V.1: Schematic diagram of magnetron sputtering technique.

V.3. Characterization techniques

V.3.1. Structural characterization using X-ray diffraction technique

One effective tool for examining the crystallographic structures of deposited materials is the X-ray diffraction (XRD) device which is widely accessible.

In our experimental work, we utilized diffraction diagrams on thin film samples. To conduct these measurements, we employed a PANalytical X'pert PRO diffractometer, which uses the Cu-Kα wavelength and consists of an X-ray tube with a Cu anode powered by high-frequency, a goniometer with a detector, a monochromator to select the average Cu wavelength, and a computer equipped with software to control the goniometer and analyze the results. The device used in our experiments is illustrated in Fig. V.2.

Fig. V.2: Image of X-ray Diffraction (XRD) apparatus used in our work.

Fig. V.3 (a) illustrates that when a crystal is struck by X-rays of electromagnetic radiation at a specific angle (θ), the reflection intensity displays a peak and constructive interference is observed, confirming the validity of Bragg's law [14].

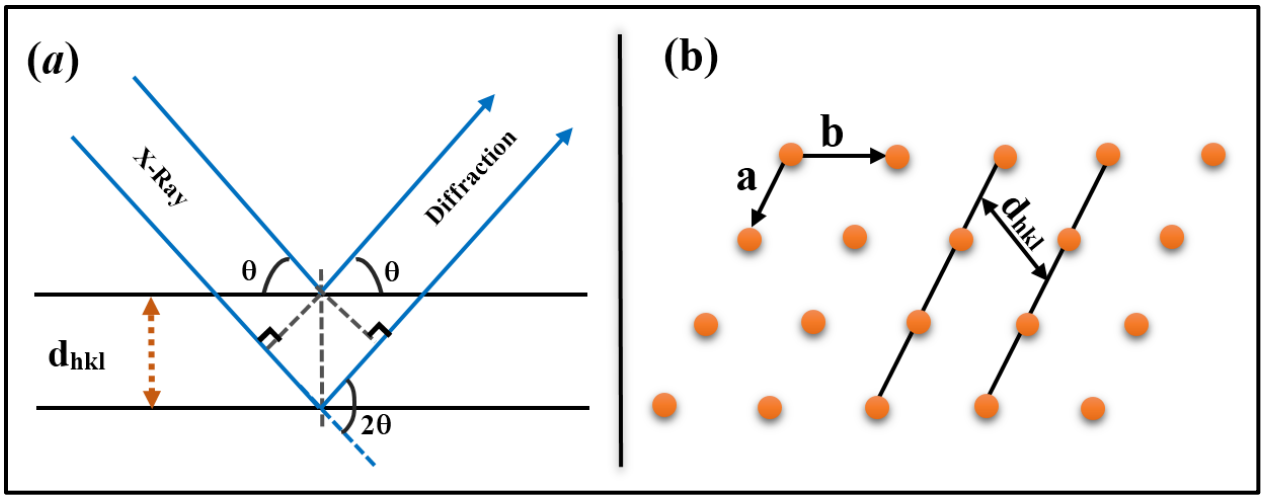

Fig. V.3: Schematic illustration of **a)** the X-ray diffraction principal and **b)** the Distance (d_{hkl}) between two reticular planes.

The relation between the distance (d_{hkl}) separating two parallel reticular planes (Fig. V.2(b)), the wavelength (λ) of X-rays, and the diffraction angle (θ) (Fig. V.2(a)) is expressed by Bragg's law in Equation (V.1) [15]:

$$2d_{hkl}sin(\theta) = n\lambda \qquad \text{(V.1)}$$

V.3.2. Lattice constant

To obtain the lattice parameters: a, b and c of a crystal with a tetragonal or cubic structure, it is possible to use the (hkl) indices and relate them to the d spacing, as follows [16]:

$$\frac{1}{(d_{hkl})^2} = \left[\frac{h^2 + k^2 + l^2}{a^2}\right] \quad (Cubic) \qquad \text{(V.2)}$$

$$\frac{1}{(d_{hkl})^2} = \left[\frac{h^2 + k^2}{a^2} + \frac{l^2}{c^2}\right] \quad (Tetragonal) \qquad \text{(V.3)}$$

In which
- d_{hkl} – inter-reticular distance,
- hkl – Miller indices,
- θ – Diffraction angle of Bragg,
- λ – Wavelength of incident radiation CuKα,
- a, c – Lattice parameters (constants) of the crystal.

In general, to calculate the values of a, b, and c from Bragg's law for Cu(In,Ga)Se_2 material, you would need to know the parameters of the crystal structure and the incident X-ray wavelength. We must follow six steps:

1. Determine the crystal structure parameters: Cu(In,Ga)Se_2 has a chalcopyrite crystal structure, which can be described using a space group notation. The lattice parameters can be obtained from X-ray diffraction (XRD) experiments or from literature sources.
2. Calculate the diffraction angle: The Bragg's law is given by $n\lambda = 2d \sin(\theta)$, where n is the order of diffraction. For a given X-ray wavelength and diffraction order, you can calculate the diffraction angle θ using the Bragg's law.
3. Calculate the interplanar spacing: From the diffraction angle θ and the lattice parameters of the crystal, you can calculate the interplanar spacing d using the Bragg's law.
4. Determine the Miller indices: The Miller indices (hkl) of the diffracted crystal planes can be determined from the interplanar spacing d using the Equation (V.2) or (V.3).
5. Identify the crystal planes: Once you have the Miller indices, you can use crystallographic databases or reference texts to identify the crystal planes that are responsible for the diffraction peaks.
6. Calculate the lattice constants: The lattice constants a, b, and c can be calculated from the Miller indices using equation (V.2) or (V.3) that relate them to the crystallographic parameters. The exact equations will depend on the crystal system and the space group of the crystal.

V.3.3. Sherrer formula

The Sherrer formula, also known as the Scherrer equation, is a mathematical formula used to estimate the average crystallite size or grain size of a crystalline material based on the full width at half maximum (FWHM) of its X-ray diffraction (XRD) peaks. It is given by:

$$D = \frac{K\lambda}{\beta \cos\theta} \quad \text{(V.4)}$$

Where:

D is the average crystallite size or grain size of the material.

K is a dimensionless shape factor, typically assumed to be around 0.9.

λ is the wavelength of the X-ray radiation used, usually in angstroms (Å).

β is the FWHM of the XRD peak, typically measured in radians.

θ is the Bragg angle at which the XRD peak is observed, typically in degrees.

The Sherrer formula assumes that the material is a homogeneous, isotropic, and randomly oriented powder with small crystallites that behave as independent scattering centers. It provides an estimate of the size of these crystallites based on the broadening of the XRD peaks due to their finite size and the X-ray diffraction effects. The Sherrer formula is widely used in materials science and engineering to study the microstructure and properties of materials, including metals, alloys, ceramics, and thin films.

V.4. Experimental details

Cu(In,Ga)Se_2 (CIGS) thin films were deposited on Mo-covered soda lime glass (SLG) substrates of 25 mm × 10 mm via Radio Frequency (RF) magnetron sputtering system. A Kurt J. Lesker 4-gun model RF-sputtering machine was used (see Fig.V.4). Special care was taken to ensure that the substrate holder was dirt-free by wiping it with ethanol-soaked lint-free wipes, because the sputtering machine was installed in a class 10 K clean room and different runs were performed to prepare CIGS samples for characterization. After each run, the sputtering machine was opened and the substrate holder was cleaned. The cleaned and dried glass was placed in the substrates inside the RF-sputtering chamber. Prior to deposition, all the substrates were cleaned ultrasonically in a methanol-acetone-methanol-deionized water sequence for a total of 60 minutes and finally dried by blowing dry N_2 gas. Source material used in this study is 99.95% for CIGS sputtering targets which was pre-sputtered for 15 minutes to remove contamination from the target surface. Deposition chamber base pressure was brought down close to 3×10^{-5} Torr by turbo molecular pump and the working pressure during all the deposition run was maintained at 10 mTorr by following 0.5 sccm of purified Argon (99.99%) as the working gas into the chamber. Substrate holder rotation speed and target to substrate distance were set to 10 rpm and 80 mm. CIGS sputtered deposition parameters such as RF power and substrate deposition temperature were fixed at 40 W (≈ 2 W/cm^2) and 300°C, respectively.

Structural and crystallinity properties as well as the deposited film orientations along the film's surface normal were examined using a PANalytical X'pert PRO diffractometer using CuKα radiation wavelength, λ = 1.5406 Å = 0.15406 nm. XRD patterns were recorded in the 2θ range from 10° to 70° with scanning rate 1 deg/min (Fig. V.2). To investigate the surface morphology, thickness, and roughness of newly prepared sample, Atomic Force Microscopy (AFM) images were captured using an MFP-3D AFM (Oxford Instruments Asylum Research) in contact mode with a Si cantilever. The height values from these AFM images were analyzed

using commercial AR software to calculate the Root Mean Square (RMS) roughness values. These measurements were obtained by employing peak force tapping mode. For the FT-IR measurements, the spectra were recorded using a Shimadzu FT-IR spectrometer in the range between 4000 and 500 cm^{-1}.

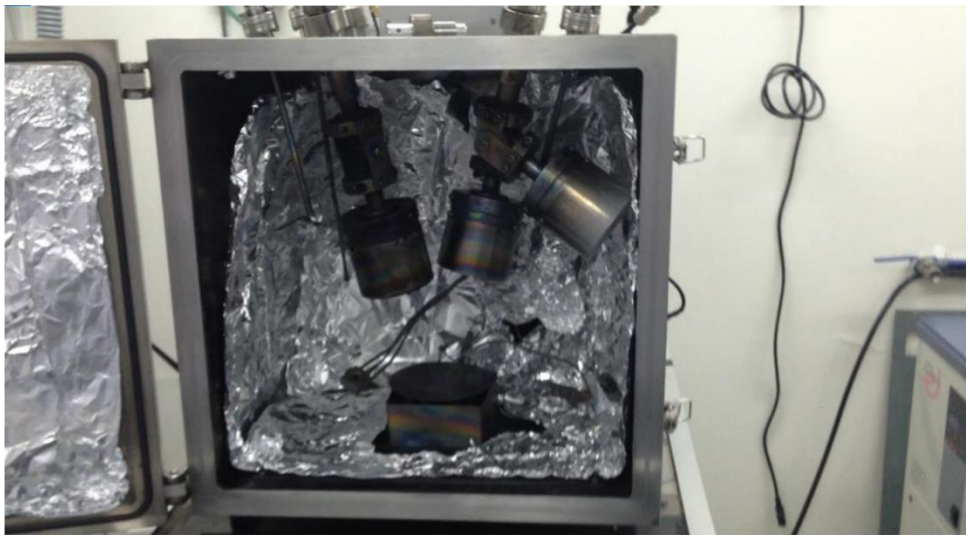

Fig.V.4: RF-magnetron sputtering system used to deposit CIGS sample.

During RF magnetron sputtering, a target made of CIGS material is bombarded with ions in a vacuum chamber, causing the atoms or ions to be ejected and deposited onto a substrate, forming a thin film. The process parameters, such as: sputtering power, deposition time, substrate temperature, and gas pressure, can be optimized to achieve the desired properties of the deposited thin film.

V.5. Results of characterization

One of the challenges in utilizing CIGS photovoltaic compounds is to produce high quality and large area CIGS films that are both cost-effective and appropriate for the application. In order to tackle this issue, a characterization study is mandatory in order to analyze the quality of deposited films.

V.5.1. Structural study by X-ray diffraction measurement

X-ray diffraction (XRD) is an important characterization technique used to analyze the crystal structure and phase composition of CIGS thin films. It can provide information about the orientation and crystallinity of the thin films, which is important for optimizing their electronic and optical properties for solar cell applications. In our case, it can be used to determine the preferred crystallographic orientation of obtain film. The presence of impurities,

defects, or secondary phases can significantly affect the electronic and optical properties of the material. By analyzing the diffraction peaks of the XRD patterns, one can identify the crystallographic phases present in the thin film and estimate their relative abundance.

The CIGS structure is a chalcopyrite-type crystal structure, which has a unique crystallographic orientation. The XRD patterns can reveal the preferred orientation of the crystal structure along a certain direction which is associated with the highest efficiency of CIGS-based solar cells.

In Fig. V.5, the XRD pattern of CIGS layer grown onto Mo/SLG at room temperature is displayed. The diffraction pattern observed is indicative of the chalcopyrite crystal structure. The film's most intense diffraction peak, which appears at around $2\theta = 26.88°$ and corresponds to the diffraction from (112) planes, shows that the films have a preferred orientation along the (112) direction, which is perpendicular to the substrate's plane. Other diffraction peak, (220), with weak intensity was also observed at $2\theta = 44.80°$. The crystallography is well-matched with the Joint Committee on Powder Diffraction Standards (JCPDS 00-035-1102) data. The intensity of the preferred orientation (112) peak for the deposited CIGS film on the Mo substrate revealed good crystallinity. Along with the XRD peaks associated with the (110) and (211) planes, which are attributed to the molybdenum (Mo) material. The study did not reveal any diffraction peaks that could not be attributed to the starting CIGS material.

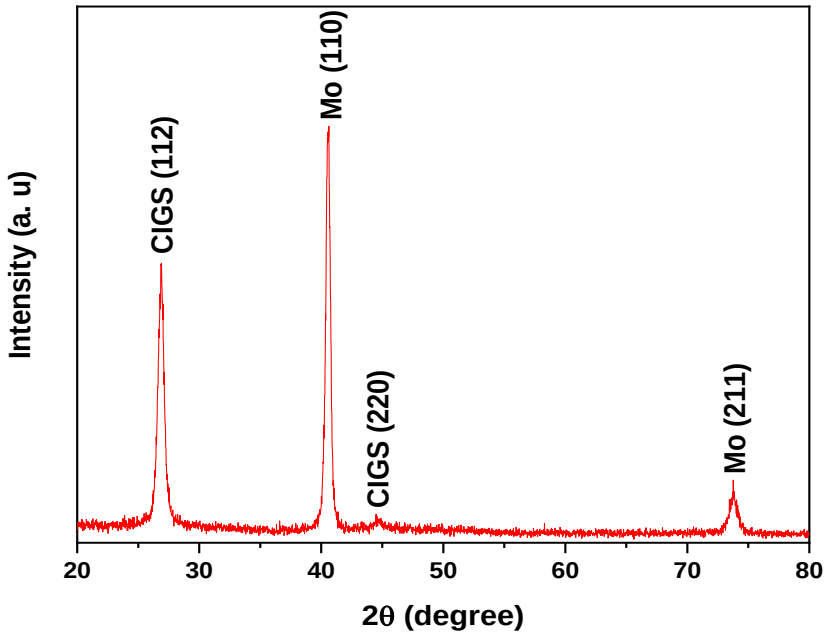

Fig. V.5: X-ray diffraction spectra of CIGS thin films for CIGS/Mo/SLG structure at RT.

In this part, we provide an overview of all the calculations carried out on various structural properties of our sample:

Lattice parameters

The lattice parameters were calculated using the following equations:

$$\frac{1}{d^2} = \frac{h^2+k^2}{a^2} + \frac{l^2}{c^2} \quad \text{(V.5)}$$

$$n\,\lambda = d_{hkl}\sin(\theta) \quad \text{(V.6)}$$

After the calculation, we got the lattice parameters: **a = 5.717 Å** and **c = 11.569 Å**.

Crystallite size D

The Scherrer's Formula is usually most effective for crystallite sizes of 200 nm or less. It is written by the following formula:

$$D = \frac{K\lambda}{\beta\cos(\theta)} \quad \text{(V.7)}$$

Where D - Average crystallite size (nm)

K: Scherrer constant. K varies from 0.68 to 2.08. K = 0.94 for spherical crystallites with cubic symmetry

λ: X-ray wavelength. For XRD with Cu-Kα average λ= 1.5406 Å = 0.15406 nm

B: FWHM (Full Width at Half Maximum) of XRD peak.

θ: XRD peak position, one half of 2θ.

The Table V.1 shows the positions and FWHM of different diffraction peaks. The position (2θ = 26.886) of the intense peak (112) is used to calculate the crystallite size *D* and the calculated *D* (using K=0.94 and Cu-Kα average λ = 0.15406 nm) is:

D = 8.67 nm

Table V.1. Positions and FWHM of different diffraction peaks.

Pos. [°2Th.]	FWHM [°2Th.]	(h k l)
26.886	0.0984	(112)
44.8052	0.4723	(220)

Texture coefficient TC

The preferred orientation of (h k l) plane can be defined as a texture coefficient (TC)(hkl), which is calculated using the following formula:

$$TC(hkl) = \frac{I_{(hkl)}/I_{r(hkl)}}{[(1/n)\sum I_{(hkl)}/I_{r(hkl)}]} \quad \text{(V.8)}$$

Where $I(hkl)$, $I_r(hkl)$, and n indicate the X-ray diffraction intensities which obtained from the film, intensity of the reference diffraction pattern (JCPDS 00-035-1102) and considered number of diffraction peaks, respectively. The higher value of the texture coefficient: TC = 1.95 as indicated in Table V.2, indicates the preferred orientation of the films along the diffraction plane (112).

Table V.2. Positions, Height and texture coefficient of different diffraction peaks.

Pos. [°2Th.]	Height [cts]	(h k l)	**TC**
26.886	595.65	(112)	**1.95**
44.8052	15.19	(220)	**0.05**

Lattice strain (ε)

Effective lattice strain gives an idea about the deficiencies and distortions of the grains in the level of CIGS thin film, which is calculated using the following formula:

$$\varepsilon = \frac{\beta}{(4\tan\theta)} \quad \text{(V.9)}$$

The Lattice strain obtained is: **ε = 1.026**

Dislocation density

The dislocation density of the crystal was evaluated using the formula:

$$\gamma = {}^{1}/_{D^2} \quad \text{(V.10)}$$

We obtained $\gamma = \mathbf{1.33\times10^{-4}\ nm^{-1}}$

As a result, Table V.3 present the positions, FWHM and intensities of different diffraction peaks of obtained CIGS sample.

Table V.3. Positions, FWHM and intensities of different diffraction peaks.

Pos. [°2Th.]	FWHM [°2Th.]	Height [cts]	Rel. Int. [%]	(h k l)	Matched by
26.886	0.0984	595.65	62.94	(112)	00-035-1102
44.8052	0.4723	15.19	1.61	(220)	00-035-1102

Based on the favorable outcomes observed in the structural properties of our sample, it can be concluded that it is well-suited for utilization in solar cell applications.

V.5.2. Morphology study by Atomic Force Microscopy

Atomic Force Microscopy (AFM) is a powerful imaging technique that can provide information about the surface topography and structure of CIGS thin films. AFM can be used to measure the crystalline structure of CIGS films by imaging their surface morphology at high resolution. In AFM imaging, a sharp probe is scanned across the surface of the CIGS film, and the height variations of the surface are measured with high precision. The resulting image can reveal features such as grain boundaries, surface roughness, and crystal orientation, which are important for understanding the crystallinity and structural properties of the material.

The surface investigation revealed that CIGS film prepared by the described method are characterized by a granular structure. Fig. V.6 shows the (a) 2D-AFM image of CIGS obtained film. This image illustrates that the substrate is entirely covered with grains of different sizes and a smooth surface with a root mean square roughness of about 40 nm. This behavior can be attributed to the nucleation and island formation on the film surface as CIGS grains are growing. The size of the CIGS nano-cluster varies from about 25 nm to 50 nm as revealed by the AFM analysis. The image 3D-AFM image of CIGS films is shown in Fig. V.6(b). As can be seen, the film shows a uniform grain size with a typical dense columnar structure.

(a)

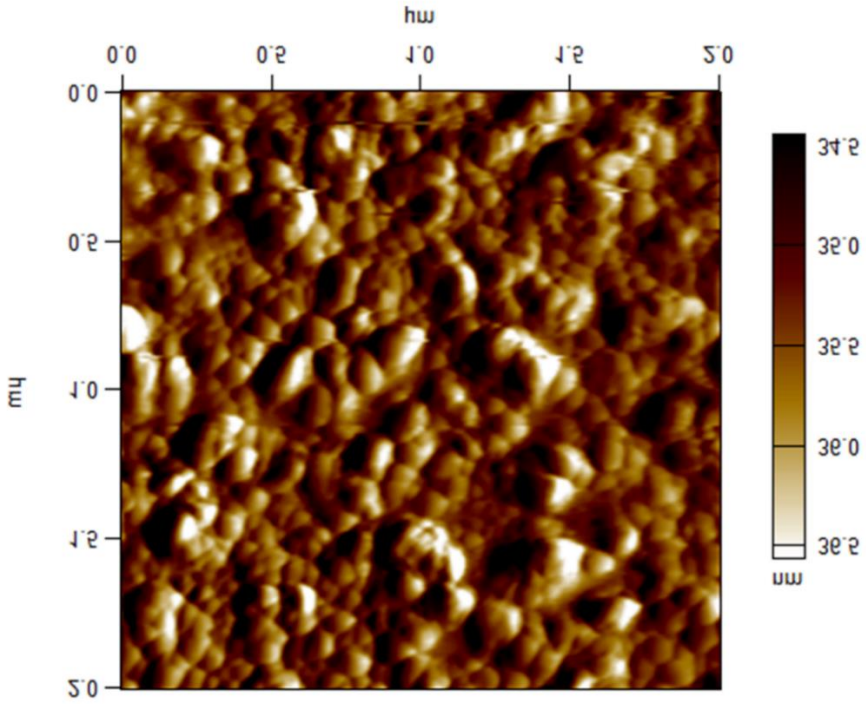

(b)

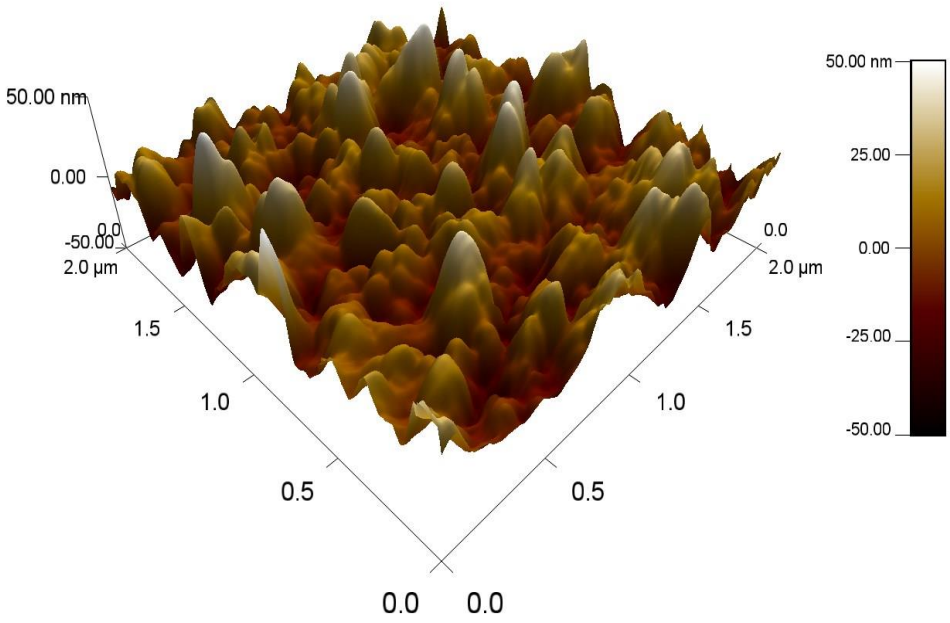

Fig. V.6: AFM morphology images of CIGS thin film deposited by rf-magnetron sputtering at room temperature: (a) 2D-AFM image and (b) 3D-AFM image.

The surface analysis of the CIGS film fabricated by physical method, described in this study, indicated a granular structure. As depicted in Fig. V.6(a), the 2D-AFM image of the CIGS film revealed that the surface was covered entirely with grains of varying sizes, creating a smooth surface with a root mean square roughness of approximately 40 nm. This outcome could be attributed to nucleation and island formation on the film surface during the growth of CIGS grains. The AFM analysis further revealed that the size of the CIGS nano-cluster ranged from 25 nm to 50 nm. Fig. V.6(b) displays the 3D-AFM image of the CIGS film, demonstrating a uniform grain size with a dense columnar structure.

Finally, we can confirm that achieving a uniform and smooth film morphology is essential for reducing defects and enhancing light absorption. The use of RF magnetron sputtering enables good control over the deposition process, leading to improved film morphology and surface quality.

V.5.3. Optical properties study using Fourier transform infrared spectroscopy

Fourier transform infrared spectroscopy (FTIR) is a useful technique for characterizing the structural and optical properties of CIGS (copper indium gallium selenide) thin films. In FTIR spectroscopy, infrared radiation is passed through a sample, and the resulting absorption spectrum is analyzed to obtain information about the chemical bonds and molecular vibrations within the material. It can be used to analyze the vibrational modes of CIGS, including those associated with the $CuInSe_2$ and $CuGaSe_2$ crystal structures. The technique can also be used to detect impurities or defects in the CIGS film, such as the presence of oxygen or sulfur. In addition, FTIR can provide information about the electronic band structure of the CIGS material, which is important for understanding its optical properties and performance in photovoltaic applications.

In general, FTIR spectroscopy is a valuable tool for analyzing the structural and optical properties of CIGS thin films, and it is widely used in research and development of CIGS-based solar cells. By providing insight into the molecular and electronic structure of the material, FTIR can aid in the development of more efficient and stable CIGS solar cells.

The FTIR spectra of CIGS thin films can contain several peaks, each corresponding to different vibrational modes and functional groups within the material. According to Fig. V.7. we observed some peaks in FTIR spectra of CIGS thin film:

- The peak at around 400 - 500 cm^{-1}, exactly at $\boldsymbol{\lambda = 416\ cm^{-1}}$ corresponds to the Se-Se stretching mode in the CIGS material.

- The peak at around 1000 - 1100 cm^{-1}, exactly at **λ = 932 cm^{-1}** corresponds to the Cu-Se stretching mode.
- The peak at around 1600 - 1700 cm^{-1}, exactly at **λ = 1661 cm^{-1}** corresponds to the Se-H bending mode, which may indicate the presence of hydrogen or other impurities in the CIGS film.

These all types of peaks that we observed in FTIR spectra of CIGS thin film. The exact positions and intensities of these peaks can vary depending on factors such as the deposition conditions and the composition of the CIGS material. By analyzing these peaks, we can gain insight into the molecular and structural properties of the CIGS material and optimize its performance in photovoltaic applications.

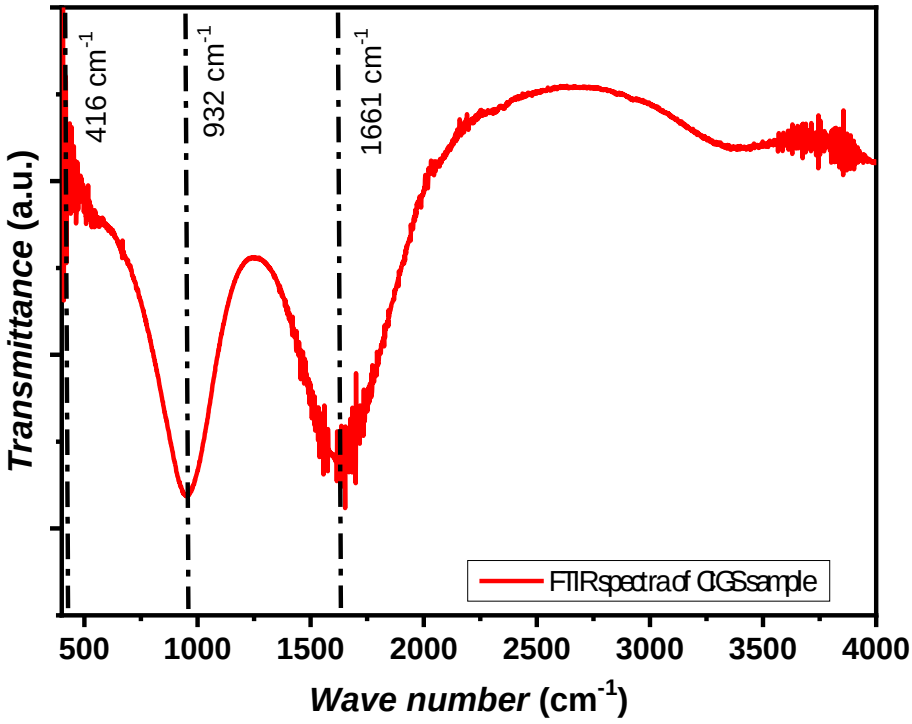

Fig. V.7: FTIR spectra of CIGS thin film obtained by RF magnetron sputtering.

V.6. Conclusion

In conclusion, the utilization of RF magnetron sputtering technique for the fabrication of high-quality CIGS thin films has proven to be effective in achieving desirable structural, morphological and optical properties.

In this work, high quality CIGS thin films were deposited by RF-magnetron sputtering, they have been characterized by various analytical techniques such as X-ray diffraction (XRD),

Atomic Force microscopy (AFM) and Fourier transform infrared spectroscopy (FTIR). These techniques help in studying the structure, morphology and optical properties of the obtained CIGS thin films.

As a result, using RF magnetron sputtering can deposit high quality CIGS thin films and product high-efficiency CIGS solar cells. It enables precise control over film thickness and deposition rate, can be performed at relatively low temperatures, and allows for the use of a wide range of substrate materials. These factors are important for achieving optimal performance and reducing manufacturing costs.

References

[1] Ma, J., Wang, Y., Liu, Y., Feng, X., Zhang, T., & Yao, X. (2021). Fabrication of high-performance CIGS solar cells with enhanced optical and electrical properties. Journal of Materials Chemistry A, 9(11), 6553-6563. doi: 10.1039/d0ta11660d.

[2] Zhou, Y., Li, H., Zhao, L., Zeng, K., Wang, X., Liu, M., Shi, T. (2020). High-efficiency CIGS solar cells with superior charge collection enabled by graded bandgap engineering. Nano Energy, 74, 104859. doi: 10.1016/j.nanoen.2020.104859.

[3] Fan, J., Tang, Q., Xu, J., Yang, X., Wei, C., Wang, Z., Wang, Y. (2022). High-efficiency CIGS thin-film solar cells with n-type ZnO/c-Si heterojunction interface. Solar Energy, 245, 1-10. doi: 10.1016/j.solener.2022.01.055.

[4] Dong, C., Sun, T., Guo, Y., Xu, Z., Sun, K., Wang, X., & Yin, Z. (2022). Non-stoichiometric CIGS thin film fabricated by magnetron sputtering for solar cell application. Solar Energy, 236, 273-280. doi: 10.1016/j.solener.2022.01.033.

[5] Ye, S., Liu, S., Liu, Z., Fu, Y., Chen, H., Wang, X. (2021). Effect of Cu content on the structural and optical properties of CIGS thin films deposited by RF magnetron sputtering. Materials Science in Semiconductor Processing, 127, 105687. doi: 10.1016/j.mssp.2021.105687.

[6] Chen, X., Chen, Z., Zhang, D., Lai, Y., Chen, L., Zhang, S., Sheng, J. (2020). Highly (112)-oriented CIGS thin films prepared by sputtering onto Mo-coated soda-lime glass substrates. Journal of Alloys and Compounds, 846, 156361. doi: 10.1016/j.jallcom.2020.156361.

[7] Zhou, H., Zhang, X., Wang, J., Li, H., & He, Y. (2020). High-quality Cu(In, Ga)Se_2 thin film deposited by RF magnetron sputtering. Solar Energy Materials and Solar Cells, 209, 110496.

[8] Reddy, R. B., Jung, I. H., & Kim, H. K. (2020). Growth of highly oriented $CuInGaSe_2$ thin films by RF magnetron sputtering. Journal of Alloys and Compounds, 832, 154986.

[9] Li, X., Li, W., Li, L., Li, H., Han, G. (2021). High-quality $CuInGaSe_2$ thin films grown by radio frequency magnetron sputtering using a modified dual-target. Journal of Materials Science: Materials in Electronics, 32(6), 7236-7243.

[10] Bao, S., Shu, T., Sun, Q., Zhang, X. (2021). Fabrication of high-quality Cu(In, Ga)Se_2 thin films by RF magnetron sputtering with various Ga contents. Journal of Materials Science: Materials in Electronics, 32(16), 22699-22707.

[11] Wu, C., Chen, J., Liu, Y., Wu, W., Chen, H., Qian, Y. (2020). Control of film thickness and composition in reactive RF magnetron sputtering deposition of AlN thin films. Journal of Materials Science: Materials in Electronics, 31(17), 14335-14342.

[12] Qin, Z., Zhang, X., Li, H., Li, J., Zhang, Y., Li, Y. (2020). Influence of RF sputtering parameters on the thickness and properties of ZnO thin films. Journal of Materials Science: Materials in Electronics, 31(8), 6055-6061.

[13] Kim, T., Lee, S., Kim, K., Kim, Y., Chung, T. M. (2021). Control of film thickness and composition in RF magnetron sputtering of AlN thin films by a neural network approach. Journal of Vacuum Science & Technology A, 39(2), 023001.

[14] Baer, D. R., Thevuthasan, S. (2010). Characterization of Thin Films and Coatings. Handbook of Deposition Technologies for Films and Coatings, 749-864.

[15] D. R. Baer, &Thevuthasan, S. (2010). Characterization of Thin Films and Coatings. Handbook of Deposition Technologies for Films and Coatings, 749-864.

[16] Subba Ramaiah Kodigala, “Chapter 4 - Structural Properties of I–III–VI2 Absorbers”, Thin Films and Nanostructures, Volume 35 (2010) Pages 115-194. https://doi.org/10.1016/B978-0-12-373697-0.00004-3.

CONCLUSION AND FUTURE WORK

CONCLUSION AND FUTURE WORK

In our thesis, we embarked on an investigation of three primary areas of focus. Firstly, we delved into the exploration of simulation study of substrate CIGS solar cells with a BSF layer and heterojunction solar cells based on CGS and CIGS, as well as the tandem and triple-junction solar cells. The study of the impact of Ordered Defect Compound layer and the activation energy levels on CIGS and CIS solar cell performances were done in the second section of this thesis. To achieve this, we used two-dimensional SILVACO/Atlas software to simulate the photovoltaic characteristics of solar cells structures. The third section of this thesis is dedicated to exploring the manufacturing technique employed for the $Cu(In,Ga)Se_2$ thin film. The Rf magnetron sputtering was utilized to deposit high quality CIGS thin film. Structural, morphological and optical properties of CIGS synthetized film were done, respectively, using some good analytical techniques such as X-ray diffraction (XRD), Atomic Force microscopy (AFM) and Fourier transform infrared spectroscopy (FTIR).

In the first section, we calculated the photovoltaic characteristic of substrate solar cell based on Copper Indium Gallium Selenide (CIGS) absorber layer using a back surface field BSF layer. We found that the presence of the BSF layer significantly improved the efficiency of CIGS solar cell. This is due to the creation of a backside BSF electric field by constructing a p+/p interface, which reduces recombination on the backside and consequently improves the electrical efficiency of the solar cell. The CGS/CIGS tandem solar cell and CGS/CIGS triple-junction solar cell under AM1.5G illumination were studied to calculate the current matching point and to extract the optimum solar cell efficiency. Through this analysis, we examined how some factors such as thicknesses, carrier concentration, defect density and operating temperature affect the performance of these solar cells.

In the second section, an in-depth analysis sheds light on the various factors that play a significant role in determining the efficiency of solar cells. Particularly, it highlights the impact of certain parameters such as ODC layer defect, activation energy levels, acceptor and donor traps (E_A/E_D) on the performance of the cells. The findings indicate that defects in the ODC layer have a detrimental effect on the efficiency of CIGS solar cells. Consequently, it becomes crucial to reduce the occurrence of ODC layer defects and/or decrease the thickness of the ODC layer in order to enhance the efficiency of CIGS solar cells.

Finally, we provided a comprehensive overview of the experimental procedures employed in the production of high-quality $Cu(In,Ga)Se_2$ thin film deposited by RF magnetron

sputtering and we conducted a thorough investigation into the structural, morphological, and optical properties of the resulting CIGS thin film.

The obtained good structural, morphological, and optical properties of CIGS films through RF magnetron sputtering offer exciting opportunities for the realization of high-performance photovoltaic devices, bringing us closer to a sustainable and clean energy future.

This research has the potential to contribute towards the development of novel and efficient structures for CIGS solar cells, offering improved performance and cost-effectiveness. Looking ahead, our future perspective involves the simulation and modeling of photovoltaic cells, specifically focusing on the incorporation of Grain Boundaries and deep defect traps within the CIGS absorber layer using three-dimensional SILVACO/Atlas. Furthermore, it is desirable to extend the analysis of defects to perovskite solar cells, broadening our understanding of defect-related phenomena in this particular technology.

ملخص

تبحث هذه الأطروحة في ثلاثة جوانب رئيسية للخلايا الشمسية CIGS. يستكشف الجزء الأول محاكاة بنية الخلايا الشمسية CIGS الركيزة باستخدام طبقة المجال السطحي الخلفي (BSF)، بالإضافة إلى الخلايا الشمسية متعددة الوصلات القائمة على النحاس، الجاليوم والسيلينيوم (CGS) والنحاس، الإنديوم، الجاليوم والسيلينيوم (CIGS)، مثل خلايا ثنائية الوصلة والخلايا الشمسية ثلاثية الوصلات. يفحص القسم الثاني تأثير طبقة العيوب (ODC) ومستويات طاقة التنشيط E_A وE_D على أداء الخلايا الشمسية CIGS وCIS باستخدام برنامج SILVACO Atlas-2D /. ويركز القسم الأخير على عملية ترسيب أغشية CIGS الرقيقة عالية الجودة باستخدام تقنية السحق المهبطي بموجات الراديو. تخضع الرقائق التي تم الحصول عليها للتحقيق في خواصها الهيكلية والمورفولوجية والبصرية من خلال بعض التقنيات مثل تحليل حيود الأشعة السينية (XRD)، والفحص المجهري للقوة الذرية (AFM) وتحويل فورييه الطيفي بالأشعة تحت الحمراء (FTIR) وهذا على التوالي.

الكلمات المفتاحية: الخلايا الشمسية، CIGS، BSF، المردودية، مستويات المصائد، طبقة ODC، السحق المهبطي بموجات الراديو.

Abstract

This thesis investigates three key aspects of CIGS solar cells. The first part explores simulations of substrate CIGS solar cell structure using Back Surface Field (BSF) layer, as well as the multi-junction solar cells based on Copper Gallium Selenide (CGS) and Copper Indium Gallium Selenide (CIGS), such as tandem and triple-junction solar cells. The second section examines the impact of the Ordered Defect Compound (ODC) layer and the activation energy levels E_A and E_D on the performance of CIGS and CIS solar cells using SILVACO/Atlas-2D software. The final section concentrates on the deposition process of high-quality CIGS thin films using rf-magnetron sputtering technique. The obtained films are subjected to investigation of their structural, morphological and optical properties through some techniques such as X-ray diffraction (XRD) analysis, Atomic Force microscopy (AFM) and Fourier transform infrared spectroscopy (FTIR), respectively.

Keywords: Solar cell, CIGS, BSF, Efficiency, Trap levels, ODC layer, rf-Magnetron Sputtering.

Résumé

Cette thèse examine trois aspects clés des cellules solaires CIGS. La première partie explore les simulations de la structure des cellules solaires CIGS sur substrat en utilisant une couche de champ de surface arrière (BSF), ainsi que les cellules solaires multi-jonctions basées sur le sélénium de cuivre-gallium (CGS) et le sélénium d'indium de cuivre-gallium (CIGS), telles que les cellules solaires tandem et triple-jonction. La deuxième section examine l'impact de la couche de défauts ordonnés (ODC) et des niveaux d'énergie d'activation EA et ED sur les performances des cellules solaires CIGS et CIS en utilisant le logiciel SILVACO/Atlas-2D. La dernière section se concentre sur le processus de dépôt de films minces de haute qualité en CIGS en utilisant la technique de pulvérisation cathodique radiofréquence. Les films obtenus font l'objet d'une étude de leurs propriétés structurales, morphologiques et optiques par le biais de techniques telles que l'analyse de diffraction des rayons X (DRX), la microscopie à force atomique (AFM) et la spectroscopie infrarouge à transformée de Fourier (FTIR), respectivement.

Mots clés: Cellule solaire. CIGS. BSF. Rendement. Niveaux de piège. ODC. Pulvérisation cathodique radiofréquence.